A 3-D COMPUTER MODEL TO SIMULATE THE SINTERING OF A RANDOMLY PACKED GREEN COMPACT IN ORDER TO INVESTIGATE THE EVOLUTION OF THE MICROSTRUCTURE

by

Brian Michael Ennis

BS, University of Pittsburgh, 1992

MBA, University of Pittsburgh, 1998

MS, University of Pittsburgh, 2002

Submitted to the Graduate Faculty of

the School of Engineering in partial fulfillment

of the requirements for the degree of

Doctor of Philosophy

University of Pittsburgh

2005

UNIVERSITY OF PITTSBURGH

SCHOOL OF ENGINEERING

This dissertation was presented

by

Brian Michael Ennis

It was defended on

December 1, 2005

and approved by

Dr. Michael J. Kolar, Professor, Dept. of Mechanical Engineering

Dr. Patrick Smolinski, Associate Professor, Dept. of Mechanical Engineering

Dr. Ian Nettleship, Associate Professor, Dept. of Materials Science and Engineering

Dissertation Director: Dr. William S. Slaughter, Associate Professor, Dept. of Mechanical Engineering

ABSTRACT

A 3-D COMPUTER MODEL TO SIMULATE THE SINTERING OF A RANDOMLY PACKED GREEN COMPACT IN ORDER TO INVESTIGATE THE EVOLUTION OF THE MICROSTRUCTURE

Brian Michael Ennis, PhD

University of Pittsburgh, 2005

The objective of this research project was to develop a three-dimensional computer model to simulate the sintering of a randomly packed green compact in order to investigate the evolution of the microstructure as densification progresses. The model randomly generates a population of spheres to simulate the particle size distributions present in commercial alumina powders. The spheres were packed into a cubic volume to construct a Representative Volume Element (RVE) with properties statistically comparable to the properties measured in real sintered materials. Sintering was modeled as uniform flattening of the contact between spheres. The sintering process was assumed to be isotropic and homogenous. The simulation of the sintering process was later expanded to include Local Particle Rearrangement (LPR). The model was compared to experimental data obtained from measurements on sintered alumina samples using two techniques: the stereological parameters for the RVE determined by the simulation, and additional measurable quantities obtained from applying tessellation to cross sections taken from the RVE to further describe the characteristics of the microstructure. Based on the measured stereological parameters and the properties of the tessellated cells, the simulation

reproduced behavioral trends in the microstructure similar to those observed in the measurement of the experimental samples thus demonstrating the feasibility of employing this type of model to explore the microstructure. The results also indicate that the generation of agglomerated particle packing arrangements may be useful in simulating the microstructural evolution of sintering since the presence of the large voids used to simulate agglomeration had a significant effect on the results. The use of LPR in the simulation did not appear to affect the results for a particle arrangement with no agglomerations, but it did influence the results for the particle arrangement with agglomeration. The results for the LPR simulations suggest that the ability of the particles to slide past each other, modeled in the simulation by the tangential viscosity, may influence the rate at which small pores are formed and/or eliminated in the RVE. However, the LPR simulations indicate that more particles are needed to effectively model the influence of agglomeration in the particle arrangement.

TABLE OF CONTENTS

LIST OF TABLES

LIST OF FIGURES

ACKNOWLEDGEMENTS

I would like to express my gratitude to my advisor, Dr. William S. Slaughter, for his guidance, support and patience throughout my graduate engineering studies at the University of Pittsburgh. I would also like to thank Dr. Ian Nettleship of the Materials Science and Engineering Department for his valuable advice and contributions to this research project. Finally, I wish to thank my family and friends for their continued support during the pursuit of my academic goals.

1.0 INTRODUCTION

Sintering is a common material forming process by which a shaped part made from a powder is heated to form a solid object. Sintering is the primary material consolidation process for ceramic products. Many common ceramics such as bricks, earthen wares, and glass, have been manufactured using sintering for centuries. In recent years, additional ceramic materials have been developed to meet the design requirements for new applications. Many advanced ceramic materials have insulating or dielectric properties which have led to significant improvements in electronic circuitry by increasing the capacity of a wide range of electronic components including capacitors, inductors, and piezoelectric materials. Other applications for ceramic materials include such uses as high temperature resistant components for jet turbines and rocket nozzles, refractory materials for furnaces, and uranium oxide fuel rods for nuclear reactors. Sintering can also be an alternative to other manufacturing methods, such as casting or forging, for products made from a variety of metals depending on the production costs or the application. Some examples of sintered metal products are oil-impregnated bearings (bronze), incandescent lamp filaments (tungsten) and permanent magnets (iron).

Prior to sintering, the powder material is pressed into a die to form a green compact. The fluid-like characteristics of the material powder provides the capability to produce complex solid shapes. This near net shape capability minimizes waste material and machining operations leading to potentially lower production costs. This is particularly true for mass production in

cases where the die used to form the shape can be used repeatedly. The subsequent sintering of the green compact densifies the powder into a solid and generally improves the properties. Unfortunately, sintering involves large amounts of shrinkage, usually about 18% linear shrinkage, and can result in less favorable engineering properties when compared to other manufacturing processes. Hence, the capability to improve and optimize material properties during sintering is essential. There are two important design considerations when using sintering as the means of production. The first design consideration is the ability to predict volume shrinkage and shape changes to predetermine the dimensions of the initial green piece. It is often difficult to predict the final shape from the initial shape due to the inhomogeneity of the dimensional changes as densification progresses. Consequently, in many cases, trial and error is the only means to determine the best technique to achieve the desired final shape. The second design consideration is the ability to predict the desired material properties of the final piece. Since both the dimensional changes and material properties are related to the evolution of the microstructure, there is a need to develop models capable of accurately predicting the microstructural behavior of materials during the sintering process. [1-3]

Traditionally, two general types of models have been used as design tools to engineer the fabrication of parts using the sintering process. The first type, continuum models [4, 5], has been developed to predict dimensional changes. However, in such models, the internal structure of the powder compact is often only represented by the change in the relative density. Since the specific details of the microstructure geometry are not considered, this results in obvious difficulty when attempting to incorporate the effects of microstructural evolution into the predictive model. The second type, contact flattening models [6, 7] with ordered geometry, has been used for many decades to predict the effect of temperature and time on sintered density.[8-10] The main drawback

to these models is the assumption of a fixed, ordered packing, or a dense, random packing. This assumption allows the unit cell to be simplified to one particle and its attendant porosity. However, it also precludes the direct modeling of the packing arrangement and its subsequent effect on sintering.

With advances in computer technology, other modeling techniques have been developed. Some attempts have been made to model two-dimensional sintering of monosized spheres to evaluate differential sintering, [11, 12] but the extension of a model into three dimensions is not as common.[13] Several studies have analyzed the three-dimensional packing arrangement of particles modeled as spheres. However, these models limit their focus to the efficiency of the particle packing by only evaluating the model based on the initial (green) density of the packing arrangement; the subsequent effect of the sintering process is not considered.[14-20] A few of the more recent models employ a multiscale approach. Generally, algorithms to control the interaction of the particles are developed using either phenomenological behavior [11, 12] or constitutive relationships [21, 22] as the basis for building a network of particles.

The present model is a three-dimensional (3-D) simulation of sintering for randomly packed particle arrangements. This model differs from previous attempts in several ways. First, the manner in which the particles are packed is improved by utilizing a control algorithm that randomly moves each particle as it is placed in the containing volume. Second, Monte Carlo integration techniques were adapted for the first time to calculate the stereological parameters to permit a comparison to data commonly reported in experimental studies to characterize sintered materials. Third, the model introduces a technique to simulate agglomerations in the particle arrangement to demonstrate how particle agglomerations can influence sintering behavior. Fourth, the model demonstrates how tessellation can be applied to 2-D cross sections from the

simulation to provide additional information for comparing the model results to experimental results. Finally, equilibrium equations are developed to allow for local particle motion in the packing arrangement.

2.0 BACKGROUND

This section describes the essential details of the fundamental concepts forming the basis for the development of the sintering model presented in this paper. The background has been separated into four main topics: a review of the sintering process with a brief summary of common sintering models, the computer modeling of particle packing arrangements, stereology, and the basic concepts of tessellation.

2.1 SINTERING

Sintering is a common material forming process used to manufacture ceramic and metallic products. The process begins with a material powder being placed in a die and then compressed using an applied external pressure. The powder at this point is often referred to as the green compact. After the green compact is formed, heat is then applied during sintering to transform the material from a powder into a solid object. The sintering temperature varies based on the material and the desired properties, but it is generally 50% to 80% of the melting temperature of the powder material. The applied heat activates the material transport mechanisms, called diffusion, which lead to densification of the material. Densification occurs primarily because of the high surface area per unit volume of the powder. At first, the reduction of the surface area is

through the formation of necks between adjacent particles. In later stages, the reduction of the surface area is usually achieved through a decrease in pore size and/or removal of the pores. The change in density results in shrinkage (generally anisotropic) of the material. The sintering process is influenced by several important factors including, but not limited to: the sintering temperature, the particle size, the sintering time, the heating rate and the applied pressure. For the sintering process, there are two main concerns for the design and manufacturing of products made using sintering: the dimensional change which can occur as a result of the densification of the material and the evolution of the microstructure which is the primary factor influencing many of the material properties such as strength, conductivity, magnetic permeability and corrosion resistance. Characterization of the microstructure is generally made by examining the pore structure and/or the size and shape of the grains. [1, 3]

The sintering process is typically separated into three generic stages: initial, intermediate and final. These stages indicate the general geometric progression of the microstructure as the powder compact evolves into the final solid object. The initial stage of sintering is characterized by neck growth between adjacent particles in contact with each other. In this stage, the void phase exists as one continuous network. The initial stage continues until adjacent necks begin to overlap. This signifies the start of the next stage. The intermediate stage of sintering is characterized by the interaction between adjacent necks as neck growth proceeds. The voids generally decrease in size in this stage. However, the void phase still remains a continuous network. The final stage of sintering is characterized by the breakup of the void phase network as densification progresses to the point where the voids become isolated. It is important to note that the transition between sintering stages is not always distinct, or even uniform throughout the

sintered object. Hence, the range of densities for which the characteristics of a particular stage apply can vary for different materials.

2.1.1 Sintering Fundamentals

The ability to predict the dimensional change is an important design consideration for the manufacture of product made from sintered materials. Historically, manufacturers have relied on measurements obtained through trial and error to predict the dimensional changes which can occur during the sintering process. From a measured change (ΔL) in the initial dimension (L), the overall volume change (ΔV) from the green volume (V) can be estimated for small shrinkages by the relationship [1],

$$\frac{\Delta V}{V_0} = 1 - \left(1 - \frac{\Delta L}{L_0}\right)^3 \approx \frac{3\Delta L}{L_0}.$$

However, this approximation does not account for anisotropic dimensional changes which can occur during the sintering process.

The fundamental description of the sintering process is typically based on the interaction of two identically sized spheres of diameter, D, in contact with each other [1] as shown in Figure 1. During sintering, matter moves to the contact region between the two spheres, eventually forming a neck of diameter, X. This is often referred to as contact flattening. For solid-state sintering, empirical data indicates that it is possible to estimate the initial shrinkage using the neck size ratio (X/D) by the relationship [1],

$$\frac{\Delta L}{L_0} = -\left(\frac{X}{D}\right)^2 .$$

However, this is only an approximation for very small neck size ratios (X/D) ≤ 0.2.

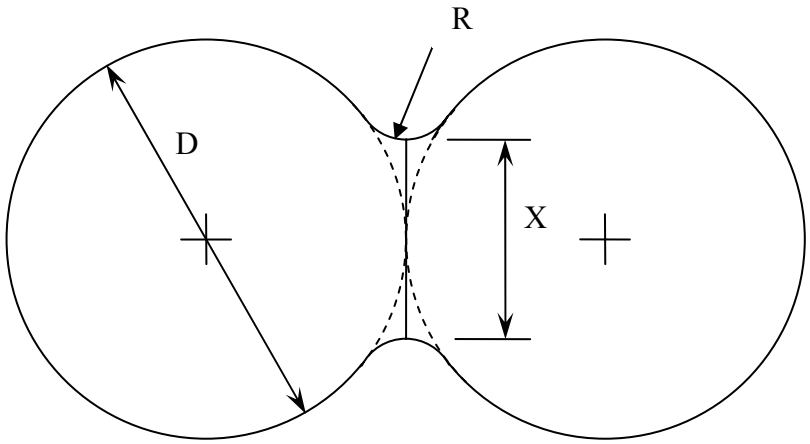

Figure 1. Two sphere model of contact flattening.

The driving force for the transfer of matter in the sintering process is a gradient chemical potential resulting from differences in curvature of the surfaces. The curvature of the spheres (diameter D in Figure 1) is much larger than the curvature at the interface (radius R in Figure 1) and the neck (diameter X in Figure 1). Various mass transport mechanisms move matter from the surface or from between the sphere centers to the neck region. As the size of the neck increases, the radius of curvature in the neck region decreases resulting in a reduction of the surface energy.

2.1.2 Phenomenological Models

Phenomenological models have been developed to predict sintering behavior using observations made on the mass transport mechanisms. The possible mechanisms contributing to mass transport include surface diffusion, evaporation-condensation, volume diffusion, grain boundary diffusion, viscous flow, plastic flow and vapor transport. Several studies have been conducted to examine the various mass transport mechanisms for different materials. [6, 7, 10] For phenomenological models, a single dominant mass transport mechanism is typically assumed to be responsible for the mass transfer. The initial stage geometry is generally based on the contact flattening model as shown in Figure 1. Using empirical data from experiments, a general rule has been developed linking the neck ratio size to the sintering rate for isothermal sintering by the relationship [1],

$$\left(\frac{X}{D}\right)^n = \frac{Bt}{D^m}.$$

Where,

X = Neck diameter.
D = Particle diameter.
B = Constant which is a function of material properties and geometric constants.
t = Time.
n, m = Coefficients.

Using this information, it is possible to estimate the shrinkage from the relationship [1],

$$\left(\frac{\Delta L}{L_0}\right)^{n/2} = \frac{Bt}{2^n D^m}.$$

Not all the mass transport mechanisms result in shrinkage. Surface transport mechanisms such as surface diffusion and evaporation-condensation do not affect particle spacing. Instead, these mechanisms promote neck growth without densification as shown in Figure 1. On the other hand, bulk transport mechanisms such as volume diffusion, grain boundary diffusion, viscous flow, plastic flow and vapor transport result in shrinkage as the location of the particle centers move together [1] as shown in Figure 2.

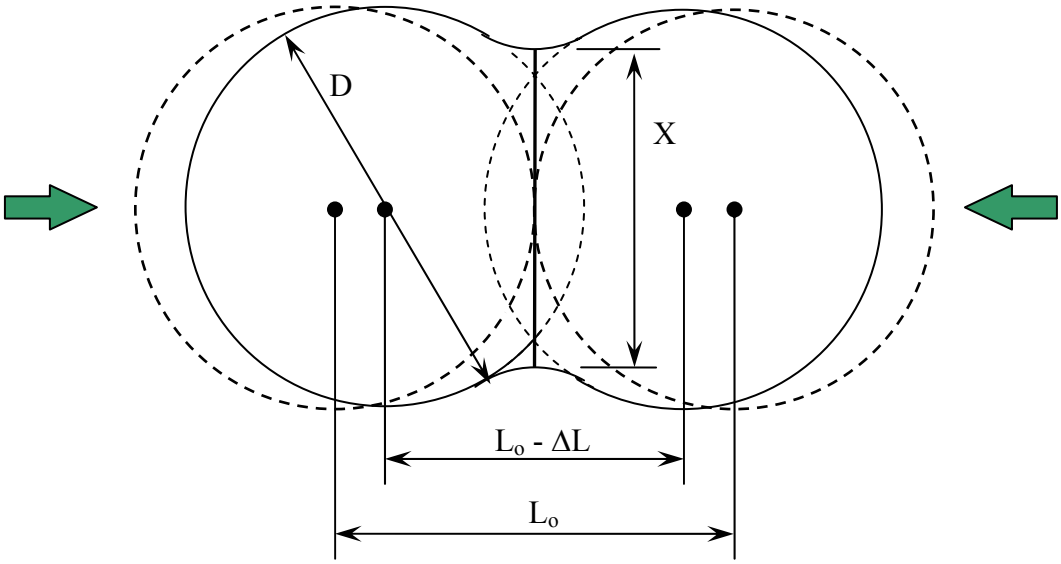

Figure 2. Two sphere contact flattening model with shrinkage.

Over the years, experimental studies have reported estimated values for the parameters based on experimental observations. The variance in the parameter value for the different mass transport mechanisms, summarized in Table 1, demonstrate the complexity of the sintering process. The assumption of a single mass transport mechanism is valid for some materials. However, Ashby [8, 9] developed the concept of sintering diagrams as a tool to illustrate that the contributions of the different mass transport mechanism to the total mass transport can vary, not

only for each stage of the sintering process, but also for different materials and particle sizes. This emphasizes the necessity, as well as the difficulty, of developing better models to accurately predict shrinkage and the evolution of the microstructure. [1-3]

Table 1: Parameter Values for Two Sphere Models in the initial stage of sintering. [1]

Material Transport Mechanism	n	m	Constant, B
Viscous Flow	2	1	f(surface energy, viscosity)
Plastic Flow	2	1	f(surface energy, Burgers vector, volume diffusivity, temperature)
Evaporation-Condensation	3	2	f(surface energy, vapor pressure, temperature)
Volume Diffusion	5	3	f(surface energy, volume diffusivity, temperature)
Grain Boundary Diffusion	6	4	f(surface energy, grain boundary diffusivity, temperature)
Surface Diffusion	7	4	f(surface energy, surface diffusivity, temperature)

2.1.3 Ordered Geometry Models

The phenomenological models are generally valid only for the initial stage of sintering where the neck size ratio (X/D) $\leq$ 0.3. As sintering progresses into the intermediate stage, neck to neck impingement begins to occur. For higher neck size ratios, impingement of adjacent necks begins to occur. As a result, the two sphere models become an inadequate representation of the actual geometry. Consequently, other models were developed based on the assumption of different geometric shape. The model for the initial stage of sintering approximates the geometry with a body centered sphere inside a unit cell which overlaps with adjacent spheres. This essentially creates an octahedral shape which is expanded to simulate sintering. For the intermediate and

final stages of the sintering process, tetrakaidecahedra (polyhedra with 14 sides) are typically used as the main shape because this shape provides a close approximation to the average number of grain contacts observed in many experiments. For the intermediate stage, interconnected cylinders, located at the edges of the tetrakaidecahedra, are used to model the continuous pore network. For the final stage, the cylinders are replaced by spheres at the intersection of the tetrakaidecahedra to model the breakup of the pore network into isolated pores. For all the geometries, it is assumed that the microstructure has an ordered geometric arrangement. This reduces the problem to the consideration of a unit cell thereby simplifying the calculation of the geometric parameters. These models are valid only for those values of the solid volume fraction where the assumed geometry holds. [1, 23, 24]

There are several facts which limit the usefulness of ordered geometry models. First, experimental measurements demonstrate that actual packing arrangements are not ordered. Also, the particles in ordered geometry models are assumed to be monosized in order to reduce the problem to the consideration of a unit cell. Consequently, the models cannot capture the effect of the particle size distribution or the presence of agglomerations on the sintering process since the models inherently lack the means to simulate their behavior. Lastly, the assumed geometries do not allow for local variations in the microstructure caused by particle rearrangement.

2.1.4 Constitutive Models

Using continuum mechanics, constitutive models [4, 5, 25-28] have been developed based on the simulation of the sintering process as the deformation of a porous viscous material. Olevsky[4] and Cocks[5] have provided comprehensive reviews of the techniques and their application to

several sintering situations. Although the governing equations differ depending on the application to specific cases, the constitutive relationships essentially link the sintering stress to the strain rate of deformation through bulk material properties and the density of the material. The microstructure is quantified by tracking the change in density as sintering progresses. The effect of porosity on the material properties is derived based on assumptions concerning the pore shape (spherical or cylindrical) and the overall geometry. The main drawback to employing constitutive models is their reliance on material parameters to quantify material behavior. Since the material properties used in constitutive models are generally derived from macroscale measurements of experimental samples, it can be difficult to predict the microscale influence on the material properties of variations in particle size distribution or the presence of agglomerations.

2.2 COMPUTER MODELS OF PARTICLE PACKING ARRANGEMENTS

2.2.1 Random Packing Models

A number of studies have analyzed the packing arrangement of particles modeled as spheres.[14-19] Most of the models can be classified into one of two general methods. The first method randomly places a distribution of particles inside a specific containing volume. [14-16] The particles are then moved in an iterative process to eliminate any overlaps between particles. The second method, sometimes referred to as the ballistic deposition method, places the particles in

the containing volume one particle at a time.[17-19] In this case, the particles are moved based on gravity. When particles make contact with each other, the moving particle is rotated around the contacted particle by rolling motion. Motion is stopped when the particle reaches a gravitationally stable position (defined as when the center of the particle is directly over the plane region connecting the points of contact of the supporting particles). Both methods treat the particles as hard spheres with a log-normal size distribution. Spheres are used to model the particles because their simple geometry is easy to use. The shape of the containing volume varies from model to model, but the most common shapes utilized are spheres, cylinders, or cubes. While there are several different size distributions which can be employed [29], the log-normal size distribution is the most commonly used in sintering models. The models are generally evaluated based solely on the solid volume fraction (i.e. the volume occupied by the particles divided by the volume being considered) for the initial packing arrangement. Nolan and Kavanagh have investigated the efficiency of the particle packing by varying the mean and standard deviation of the particle sizes.[14-16] Their analysis of different arrangements of randomly packed spheres report values for the volume fraction ranging from 0.509 to 0.638.

2.2.2 Multiscale Models

In recent years, a few models have been proposed to simulate the sintering of the particle packing arrangement using a multiscale approach. Jagota and Dawson developed constitutive relationships for the interaction of individual particles [11] which was extended to a two dimensional network of particles linked by the contact between particles.[12] Parhami and McMeeking [22] created a network of monosized spheres using a diffusional creep law.[21] In these simulations, the multiscale models use phenomenological or constitutive relationships to

develop algorithms to govern the behavior of a pair of particles. The model is then extended, using the behavior of the discrete particles to predict particle behavior, into a network of particles. The main drawback to these methods is that the models rely on the relative density to describe the microstructure.

2.3 STEREOLOGY

There are several different techniques available to obtain the data used to characterize the microstructure of real sintering materials including optical microscopy, scanning electron microscopy and transmission electron microscopy. However, these methods suffer from the same drawback — the necessity of using measurements of features on two-dimensional (2-D) scanned images to quantify the properties of a three dimensional (3-D) sintered solid. To overcome this difficulty, the science of stereology was developed, based on statistical sampling and spatial geometry, to determine the geometric properties used to describe the characteristics of the 3-D solid from measurements of 2-D surfaces or sections. [30-33]

2.3.1 Basic Assumption

Stereology is based on the assumption that the 2-D sections(s) taken from the solid are an accurate statistical representation of the 3-D properties of the solid volume. If the features being measured are randomly placed in the volume under consideration, then the assumption is valid

and any arbitrary section(s) will meet the requirement for statistical representation. However, there are cases where the features are not randomly placed or uniform in the volume (material structures with preferred orientations for example). In these instances, a sufficient number of randomly oriented and located (or statistically uniform) sections taken from the solid are needed to adequately describe the features in the volume to meet the requirement for statistical representation.

To illustrate how the location of the sections can affect the results of the measurements, consider the first case of a sphere with the radius, $R_{B,}$ as shown in Figure 3. If the section is located away from the center of the sphere (see Section A-A), the surface shows a circle with radius, $R_{A,}$ which is less than the true radius of the sphere. However, if the section is taken through the center of the spheres (see Section B-B), the section shows a circle with radius, $R_{B,}$ corresponding to the true radius of the sphere.

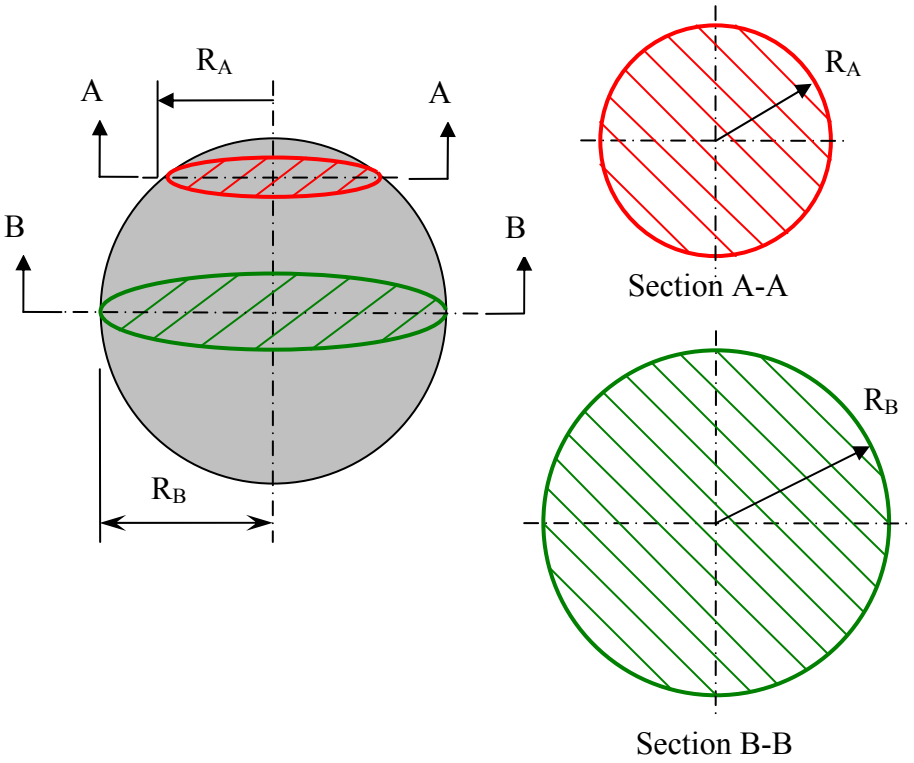

Figure 3. Difference in measured particle size and contact due to section location.

The orientation of the sections can also affect the measurements. Asymmetrical shapes with preferred orientations can lead to incorrect statistical information concerning the size and the shape of the features. This is illustrated by the case of a cylinder as shown in Figure 4. If a section is taken along the cylinder length (Section C-C in Figure 4), the projected area implies that the shape of feature is a rectangle. However, if the section is taken perpendicular to the length (Section D-D in Figure 4), the projected area implies that the shape of the feature is a circle. This disparity in section shape demonstrates the necessity of taking multiple, randomly located and oriented sections to obtain sufficient information to adequately quantify the measured feature(s). If the sections taken from the solid are not randomly oriented for this case,

the results will be skewed leading to a misinterpretation of the actual size and shape of the objects being measured.

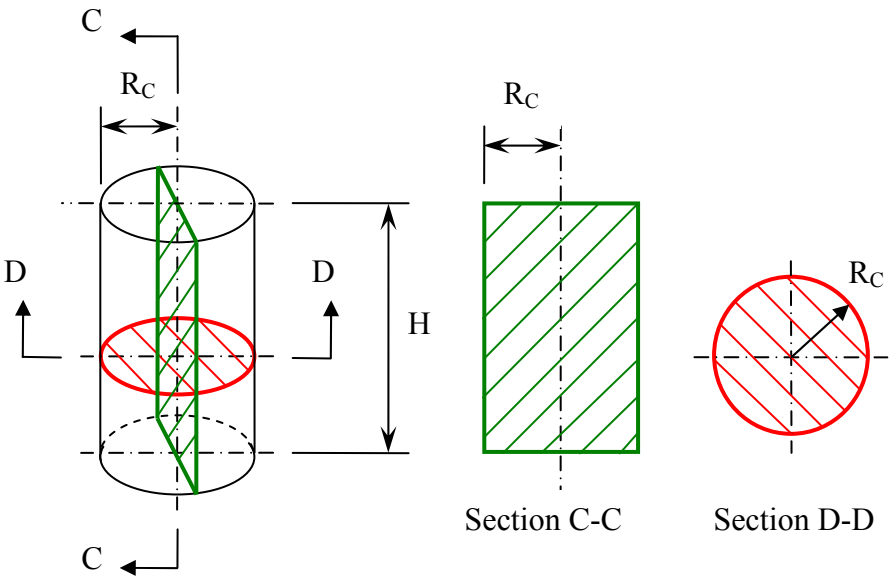

Figure 4. Difference in projected area due to asymmetrical shape.

Since the shapes of the features are generally unknown before the measurements, multiple randomly located and oriented sections are typically used to provide sufficient statistical data to determine the true size and shape of the features present in the sample.

2.3.2 Terminology

The science of stereology has its own nomenclature to identify measured quantities. Each quantity is specified using three variables: a main variable, a subscript and a superscript. The main variable specifies the geometric property being measured (identified by V for volume, S for surface area, L for line, and P for points). The subscript refers to the region under consideration.

In general, the superscript identifies the phase being measured. For this investigation, the superscript is used to distinguish between the solid space occupied by particles (identified by S for solid) and the void space between them (identified by V for void). Thus, as an example, the volume (specified by main variable V) occupied by the solid particles (specified by superscript S) per unit volume (specified by subscript V) is identified in stereological notation as $V_V{}^S$.

2.3.3 Relationship between Measured 2-D and 3-D Properties

There are several methods which can be applied to the measurement of the features on the 2-D plane section (or surface): areal analysis, lineal analysis and point analysis. Consequently, there are different, but equivalent, techniques which may be employed to determine the same stereological parameter. For sintered materials, the measured properties of interest are the solid volume fraction ($V_V{}^S$), the solid-solid surface area per unit volume (S_V^{SS}), and the solid-void surface area per unit volume (S_V^{SV}). In general, the volume and surface area are related to equivalent areal, lineal or point properties through the following relationships [33]:

$$V_V{}^S = A_A{}^S = L_L{}^S = P_P{}^S$$

$$S_V = 2 \cdot P_L$$

The proof of the relationship for the volume measurements is summarized here for each method.[32, 33] For areal analysis, the proof to find the solid volume fraction is based on the concept that the volume of an object can be determined from integrating the area over the length

of the object. If features are randomly placed in a volume as shown in Figure 5, then a slice of thickness, dx, and area, A_0, taken from the volume will intersect some of the features.

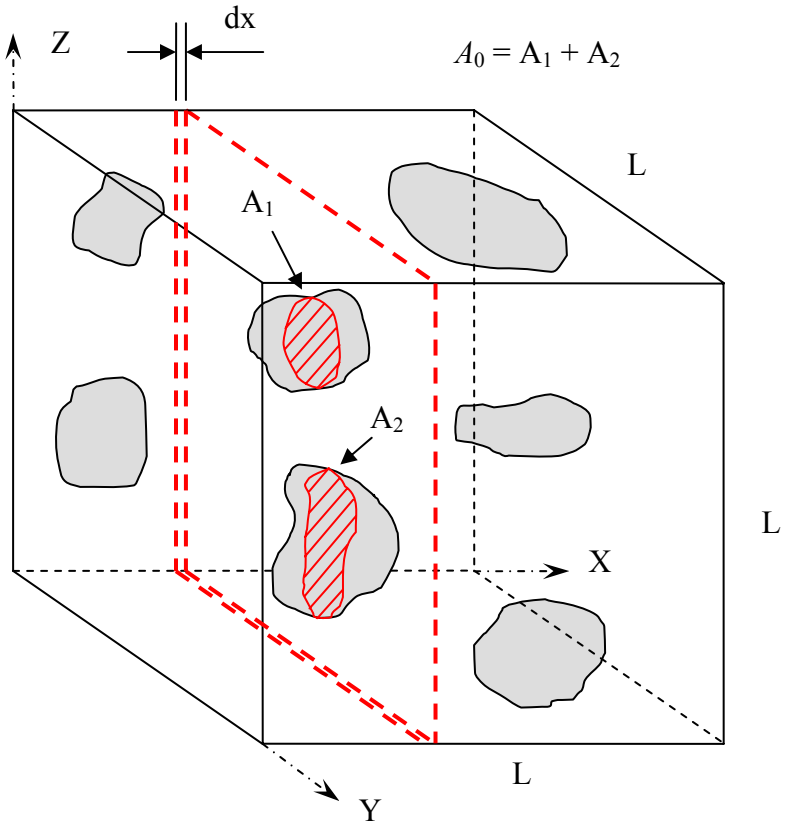

Figure 5. Area of the sample section taken from the solid.

The features on the intersecting plane will have some area, A, which can be determined. The calculated area of the features will vary for each slice depending on the size, shape and number of the intersected features. Hence, if multiple slices are taken, a distribution of the area of the features as a function of the length of the examined volume can be profiled as shown in Figure 4.

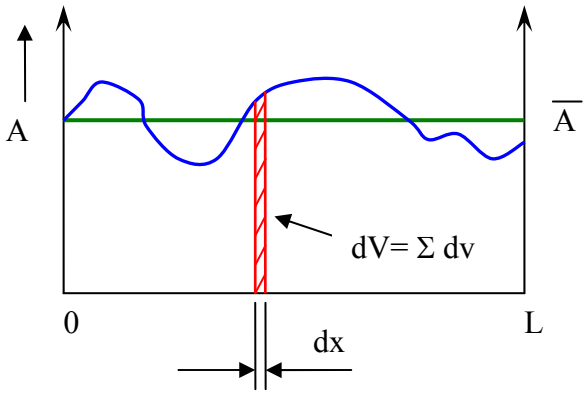

Figure 6. Variation of the feature area over the length of the volume.

The average area, $\overline{A}$, of the features for the different slices could then be determined. The differential volume of the features on the slice is given by

$$dV = \sum dv = \sum a dx = A dx .$$

This expression is integrated over the length to determine the volume of the feature,

$$V^S = \int_0^L dV = \int_0^L A dx = \overline{A} \cdot L .$$

The calculated feature volume is then divided by the total volume, V_0, considered to determine the feature volume per unit volume,

$$V_V{}^S = \frac{V^S}{V_0} = \frac{\overline{A} \cdot L}{A_0 \cdot L} .$$

Thus, the solid volume fraction, $V_V{}^S$, is equivalent to the solid area fraction, $A_A{}^S$ through the relationship,

$$V_V{}^S = \frac{\overline{A}}{A_0} = A_A{}^S .$$

A similar argument can be made to use lineal analysis instead of the areal analysis. In this case, consider the surface of the 2-D section taken from the 3-D solid as shown in Figure 5.

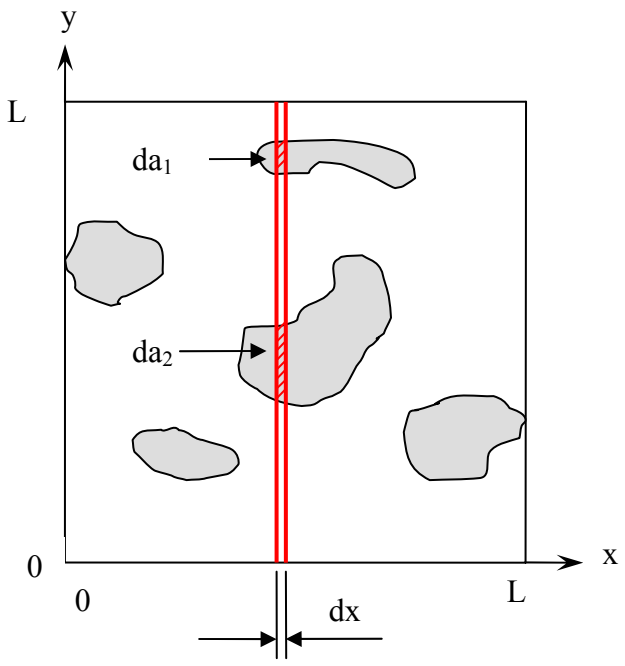

Figure 7. Lineal analysis on a surface to find area of feature.

If multiple lines are considered, then a distribution of the line length intersecting the features over the length of the area can be profiled (similar to the previous example) as shown in Figure 6.

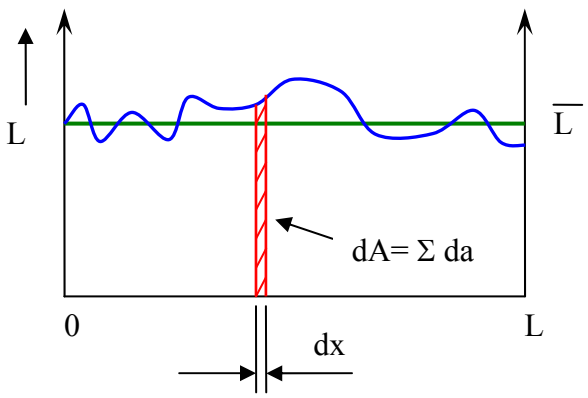

Figure 8. Feature line length variation.

Thus, the differential area, which is a function of the feature line length from the section, is given by

$$dA = \sum da = \sum l dx = L dx .$$

This expression can be integrated to determine the area of the feature,

$$A = \int_0^L dA = \int_0^L L dx = \overline{L} \cdot L .$$

The calculated feature area is then divided by the total area considered to determine the feature area per unit area,

$$A_A = \frac{A}{L^2} .$$

Thus proving the relationship,

$$A_A{}^S = L_L{}^S .$$

Finally, a point analysis can be employed as well to find the solid volume fraction. Point analysis is based on a random distribution of points on the body being examined. For a volume, the probability that a point resides in the space occupied by the features is proportional to the number of points inside the features divided by the number of total points considered,

$$V_V{}^S = P_P{}^S .$$

Thus, it has been shown that the solid volume fraction can be determined using point, lineal and areal solid fractions are equivalent to

$$V_V{}^S = A_A{}^S = L_L{}^S = P_P{}^S .$$

In actual practice, the solid volume fraction is determined using a point analysis by applying a grid of points to the surface of the sample since it is not possible to apply a 3-D grid of points to the actual volume. An example of this measurement is illustrated in Section 2.3.4.1. The decision to employ areal, lineal or point analysis is generally based on the most efficient manner of calculating the particular quantity being measured. Similar proofs, omitted here, are available for applying lineal or point analysis to determine the surface area properties as well. [33]

2.3.4 Measured Stereological Parameters.

The geometric parameters measured by applying stereology are used to quantify the microstructure when comparing the simulation and experimental results. While there are several stereological parameters, the three most important independent parameters commonly reported in experimental studies examining the sintering process are: the solid volume per unit volume, V_V^S, the solid-solid surface area per unit volume, S_V^{SS}, and the solid-void surface area per unit volume, S_V^{SV}. Examples of how the stereological principles are used to determine each of these quantities in experimental studies is provided in the remainder of this section. In practice, the stereological measurements for experiments are conducted using computer software to analyze the pixels from scanned images of the sample surface to determine the quantities. Despite this, the basic measurement techniques commonly employed in experimental studies are essentially the same as described below.

2.3.4.1 Solid Volume Fraction. The solid volume fraction, V_V^S, is defined as the ratio of the volume occupied by the solid particles divided by the total volume considered. To measure this quantity, the stereological procedure is to superimpose a grid of evenly spaced points on the plane section being examined. This is illustrated in Figure 9. Some points (indicated by the red dots) will lie on a solid region (shaded grey) of the surface of the plane section while other points (indicated by the blue dots) will lie on the voids (the white regions) between the particles. The number of points lying on the solid phase is then counted. The solid volume fraction is the ratio

of the number of points lying on a solid region divided by the total number of points used in the grid (i.e. using the stereological relationship, $V_V{}^S = P_P{}^S$).

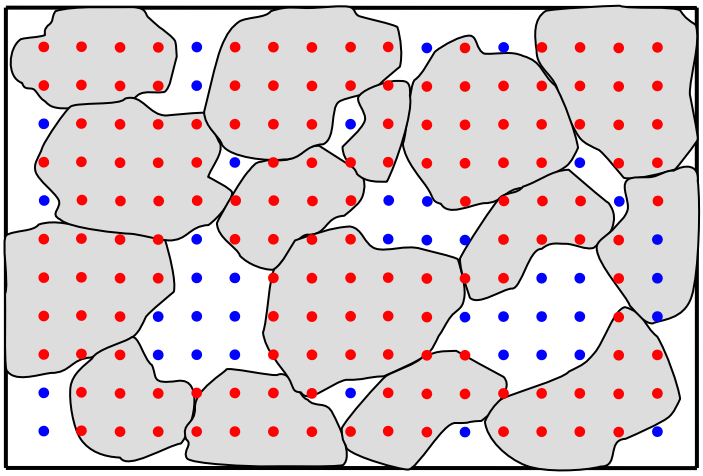

Figure 9. Measuring the solid volume fraction using stereology.

2.3.4.2 Solid-Solid Surface Area. The solid-solid surface area, S_V^{SS}, is defined as the surface area of contact between particles which overlap divided by the total volume considered. This quantity is usually measured using random chords placed along the surface of the sample plane section. As shown in Figure 10, the red line represents the measuring chord with the green dots indicating the points where the line crosses a solid-solid interface. The solid-solid surface area is equal to two times the ratio of the number of points on the chord intersecting a solid-solid interface divided by the total length of the chord (i.e. using the stereological relationship, $S_V{}^{SS} = 2 \cdot P_L{}^{SS}$).

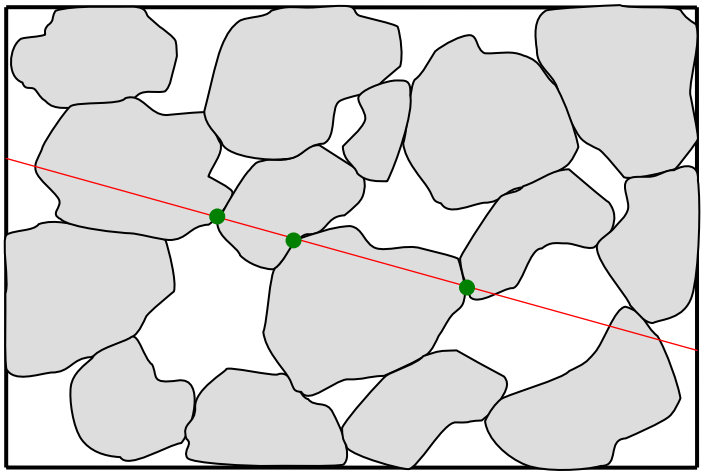

Figure 10. Measuring the solid-solid surface area using stereology.

2.3.4.3 Solid-Void Surface Area. The solid-void surface area, S_V^{SV}, is defined as the surface area of the particles exposed to voids divided by the total volume considered. This quantity is usually measured using random chords placed along the surface of the sample plane section. As shown in Figure 11, the red line represents a chord with the green dots indicating the points where the line crosses a solid-void interface. The solid-void surface area is two times the ratio of the number of points on the chord intersecting a solid-void interface divided by the total length of the chord (i.e. using the stereological relationship, $S_V{}^{SV} = 2 \cdot P_L{}^{SV}$).

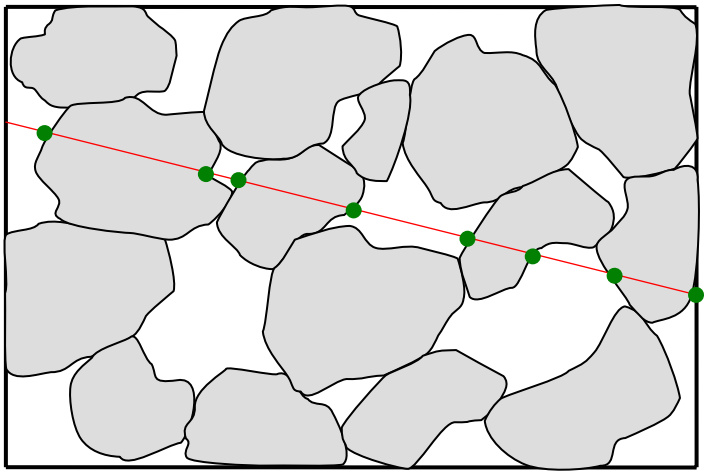

Figure 11. Measuring the solid-void surface area using stereology.

2.4 TESSELLATION

As noted in the previous section, stereological parameters (V_V^S, S_V^{SS}, and S_V^{SV}) are the traditional measurements used to quantify the characteristics of the microstructure for sintered materials. However, the information derived from the stereological parameters quantifies the properties for the overall volume only. This information may be insufficient to distinguish between two similar, but distinct, microstructures. For example, it is possible for two green compacts to have the same solid volume fractions (V_V^S), but different microstructures due to dissimilar particle packing arrangements — one green compact could have a uniform distribution of particles, while another has agglomerations of particles with larger voids interspaced between the clusters of particles. As a result, other means are required to identify the distinguishing characteristics of the

microstructure since the differences between the two compacts are only evident at a length scale different from the one at which the stereological parameters are measured. For such cases, another measuring method, tessellation, has been proposed as a means to provide additional information pertaining to the population distribution to differentiate the characteristics of the microstructures. [34, 35]

Tessellation is a technique used to uniquely segment an area into cells based on a feature of interest.[36] Tessellation separates the area, containing a spatial distribution of the feature, by establishing cell boundaries such that the positions inside a particular cell boundary are closer to the feature of interest contained within the cell than to any other point. Once the cell boundaries are established, the cell can then be characterized by determining cell parameters such as the area, the perimeter length, the aspect ratio and the number of adjacent cells. Tessellation can be applied for different features such as the location of the particle centers, the size of the particles, or the mass of the particles.[34-36]

The description of the tessellation presented below details how the technique is applied to characterize 2-D surfaces. The application of tessellation for two dimensions was chosen to allow the comparison of the simulation results to experimental data. Since the experimental data was obtained from the measurements taken from the surfaces of the samples, it was necessary to use a similar method to the simulation. However, it should be noted that the tessellation can be applied in three dimensions as well. Hence, when experimental techniques improve to permit the 3-D measurement of sintered objects, it will still be possible to adapt the tessellation technique to determine parameters to characterize the microstructure.

2.4.1 Point Tessellation

The simplest case to illustrate how tessellation is implemented is to consider point tessellation. In Figure 12, points A through H represent the features of interest located on a surface under examination. To construct the tessellation cell for point A, the surface is segmented by lines which bisect the distances between point A and its neighboring points B through H. For example, Line 1 bisects the distance between point A and point H. Completion of the process for all the points on the surface results in the outline of a shape enclosing each point on the surface. This shape is called a tessellation cell. The boundary of the tessellation cell surrounding point A is indicated by the dashed lines in Figure 12. Note the intersection of the boundary lines between points A and H and points A and E at the right corner of the cell. This intersection closes off the tessellation cell at this corner. This makes the boundary line between points A and G irrelevant since it does not contribute to the outline of the tessellation cell enclosing point A. Thus, it is omitted in Figure 12. The other interior solid lines represent the boundaries of the cells for the remaining points (B through H) on the surface.

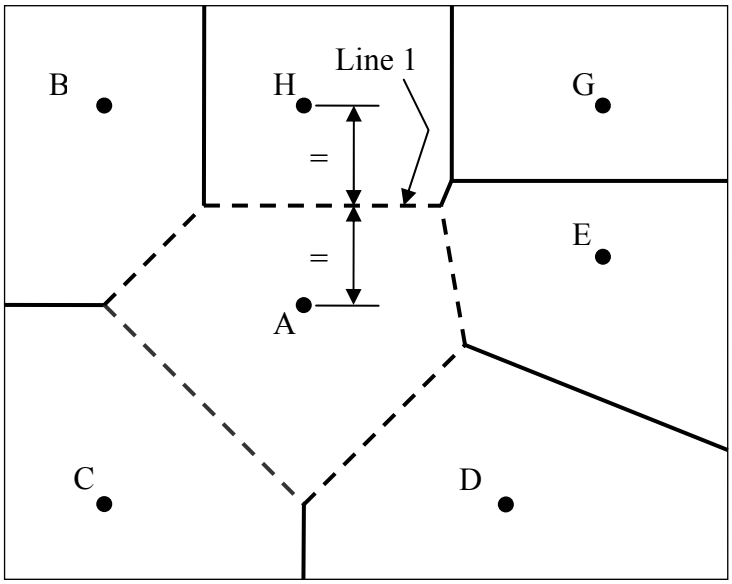

Figure 12. Illustration of how point tessellation is used to segment an area into cells.

2.4.2 Feature Tessellation

Tessellation can also be applied for features of interest on the surface instead of just points. Feature tessellation is implemented using the same basic method as described for point tessellation in the previous section. However, the size and morphology of the chosen feature will influence the size and the morphology of the resulting tessellation cells.[35-37] This is demonstrated by the example shown in Figure 13. In this case, the features of interest on the surface are the shaded regions bounded by a circle and a straight line. The resulting boundary for the tessellation cell, indicated by the dashed line, is a parabolic arc equidistant from the boundaries of the features. Since the tessellation cells are formulated from a feature of interest, the tessellation parameters can provide additional measurable quantities based on the selected feature of interest which can be used to characterize the microstructures of the sintered materials.

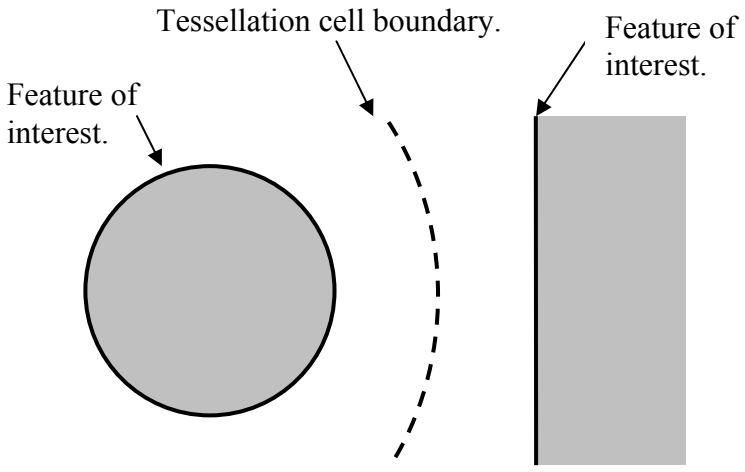

Figure 13. Influence of feature outline on the tessellation cell formation.

2.4.3 Solid Area Fraction (SAF)

When applying the tessellation technique to cross sections of sintered material samples, the feature of interest selected as the basis of the tessellation usually is the void space (i.e. the pores) between the particles. In the sample tessellation cell shown in Figure 14, the tessellation cell has two measures, the size of the pore contained inside the boundaries of the cell and the size of the cell itself, which are useful in quantifying the material being investigated. To allow comparisons between materials with different characteristic length scales and the model, the non-dimensional quantity solid area fraction (SAF) for a cell is defined, in terms of the cell area (CA) and the pore area (PA), as

$$SAF = 1 - (PA / CA). \qquad [2.4.3.1]$$

Thus, the solid area fraction is an indicator of the percentage of the tessellation cell area occupied by solid particles. The specific application of tessellation to the simulation is described in more detail in Section 3.5.2.

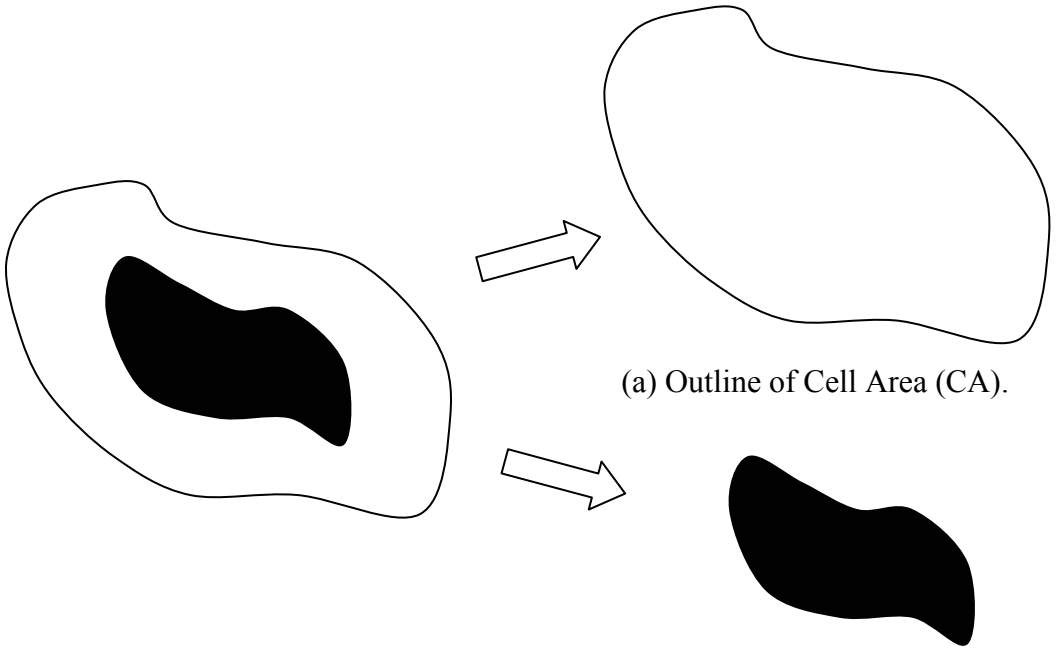

(a) Outline of Cell Area (CA).

(b) Pore Area (PA) contained inside the cell.

Figure 14. Pictorial of the Cell Area (CA) and the Pore Area (PA) for a tessellated cell.

3.0 MODEL DESCRIPTION

The essential feature of the simulation is the creation of the Representative Volume Element (RVE). The purpose of the RVE is to create a particle packing arrangement with geometrical properties which are statistically similar to the experimental properties obtained from measurements of real sintered materials. This section describes the details of the model formulation including the generation of the particle size distribution, the formation of the green compact, the creation of the RVE, the simulation of agglomerated packing arrangements, the methods used to simulate sintering, and the measurement techniques used to evaluate the model. The simulation was programmed in the C++ computer language and executed using Microsoft Visual C++ 6.0 on a personal computer. The images for the simulation results were generated using 3-D image rendering software package POV-Ray™.

3.1 GENERATION OF THE PARTICLE SIZE DISTRIBUTION

The particles comprising the RVE are modeled as spheres. The first step in the construction of the model is to create the distribution of particle sizes needed by the model to simulate the particle size distributions observed in real powders. While there are several possible distributions available to model particle sizes (the Weibull, Gamma, and Log-Normal distributions are the

more commonly employed options), experimental evidence indicates that many real powders have particle size distributions which fit a log-normal relationship [15, 16, 29] given by

$$p(r) = \frac{1}{\sqrt{2\pi}\cdot\sigma} e^{-\left[\ln(r)-\ln(\bar{x})\right]^2 / 2\sigma^2}$$

where r is the sphere radius, $\bar{x}$ is the median of the distribution, and σ is the standard deviation. Since it was the best fit to the experimental data chosen for comparison with the simulation, the log-normal distribution was used in the simulation. [29]

The generation of a random set of particle sizes with a log-normal distribution was done in two stages. First, a normal (Gaussian) distribution is created using standard program routines for the generation of random numbers.[38, 39] The normal distribution is then transformed into log-normal distribution using specified values for the mean and the standard deviation of the exponential function.[38] The generated log normal distribution was then normalized for comparison to the experimental particle size distribution. As shown in Figure 15, the simulation data fits the experimental data over most of the particle size distribution with only minor deviations at the extreme percentiles (<10% and >90%) of the distribution.

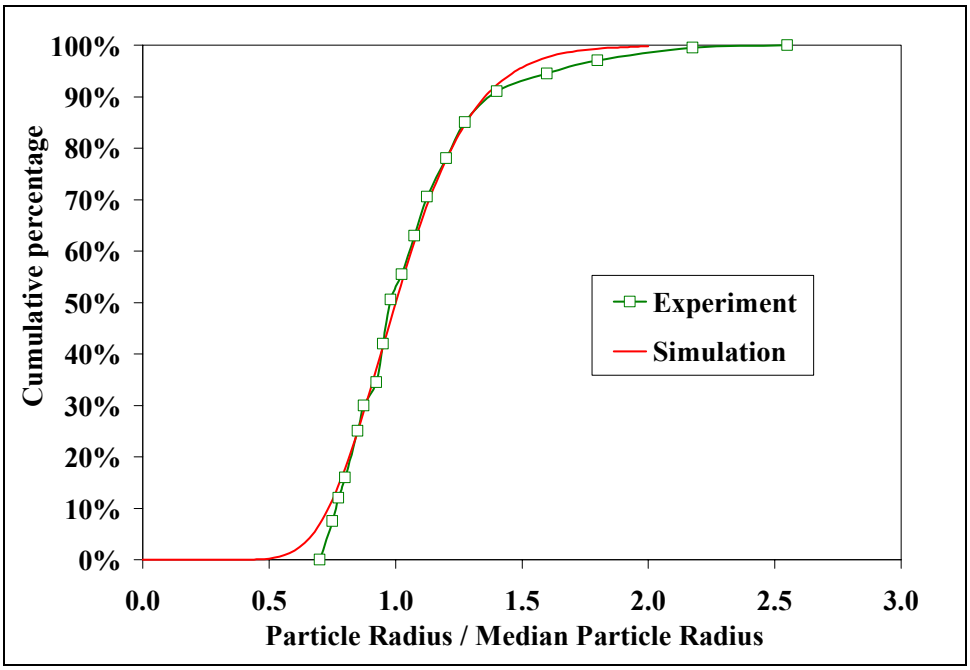

Figure 15. Comparison of simulation and experiment particle size distributions.

3.2 FORMATION OF THE GREEN COMPACT

After generating the particle size distribution, the next step is to place the particles into a volume to form the green compact. To do this, each particle is individually placed into a cubic virtual box. The particle center is initially assigned random *x* and *y* coordinates within the domain of the box but with a *z* coordinate greater than that of any of the other particles already in the box – Location 1 in Figure 16. From this initial location, the particle is then moved in the negative *z* direction to a plane just above the particles already in the virtual box – Location 2 in Figure 16.

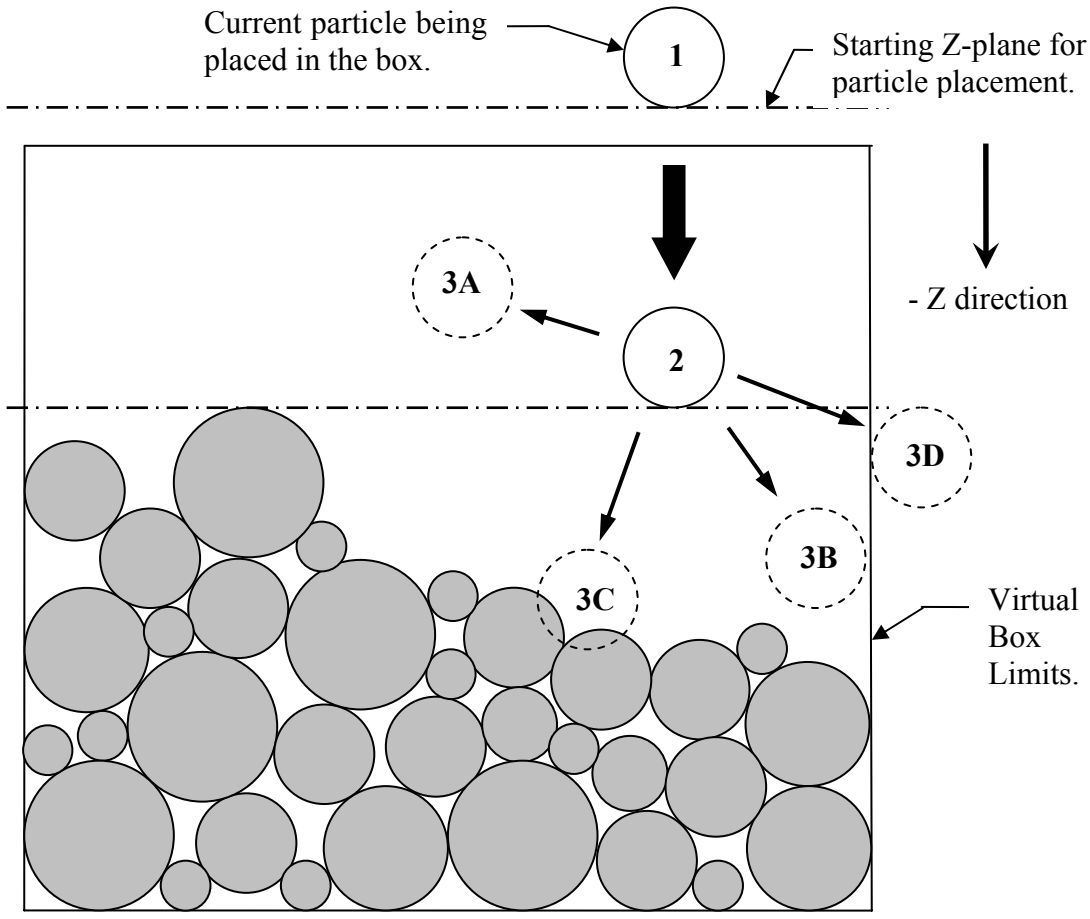

Figure 16. The placement of new particles into the virtual box.

From Location 2, the particle motion is controlled by a potential function. The potential of the particle is proportional to the "height" z, with a penalty applied for any overlap (i.e. physical interference) with other particles. The overlap ratio is determined from the distance between particle centers (*CDIST*) and the particle radii (R_i and R_j) as shown in Figure 17.

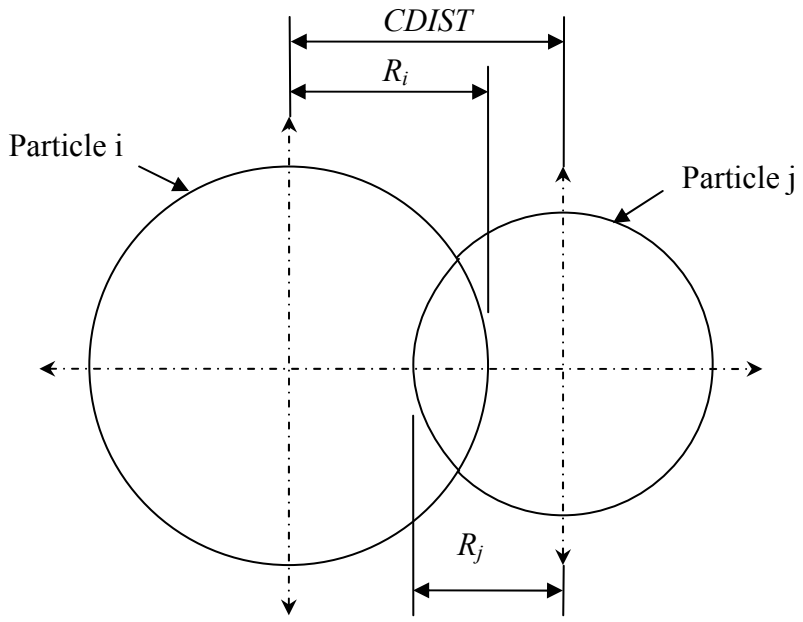

Figure 17. Geometry used to determine the overlap for a pair of particles.

The overlap ratio is the defined as,

$$OVERLAP_{ij} = \frac{R_i + R_j - CDIST}{R_i}.$$

The assessed penalty for overlap ratio is determined using a power law relationship,

$$PENALTY = C * (OVERLAP_{ij})^P,$$

where *PENALTY* is the contribution to potential function due to the overlap, *C* is a constant coefficient of penalty function, and *P* is a constant exponent for the penalty function. The amount of the applied penalty can be varied by specifying different values for constants *C* and *P*.

This provides the simulation with the capability of permitting smaller or larger overlaps as necessary to simulate the desired particle arrangement in the model. The particle's potential (ϕ_i) for a particular location is calculated by,

$$\phi_i = Z_i + \sum_{j=1}^{N} C * (OVERLAP_{ij})^P \ ,$$

where Z_i is the height of current particle inside the virtual box and N is the number of overlaps for the current particle with other particles already in the virtual box.

From Position 2, a random displacement of the particle less than some specified magnitude, *d,* is considered. Several new locations are possible for the particle – these are labeled 3A, 3B, 3C, and 3D in Figure 16. Location 3A has a greater potential since the new location is at a higher *z* position in the box. Location 3B has a lower potential due to a lower height and the lack of any overlap with other particles. Location 3C may have a lower potential due to a lower height, but the penalty for the overlap with other particles also has to be considered. If the new position reduces the particle's potential, then it is accepted; otherwise it is rejected. Location 3D would be rejected since it would place the particle outside the limits of the cubic box. This procedure is repeated until a specified number of consecutive rejections occur. The maximum random displacement *d* is then reduced and more random displacements are considered. By proceeding in this way, a local minimum of the particle's potential is approximated. The severity of the penalty for particle overlap, the number of consecutive rejections before moving on to a smaller value of displacement *d*, and the schedule of decreasing values of *d* are established via a trial and error balance between computational efficiency and the

desire to minimize particle overlap and maximize packing density. This procedure is repeated for each new particle until the virtual box is filled.

3.3 CREATION OF THE REPRESENTATIVE VOLUME ELEMENT (RVE)

From the set of particles in the filled virtual box, a subset of particles is obtained to create the Representative Volume Element (RVE). The 3-D image in Figure 18 shows the filled box for a simulation of approximately 14,000 particles with an average particle overlap of 0.5%. This particle arrangement has an initial green density of 0.61. The RVE is arbitrarily defined as a cube with unit volume. The limits defining the original cubic box are larger in size than the desired RVE by approximately 10% on each side. For those spheres that intersect the boundary of the RVE, only the portions inside the RVE are included, as shown in Figure 19. By making the RVE a smaller volume within the confines of the virtual box, the influence on the results caused by packing anomalies near the boundaries of the cubic box is minimized. Recent simulations have suggested that, for a log-normal distribution of sphere sizes, approximately 10,000 spheres are needed to generate reproducible values of the solid volume fractions.[15, 20]

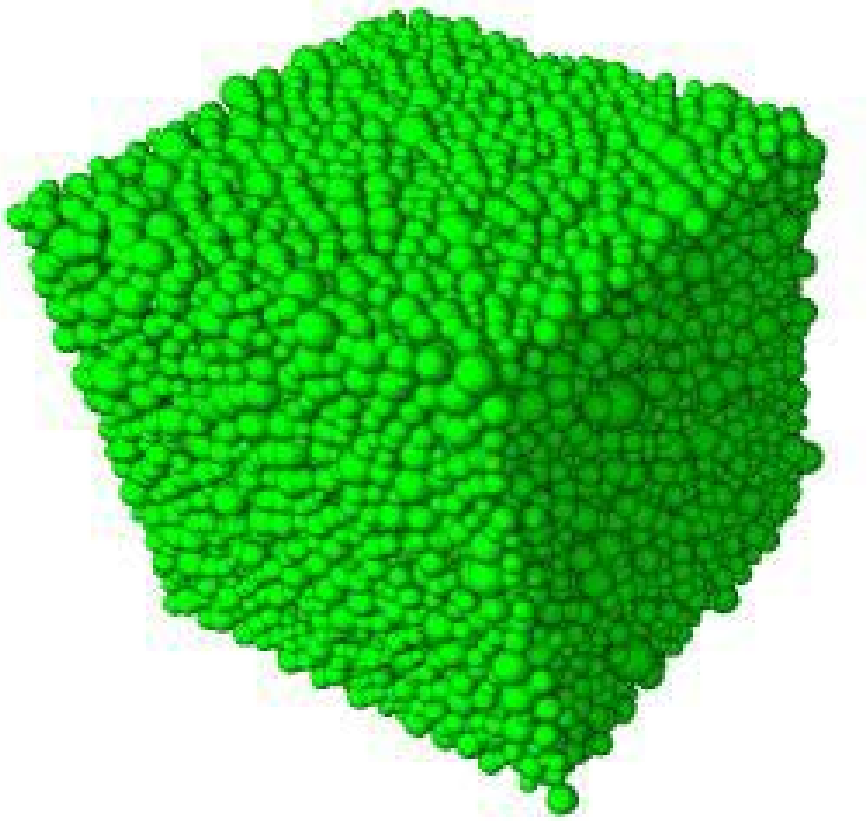

Figure 18. 3-D image of the filled virtual box generated by the simulation.

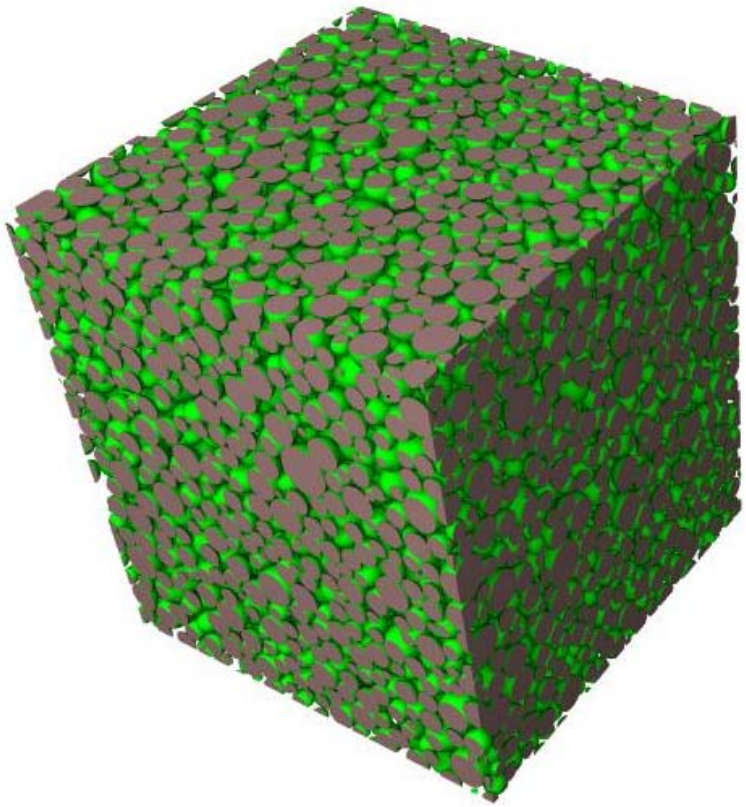

Figure 19. 3-D image of the Representative Volume Element (RVE).

3.4 SIMULATION OF AGGLOMERATIONS

For some materials, there is a tendency for the particles to agglomerate, or clump, as the initial green compact is formed. When this occurs, the result is a packing arrangement containing groups of closely packed particles with larger voids. Particle agglomeration is important when examining the behavior of sintered materials since the tails of the particle size distribution are critical factors in determining the relative densification and coarsening rates.[1] To replicate this phenomenon in the model, additional voids were created in the initial packing arrangement. This was done by selecting random points inside the virtual box and removing any particle intersecting with the point from the RVE. This creates additional voids in the original particle packing arrangement as shown in Figure 20. By varying the number of void creating points, it is possible to simulate agglomerated packing arrangements with voids of different frequency and size.

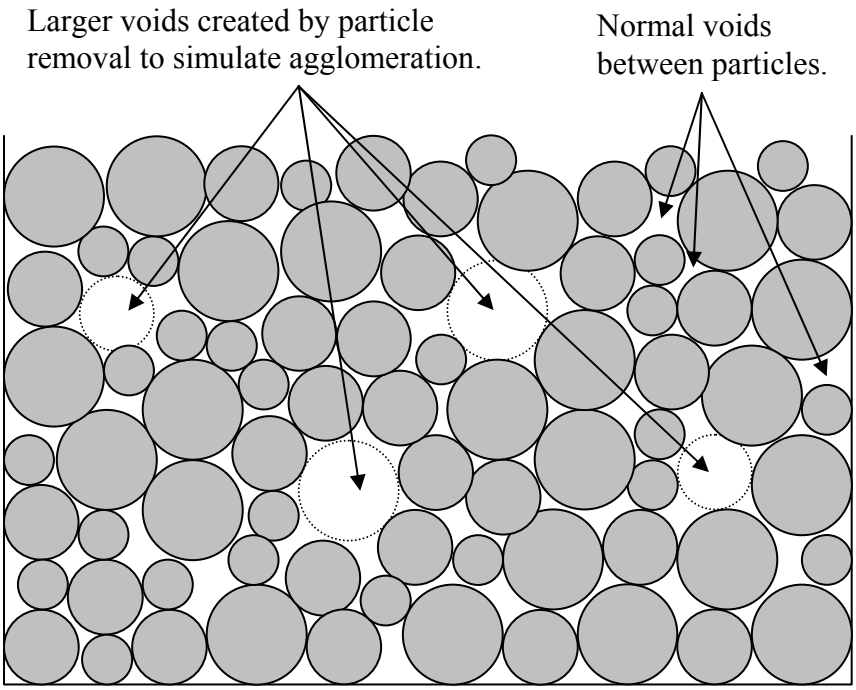

Figure 20. Random removal of spheres to create larger voids to simulate particle agglomeration.

3.5 SIMULATION OF SINTERING

After generation of the initial particle packing arrangement (i.e. the green compact), the next step in the model is to simulate the sintering process. As described in Section 2.1, there are several different approaches that have been proposed to model the behavior of sintered materials. In the present model, a technique defined as isotropic, homogenous sintering is initially used to simulate the densification of the particle packing arrangement. Sintering via Local Particle Rearrangement (LPR) was later implemented. The essential features of these methods are outlined in this section.

3.5.1 Isotropic, Homogenous Sintering

Densification occurs in the model by the self-similar reduction in distances between sphere centers to simulate uniform contact flattening. For the purposes of this investigation, this behavior is defined as isotropic, homogeneous sintering. This concept is illustrated by the interaction of a pair of particles modeled as spheres as shown in Figure 21. Initially, the particles have little or no contact as shown in Figure 21(a). Densification is simulated by the movement of the particle centers towards each other at a uniform rate as shown in Figure 21(b). The overlapping volume of the particles (indicated by the hatched regions) is assumed to be uniformly redistributed around the available solid-void surface area of the spheres resulting in an expansion of the particle radii (indicated by the dashed lines). The geometric relationships of the particles are then magnified to return to the original spacing between particle centers as shown in Figure 21(c). This magnification is permitted since the model is dimensionless due to the absence of material properties which would impose a length scale to the simulation. This process is implemented in the model by fixing the location of the particle centers while uniformly expanding the radii of the particles. This accomplishes the same net effect as the steps illustrated in Figure 21, but the procedure is computationally more efficient since the particle centers do not have to be moved. It is important to note that the time dependence of the sintering process and rearrangement of the particles were neglected. Consequently, the properties of the simulated material are not incorporated in this part of the simulation.

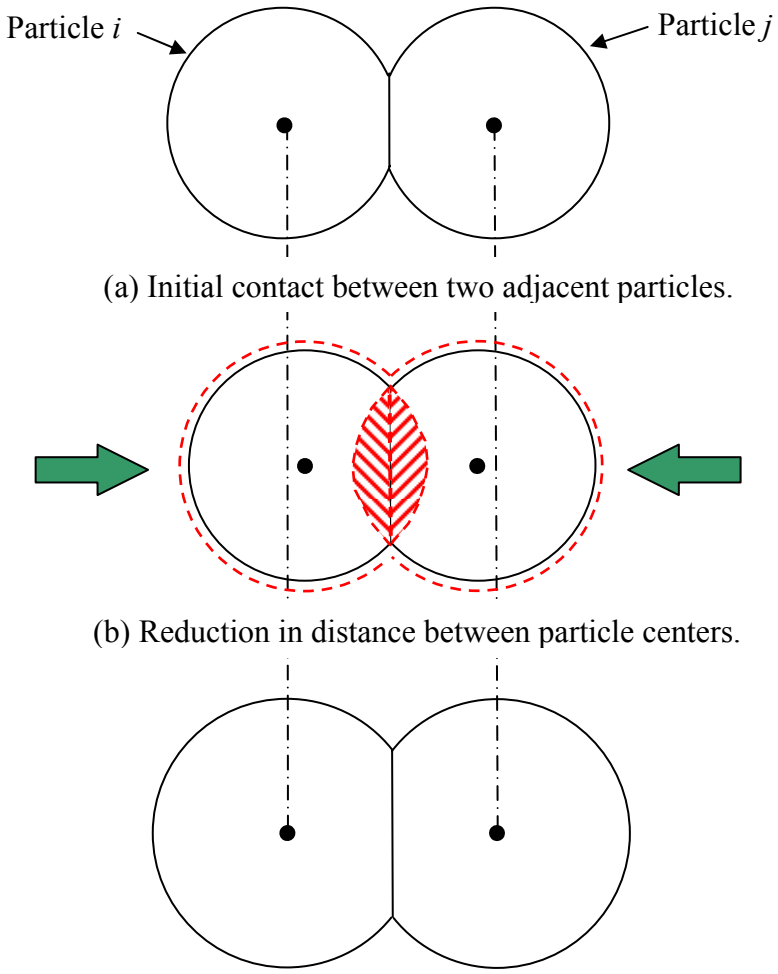

Figure 21. Graphical representation of isotropic, homogenous sintering.

3.5.2 Sintering with Local Particle Rearrangement (LPR)

The isotropic, homogenous sintering technique described in the previous section assumes that the particle centers move together at a constant rate. However, experimental evidence indicates that local rearrangement of the particle centers can occur during sintering. To simulate this behavior,

Local Particle Rearrangement (LPR) was incorporated into the simulation by modeling the particle arrangement as a viscous, porous medium.

To determine the motion of the particles, force and moment equilibrium is established for each sintering step. The conceptual basis for the force and moment equilibrium equations is described here; a step by step derivation of the equations for an overlap for a pair of particles is provided in the Appendix. When an overlap is present between a pair of particles, the contact force is resolved into a normal component to represent contact flattening and a tangential component to represent sliding along the grain boundary as shown in Figure 22.

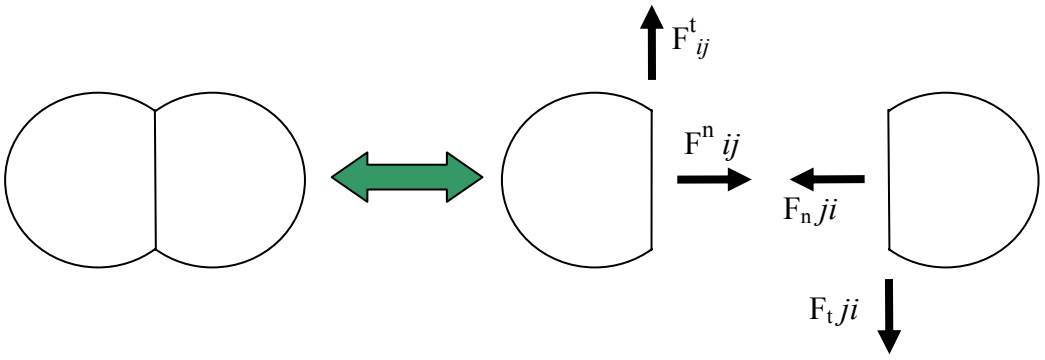

Figure 22. Free body diagram of the contact forces between two overlapping particles.

A linear relationship is assumed between the forces acting on the particles and the corresponding relative velocity of the particle centers. Densification occurs by assuming the particles centers move together at a constant rate - this is implemented in the simulation by applying a free centering velocity (V_0) to the centers of overlapping particles. The properties of the simulated material are introduced to the model using the shear and normal viscosities. The normal viscosity, μ^n, is defined as the relationship between the normal force per contact area and the normal component of the relative velocity. The tangential (or shear) viscosity, μ^t, is

defined as the relationship between the tangential force per contact area and the tangential component of the relative velocity. Normally, these material parameters are dependent on the sintering temperature and would be determined from experimental data for the sintering case being examined. However, for the purposes of this investigation, assumed values for the viscosities were used to explore their influence on the evolution of the microstructure.

Since each particle may have multiple contact surfaces, it is necessary to combine the equations for each individual overlap to determine the resultant force acting on a particular particle. The result is a system of linear equations which has to be solved for each time step in the sintering process. The system of equations is compiled for all the particles in the cubic volume (not just the RVE), hence individual particles are free to move into or out of the RVE. The linear system of equations is compiled into the matrix form $A \cdot X = B$ using the contributions of each overlap as derived in the Appendix. Matrix A contains the coefficients of the unknown variables in the system of equations. Vector X contains the unknown scalar components of the linear velocities (V) and angular velocities (ω) of all the particles in the cubic volume. For *n* particles in the cubic volume, there are 6*n* unknown variables – three scalar components to specify the linear velocity and three scalar components to specify the angular velocity for each particle. Vector B is essentially the forcing function and is based on the free centering velocity (V_0) which drives the sintering process in the simulation. The resulting matrix is of the form,

$$\begin{bmatrix} A_{11} & \vdots & A_{1N} \\ \cdots & \cdots & \cdots \\ A_{N1} & \vdots & A_{NN} \end{bmatrix}_{6nx6n} \begin{bmatrix} V \\ \cdots \\ \omega \end{bmatrix}_{6nx1} = \begin{bmatrix} f(V_0) \\ \cdots \\ 0 \end{bmatrix}_{6nx1}.$$

Since the equations of motion are based on the relative velocity between particles, boundary conditions are necessary to prevent rigid body displacement and rotation of the RVE.[40] The boundary conditions imposed were to set the linear and angular velocities to zero for the particle located at (or nearest to) the center of the RVE. The resulting physical behavior of the particles is illustrated in Figure 23. The green compact is an interconnected arrangement of particles with minimal overlap as shown in Figure 23(a). The particle highlighted in red identifies the particle at the center which is fixed to establish the boundary conditions. As sintering progresses, the particles collapse towards the fixed particle located at the center of the RVE as shown in Figure 23(b).

A LU Decomposition routine was used to calculate the solution to the system of linear equations. Once the velocities are determined, the locations of the particle centers are calculated for the time step, the stereological parameters are determined, and then a new system of equations is developed for the next specified time step. The process is repeated for the number of time steps needed to simulate full densification of the sintered material.

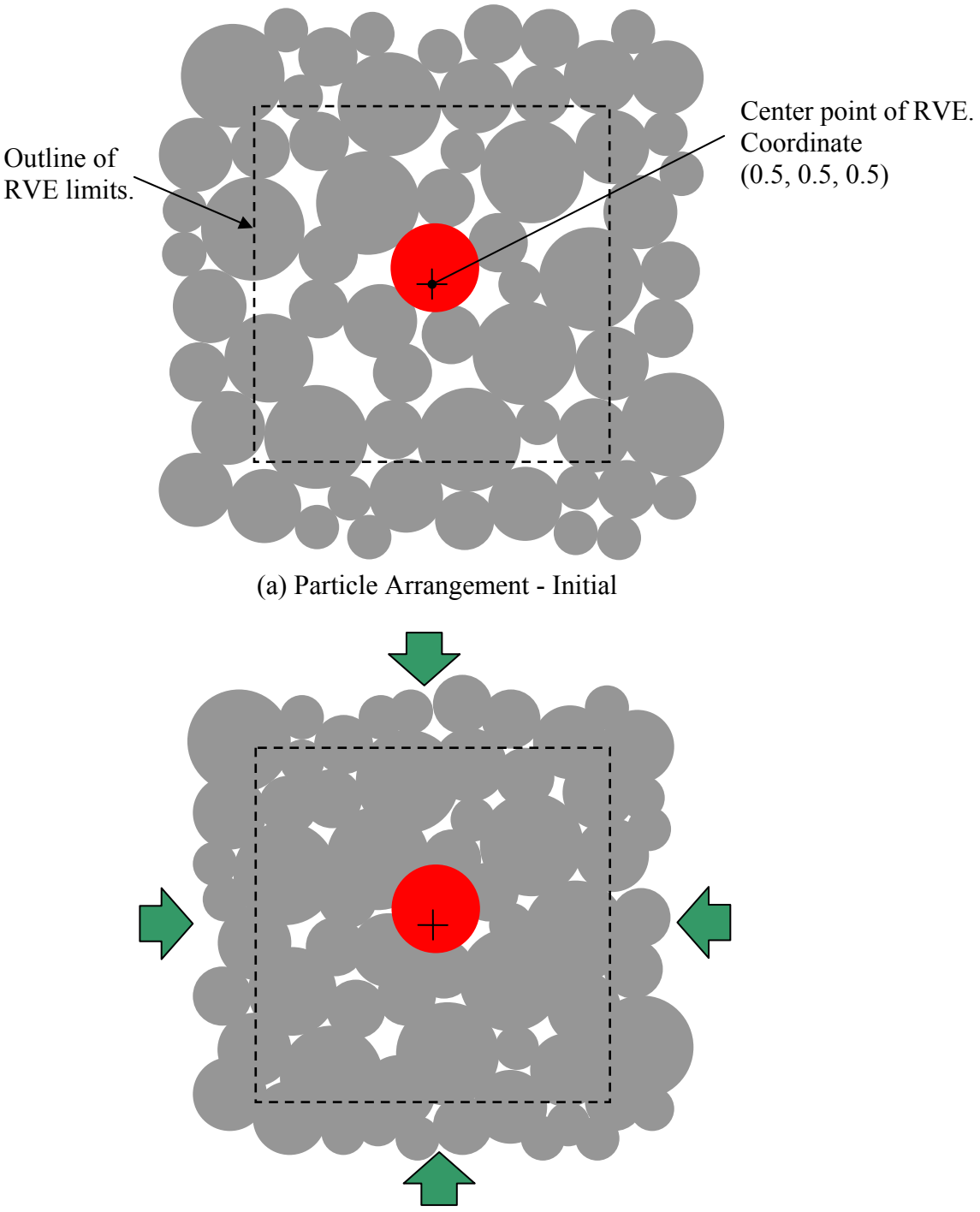

Figure 23. Sintering using Local Particle Rearrangement (LPR).

3.6 MEASUREMENT OF SIMULATION RESULTS

The evolution of the microstructure is monitored in the simulation using two measuring methods to determine the properties of the particles either entirely or partially inside the RVE for each step of the simulate sintering. The first method is the calculation of the stereological parameters. The second method is the application of tessellation to sections taken from the RVE. The application of each of these methods to the simulation is described in this section. It should be noted that these measuring methods function independently of the techniques used to simulate the sintering process. Hence, the measurements are the same for both the isotropic, homogenous sintering model (Section 3.5.1) and the sintering model with local particle rearrangement (Section 3.5.2), and can be applied to future sintering models.

3.6.1 Stereological Parameters

The evolution of the microstructure during the sintering process is simulated by the geometrical interaction of an assemblage of spheres which represent the particles comprising the compact. The model determines the same parameters used to quantify experimental samples of sintered materials: the solid volume fraction (V_V^S), the solid-solid surface area (S_V^{SS}), and the solid-void surface area (S_V^{SV}). Subroutines in the computer program are used to calculate these properties for the particles and the portions of the particles inside the limits of the Representative Volume Element (RVE). For each subroutine, a random number generator is used to create an even

distribution of points, either inside the volume (for V_V^S) or on the surface of the particles (for S_V^{SS} and S_V^{SV}), of the quantity to be measured. Then, acceptance / rejection criteria are applied to the points to ascertain the percentage of the feature which contributes to the global value of the quantity inside the RVE. In general, the accuracy of the calculation is related to the square root of the number of points considered. Detailed descriptions of the subroutines used to determine each parameter are provided below.

The accuracy of the calculations of each stereological parameter was estimated using several tests. The first test was to apply the program subroutines to the simple case of two, monosized overlapping spheres. The calculated values for the stereological quantities were compared to the results determined analytically using solid geometry. The second test was to vary the orientation of the second particle relative to the first particle to confirm that the calculations were not location sensitive. The final test was the simulation of isotropic, homogenous sintering using eight spheres with the sphere centers located at the corners of the RVE. Again, the results were confirmed for each sintering step using equations derived from analytic solid geometry. From the results of these tests, the minimum number of random points for each calculation was determined to ensure a deviation from the analytical results of less than 1%.

3.6.1.1 Determining the Solid Volume Fraction. The solid volume fraction, V_V^S, is the ratio of the volume occupied by the solid particles divided by the total volume of the RVE. The solid volume fraction is calculated for each sintering step in the simulation using Monte Carlo integration. Points are generated with random coordinates inside the limits of the Representative Volume Element (RVE). The location of each point is checked to determine whether it resides

inside the spherical volume for any particle, or portion of a particle, in the RVE. The ratio of the number of points residing inside any particle divided by the total number of points considered, $P_P^{\ S}$, determines the solid volume fraction, $V_V^{\ S}$ using the stereological relationship, $V_V^{\ S} = P_P^{\ S}$, derived in Section 2.3.3.

3.6.1.2 Determining the Solid-Void Surface Area. The solid-void surface area, S_V^{SV}, of a particle is the portion of a particle's surface area exposed to void space (i.e. not in contact or overlapping with any other particle). The model calculates the total solid-void surface area for all the particles and portions of particles inside the RVE for each step of the simulated sintering process. Figure 24 depicts the case of two overlapping particles - particle *i* is the current particle for which the solid-void surface area is being calculated and particle *j* is an adjacent particle which overlaps with the current particle. For this case, the shaded region (Ω_{INT}) indicates the portion of the surface area of current particle *i* which intersects with the overlapping particle *j*. The remaining surface area of particle *i* (Ω_{SV}) is the solid-void surface area for the current particle.

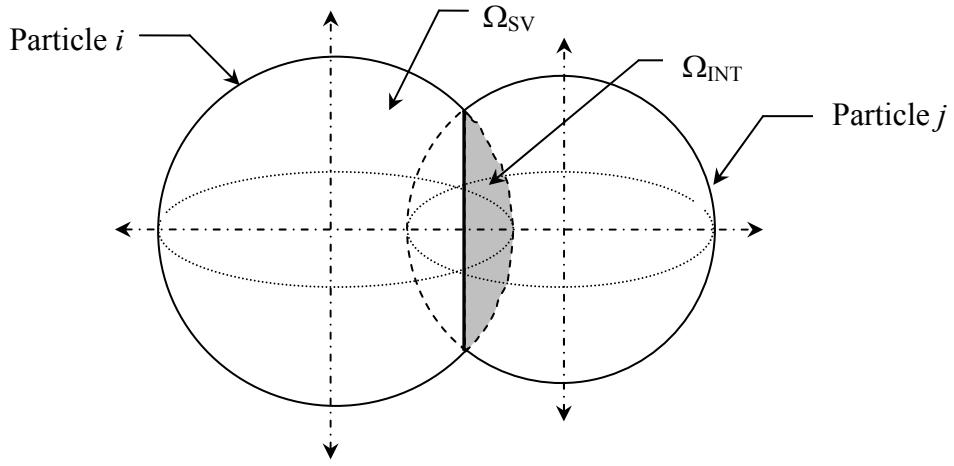

Figure 24. Particles modeled as overlapping spheres.

For the two sphere case illustrated in Figure 24, it is a simple task to determine S_V^{SV} using analytic geometry. However, if the current particle intersects with more than one mutually overlapping particle, it becomes difficult to calculate S_V^{SV} analytically. Consequently, a different approach to determining S_V^{SV} is needed. For the simulation, the Monte Carlo integration technique was adapted as the most efficient means to determine S_V^{SV}. To implement this technique, points are randomly generated on the surface of the sphere. Since the particles are modeled as spheres, spherical coordinates using randomized values of angles ϕ and θ were used to locate the points on the surface of the particle. A differential surface area element [(40)] is determined from the geometry shown in Figure 25.

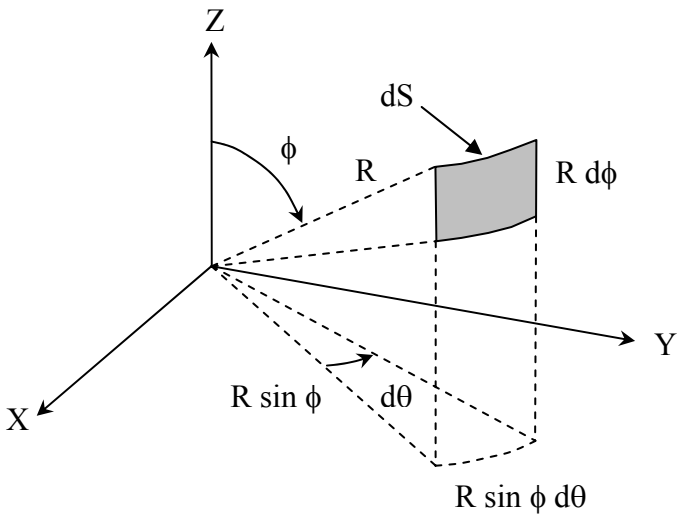

Figure 25. Differential surface area, *dS*, for a particle in spherical coordinates.

The differential area is given by $dS = R^2 \sin\phi d\phi d\theta$. The range of values for the randomized angles used to locate the points on the surface are,

$$0 \leq \phi \leq \pi \qquad \text{and} \qquad 0 \leq \theta \leq 2\pi.$$

This will generate an even distribution of points on the θ-ϕ plane. The location of each point is checked versus each particle overlapping with the current particle being considered. If the point is inside the volume of any other sphere, it does not contribute to the solid-void surface area. If the point lies outside any other sphere, it does contribute to the amount of the solid-void surface area. Computationally, this results in the following rule:

$$f(\theta,\phi) = R^2 \sin\phi \qquad \text{if } f(\theta,\phi) \in \Omega'_{SV}$$

$$= \quad 0 \quad \text{if } f(\theta,\phi) \notin \Omega'_{SV}.$$

The solid-void surface area for each particle is the sum of the contributions of the points outside any other sphere divided by the total number of points considered and is given by,

$$S^{SV} = \int_{\Omega_{SV}'} f(\theta,\phi) d\theta d\phi .$$

The solid-void surface area per unit volume, S_V^{SV}, is determined from the summation of the solid-void surface areas for all the particles and the portions of particles inside the RVE divided by the volume of the RVE.

3.6.1.3 Determining the Solid-Solid Surface Area. The solid-solid surface area, S_V^{SS}, is the portion of the surface area in contact with another particle for all the particles either entirely, or the portions of the particles, inside the RVE. Unlike the solid-void surface area, the solid-solid surface area is determined, not from the portion surface area of the sphere overlapping with other particles, but from the circular contact area of radius, rc, formed at the intersection of the overlapping spheres as shown in Figure 26.

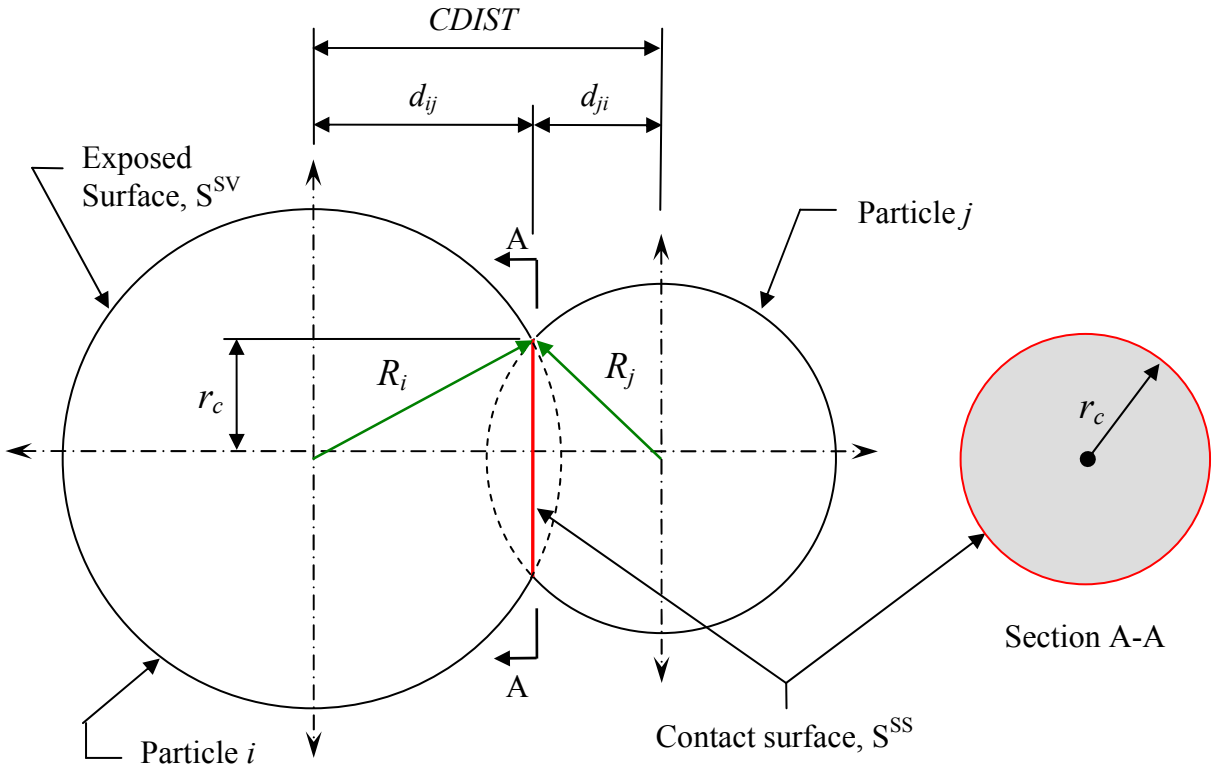

Figure 26. Contact surface area between two adjacent, overlapping spheres.

The equations used to determine the solid-solid surface area, S_V^{SS}, are derived using the distance between centers of the overlapping particles, (*CDIST*), the radius of contact (r_c), the radii of the particles (R_i and R_j) and the distances from the center of each particle to the contact surface (d_{ij} and d_{ji}). The following relationships are obtained from the geometry in Figure 26:

$$CDIST = d_{ij} + d_{ji} \qquad [3.6.1.3.1]$$

$$d_{ij}^{\,2} + r_c^2 = R_i^2 \qquad [3.6.1.3.2]$$

$$d_{ji}^{\ 2} + r_c^2 = R_j^2 \qquad [3.6.1.3.3]$$

If equations [3.6.1.3.2] and [3.6.1.3.3] are rearranged to solve for r_c^2, the equations can be set equal to each yielding the following,

$$r_c^2 = R_i^2 - d_{ij}^2 = R_j^2 - d_{ji}^2 \qquad [3.6.1.3.4]$$

Then, solving equation [3.6.1.3.1] for d_{ji} and substituting for d_{ji} in the right hand side of equation [3.6.1.3.4] results in the following expression,

$$R_i^2 - d_{ij}^2 = R_j^2 - \left(CDIST - d_{ij}\right)^2 \qquad [3.5.1.3.5]$$

Expanding the right hand side of equation [3.6.1.3.5],

$$R_i^2 - d_{ij}^2 = R_j^2 - \left(CDIST^2 - 2 \cdot CDIST \cdot d_{ij} + d_{ij}^2\right)$$

$$R_i^2 - d_{ij}^2 = R_j^2 - CDIST^2 + 2 \cdot CDIST \cdot d_{ij} - d_{ij}^2 .$$

The expression can be simplified by canceling like terms to give,

$$R_i^2 = R_j^2 - CDIST^2 + 2 \cdot CDIST \cdot d_{ij} .$$

This can be then solved for d_{ij},

$$2 \cdot CDIST \cdot d_{ij} = R_i^2 - R_j^2 + CDIST^2$$

$$d_{ij} = \left(R_i^2 - R_j^2 + CDIST^2\right) \Big/ 2 \cdot CDIST \,. \qquad [3.6.1.3.6]$$

Since R_i, R_j and $CDIST$ are all known quantities, the distances from the particle centers to the contact surface, d_{ij} and d_{ji}, can be determined analytically using equations [3.6.1.3.6] and [3.6.1.3.1]. Then, the contact radius, r_c, can be determined from either equation [3.6.1.3.2] or [3.6.1.3.3]. Finally, the contact surface area is calculated as the area of a circle using the contact radius.

However, for multiple, mutually overlapping spheres, the solid-solid surface area must be adjusted for the change in the geometrical relationships caused by the additional intersecting sphere(s). For the case of three mutually overlapping spheres shown in Figure 27, a portion of the circular contact area (the shaded region of Section B-B) between particles *i* and *j* has to be removed from the solid-solid surface area calculation to account for the overlap of the additional particle *k*. As the number of mutually overlapping spheres increases, it becomes increasingly difficult to use solid geometry to calculate the portion of surface area to remove due to the complexity of the geometry of the overlapping particles. To overcome this difficulty, a technique was developed to compute the correct solid-solid surface area utilizing Monte Carlo integration and vector algebra.

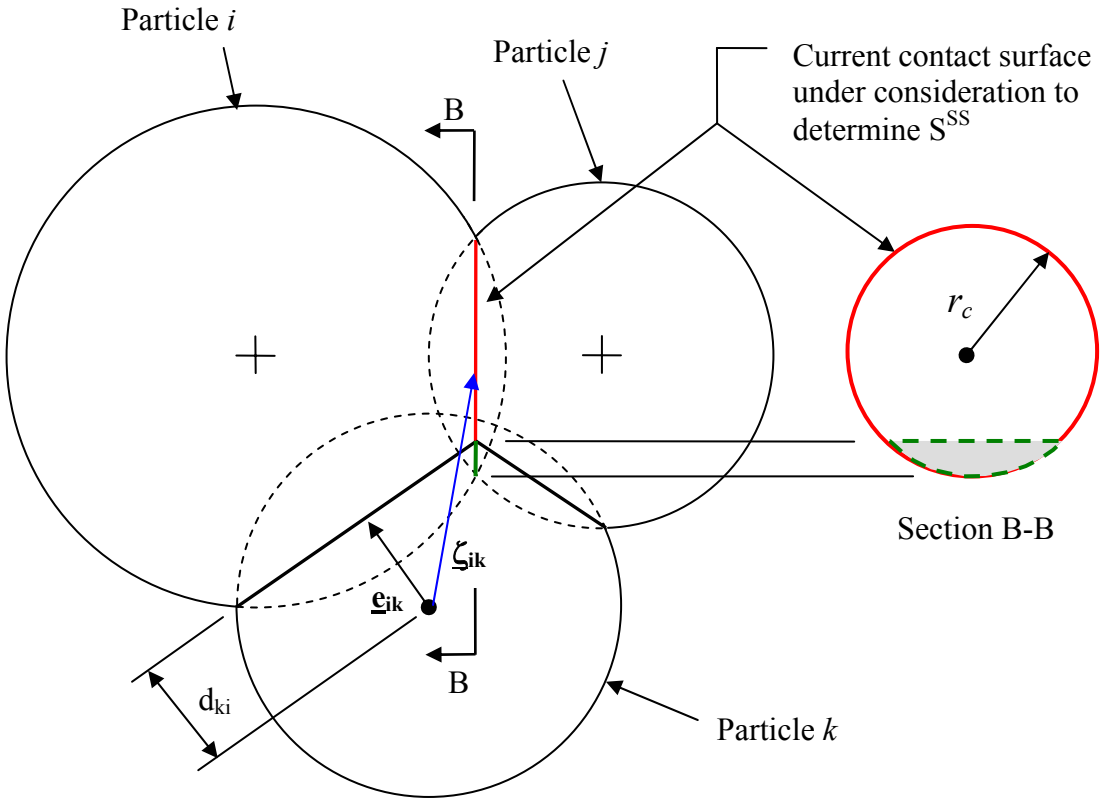

Figure 27. Geometric interaction between mutually overlapping spheres.

The procedure to do this begins by randomly generating an even distribution of points to represent the area of the contact surface between particles *i* and *j*. Vector algebra is then employed to ascertain what percentage of the points on the surface have to be rejected due to the overlap with particle *k*. The vector ($\underline{\zeta}_{ik}$) from the center of particle *k* to the location of each point representing the contact surface is determined. The dot product is used to calculate the projected distance of vector ($\underline{\zeta}_{ik}$) on the unit vector ($\underline{e}_{ik}$) identifying the direction from the center of the particle *k* to the center of particle *i*. If the resulting projected distance is less than the distance (d_{ki}) from the center of the particle *k* to its contact surface with particle *i*, then the point resides inside the overlap with particle *k* (i.e. the shaded region of Section B-B) and therefore the point

does not contribute to the solid-solid surface area. If not, the point is outside the contact surface of particle k and therefore the point does contribute to the solid-solid surface area. The points are also separately checked to reject any portion of the solid-solid surface area residing outside the limits of the RVE. Finally, the percentage of points accepted is multiplied by the area of the contact circle to determine the solid-solid surface area for the overlap. The procedure is repeated for each overlap. The results are summed to arrive at the solid-solid surface area for all the particles residing in the RVE.

3.6.1.4 Dimensionless Parameters. Traditionally, the stereological parameters described above are the measured quantities used to characterize the microstructure of sintered materials. However, given the range of particle sizes in the powder materials, it can sometimes be difficult to compare the microstructures of diverse sintered materials. Thus, to aid in comparing different microstructures, several non-dimensional parameters have been proposed to further analyze the evolution of the microstructure.(17, 23, 24) In particular, Krishnan et al.(17) have proposed using the fractional solid-solid surface area ($\overline{S}_V^{SS}$) and the fractional solid-void surface area ($\overline{S}_V^{SV}$). These parameters are determined from the measured S_V^{SS} and S_V^{SV}. The fractional solid-solid surface area ($\overline{S}_V^{SS}$) and the fractional solid-void surface area ($\overline{S}_V^{SV}$) are defined as,

$$\overline{S}_V^{SS} = \frac{S_V^{SS}}{S_V^{SS} + S_V^{SV}}$$

and,

$$\overline{S}_V^{SV} = \frac{S_V^{SV}}{S_V^{SS} + S_V^{SV}}.$$

Thus, the fractional solid-void and solid-solid surface areas represent the relative percentage of each quantity with respect to the other. Note also that, based on their definitions, $\overline{S}_V^{SS} + \overline{S}_V^{SV} = 1$.

3.6.2 Applying Tessellation to the Simulation

The stereological parameters provide information to quantify the overall properties of the RVE, but they may not provide sufficient information to distinguish between similar, yet distinct microstructures. Tessellation has been proposed as an additional tool to further quantify the microstructure of sintered materials [35, 37] since tessellation cells can be analyzed to obtain information related to the distribution of the particles inside the RVE. In experiments, tessellation is applied to the surface of samples taken from the sintered object using the pores as the feature of interest for determining the outline of the cell boundaries. As noted earlier, the size and shape of the pore areas will influence the size and shape of the resulting tessellation cell.

In a similar manner, tessellation can also be applied to 2-D cross sections, using image generating software POV-Ray™, taken from the 3-D Representative Volume Element for each step of the simulated sintering process. A sample cross section from a simulation with approximately 100 spheres inside the RVE is shown in Figure 28(a). In the cross section, the white regions are areas from the section occupied by solid particles; the black regions are void areas. The tessellation analysis applied to the cross section generates the tessellation cells based on the pores as the feature of interest. The result is the tessellated image shown in Figure 28(b) with the shapes of the tessellated cells distinguished by the different colors. To illustrate the

relationship between the feature (pores) and the shape of the cells, the outlines of the tessellated cells from Figure 28(b) are superimposed on the cross section as shown in Figure 28(c).

Tessellation can not always be freely applied to cross sections from sintered materials. The presence of the continuous pore network for low solid volume fractions can hinder the ability to segment the surface into tessellation cells. For example, if a group of pores are open to the edge of the examined area as shown by Region A in Figure 28(a), the number of tessellation cells obtained from the cross section as shown by Region B in Figure 28(b)] can be significantly reduced, thereby affecting the measurements. As a result, for practical measurements, tessellation is generally employed for higher ($V_V^S > 0.75$) solid volume fractions. This is a concern when applying tessellation to measurements of material samples as well as the cross sections taken from the simulation.

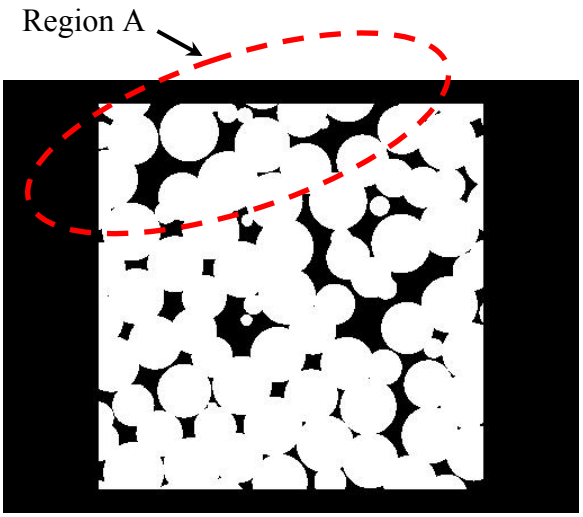

(a) Simulation cross section.

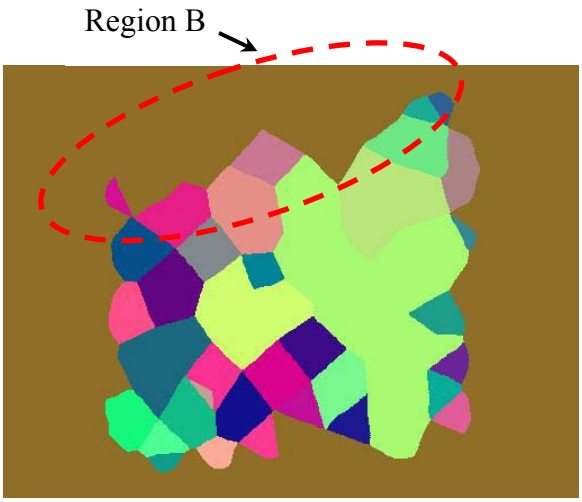

(b) Tessellated image showing cells.

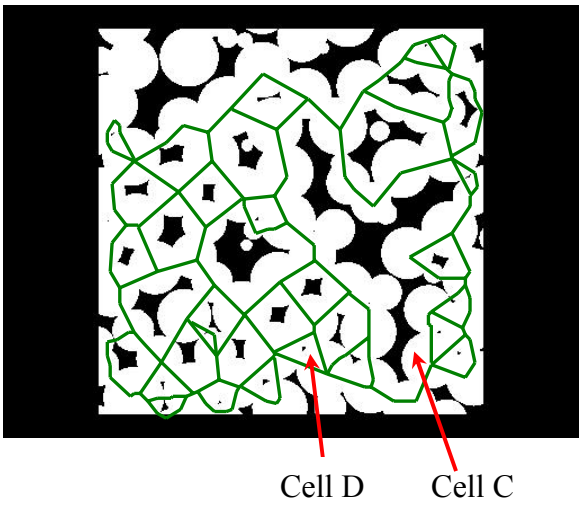

(c) Overlay of cell outlines from (b) onto (a).

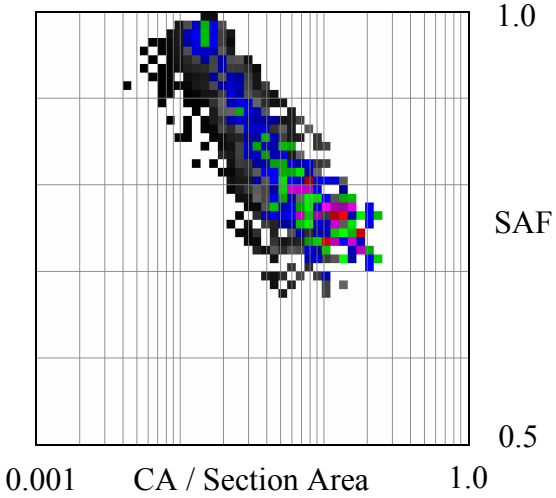

(d) 2-D SAF vs. CA / Section Area map.

Figure 28. Tessellation of RVE sections to form cells (for a simulation with 100 spheres in the RVE).

The RVE is systematically sampled using multiple cross sections taken at evenly spaced intervals in parallel X, Y and Z planes as shown in Figure 29. This is done to obtain sufficient statistical data to characterize the particle arrangement inside the RVE.

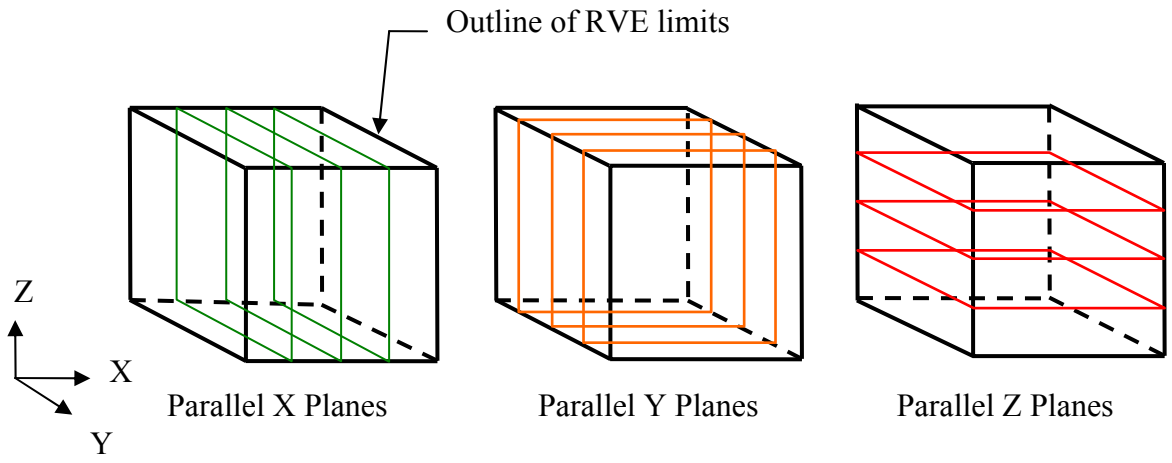

Figure 29. Sectioning the RVE for tessellation analysis.

The spatial data obtained from the analysis of the tessellation cells using these sections are tabulated and the resulting cell property distribution are plotted using the solid area fraction (SAF) versus the cell area (CA) per section area map as shown in Figure 28(d). This map is a graphical representation which displays the frequency of the tessellation cells (ranging from high frequencies for red areas to low frequencies for black areas) corresponding to the values of SAF and CA / Section Area for the cell characteristics used to quantify the microstructure. For each tessellated cell, the pore area (PA) and the cell area (CA) are determined and the solid area fraction (SAF) calculated for each tessellated cell. As shown by Cell C in Figure 28(c), the presence of the interconnected pore network can generate cells predominantly comprised of void space, resulting in a cell with a low SAF. On the other hand, even at low densities, small,

isolated pores can generate cells with a high SAF as shown by Cell D in Figure 28(c). By implementing this procedure for each step of the simulated sintering process, a series of maps are created for different solid volume fractions. The maps are analyzed to ascertain the behavior of the microstructure inside the RVE as densification progresses in the simulation.

3.6.3 Analysis of Microstructural Behavior Using SAF vs. CA Maps.

In order to use SAF vs. CA maps to analyze microstructural behavior during densification, it is necessary to understand the relationship between the measured parameters and the corresponding physical characteristics of the microstructure. The motivation for employing tessellation is to obtain data related to the population distribution which can be used to characterize the microstructure. Therefore, the frequency (or number of cells) corresponding to the different values of cell properties is crucial to the analysis. The best way to visualize the distribution of cell properties is to plot the data using a 3-D SAF vs. CA Map. A sample map from the simulation is shown in Figure 30(a). This map characterizes the microstructure by sorting the cells into the bins based on the values of the cell properties (i.e. SAF and CA). The data is then plotted using the SAF - CA plane to identify the measured characteristics of the cells. The frequency (or number) of cells corresponding to the properties are plotted orthogonal to the SAF - CA plane. The colors in Figures 30(a) and 30(b) specify the frequency range. In descending order, the frequency range is red (identifying the highest frequency), purple, green, blue, and black (identifying the lowest frequency).

While the 3-D SAF vs. CA Map is useful in visualizing the distribution of the tessellation cell properties, it is easier to use a 2-D SAF vs. CA Map to interpret the physical characteristics

of the microstructure. The 2-D SAF vs. CA Map corresponding to the data in Figure 30(a) is shown in Figure 30(b). The extreme combinations of the tessellation cell properties occur at the corners of the 2-D SAF vs. CA Map. Graphical representations for these combinations are labeled as Cell A, Cell B, Cell C and Cell D in Figure 30(b). These are:

- Cell A is small in size (low CA) with a relatively small pore yielding a high SAF.
- Cell B is large in size (high CA) with a relatively small pore yielding a high SAF.
- Cell C is small in size (low CA) with a relatively large pore yielding a low SAF.
- Cell D is large in size (high CA) with a relatively large pore yielding a low SAF.

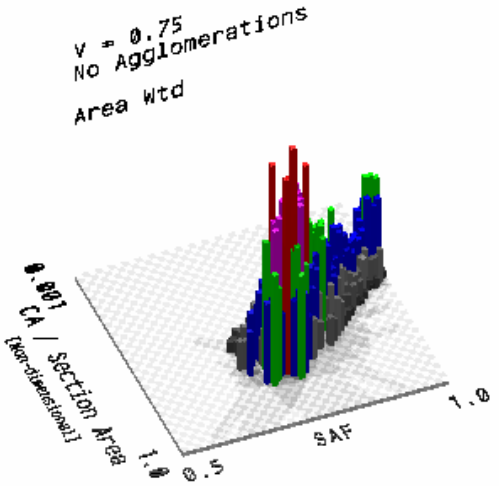

(a) 3-D Solid Area Fraction (SAF) vs. Cell Area (CA) Map.

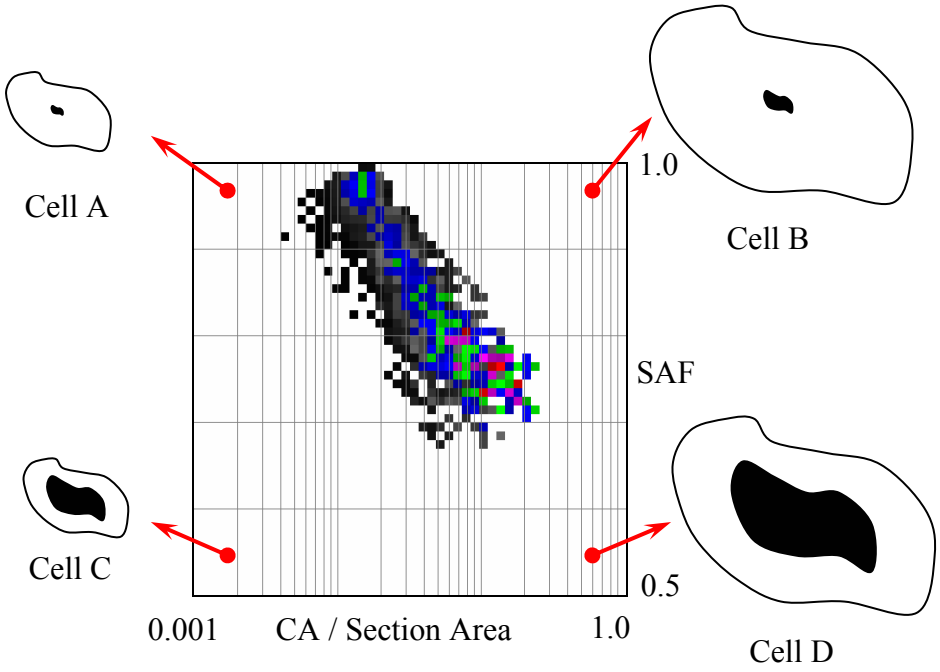

(b) 2-D Solid Area Fraction (SAF) vs. Cell Area (CA) Map.

Figure 30. Equivalent Solid Area Fraction (SAF) vs. Cell Area (CA) Maps for (a) 2-D and (b) 3-D.

An examination of the SAF versus the CA maps for the different solid volume fractions can provide insight into the physical behavior of the microstructure. McAfee *et al* [35, 37] have shown that the movement of the cells with the highest frequency (referred to as the peak) from one SAF versus CA map to another for different solid volume fractions can indicate trends in the general evolution of the microstructure. For this purpose, the 2-D SAF vs. CA map is generally employed since it is easier to plot the path of the changes in the peak and relate it to the measured cell properties.

When using the SAF vs. CA maps to interpret microstructural behavior, it is important to keep in mind that the tessellation cells are formulated based on the pores as the feature of interest. By rearranging equation 2.4.3.1, it is possible to express the pore area (PA) in terms of the cell area (CA) and the solid area fraction (SAF) using,

$$PA = CA \cdot (1 - SAF) . \qquad [3.6.4.1]$$

Using equation 3.6.4.1, lines of constant pore area (PA), called *isopore* lines, can be superimposed on the 2-D SAF vs. CA Map to assist in the interpretation of the microstructural behavior. It should be noted that the horizontal axis (CA) is a logarithmic scale indicating the order of magnitude of cell size while the vertical axis (SAF) is a linear scale indicating the relative size of the pore inside the tessellation cell. Because of this, the isopore lines have a logarithmic scale as indicated in Figure 31.

The principle directions of peak motion are shown on the sample 2-D plane of the SAF versus the CA/ Section Area shown in Figure 31. Movement of the peak in the direction indicated by arrow (a) is an increase in the solid area fraction (SAF) without a change in cell size

(CA). This results from a general decrease in pore size (i.e. shrinkage) in the microstructure. Movement of the peak in the direction indicated by arrow (b) is an increase in cell size (CA) without a change in solid area fraction (SAF). This may result from pore coalescence. Movement of the peak in the direction of arrow (c) is a decrease in cell area (CA) without a change in solid area fraction (SAF). This indicates the breakup of the pore sections. Movement of the peak in the direction indicated by arrow (d) indicates the shrinkage and/or the elimination of the pores. Movement of the peak in the direction indicated by arrow (e) indicates the breakup of the pores with pore shrinkage.

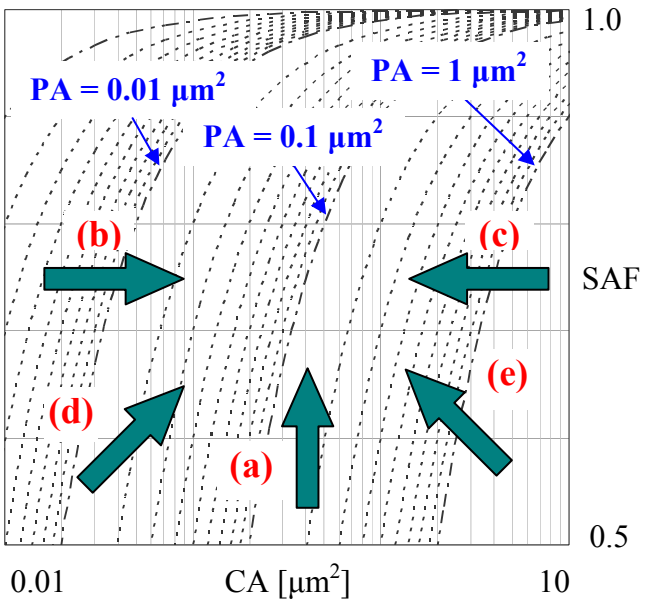

Figure 31. Monitoring peak motion to interpret the physical behavior of the microstructure. Arrow (a) is pore shrinkage, (b) is pore coalescence, (c) is pore break-up, (d) is pore shrinkage and elimination while (e) is pore break-up and shrinkage.

(Courtesy of the MSE Dept., University of Pittsburgh, McAfee[37])

4.0 EXPERIMENTAL DATA

Since the purpose of the proposed model is to simulate the behavior of real sintered materials, it is important to note the general trends observed in the experimental data in order to properly evaluate the simulation results. To obtain the necessary information for comparison to the simulation results, the author has relied upon the work of others for the experimental data and images presented in this section. In particular, the primary experimental data used for comparison to the simulation results were obtained from the studies of alumina samples conducted at the University of Pittsburgh by Krishnan, et al [17] and McAfee [35, 37]. Other published studies by Shaw and Brook[42] on the grain coarsening of alumina powder, a study by Aigeltinger and DeHoff[43] on the sintering of spherical copper powders, and a study by Aigeltinger and Exner[44] are also cited.

In general, experimental data is obtained from an analysis of digital images taken from scans of the sample surface. Scanning Electron Microscopy (SEM) is typically used generate a grayscale micrograph of the sample surfaces similar to the image shown in Figure 32. The specific details of the step-by-step experimental procedure are omitted here, but they are described by McAfee[35] (p.50-51).

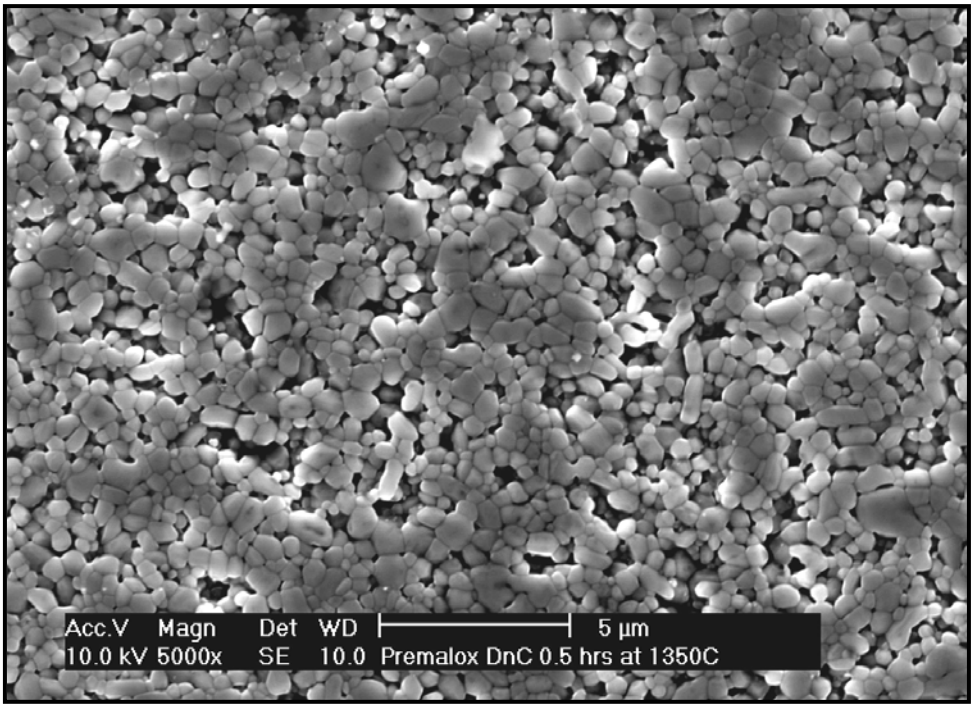

Figure 32. SEM micrograph of sintered alumina - dispersed case.
(Courtesy of the MSE Dept., University of Pittsburgh, McAfee[35], p. 4)

For this investigation, the primary sources of experimental data used for comparison to the simulation results are the studies by Krishnan [17] and McAfee [29, 35, 37] conducted on alumina samples. The particle size distribution measured in these studies [29] was used as the benchmark for the simulation particle size distribution as outlined in Section 3.1. These investigations examined two different arrangements of alumina powder – referred to as the *dispersed* and *flocculated* cases. Examples of the scanned images obtained from experimental samples are shown in Figure 33 for the dispersed alumina and Figure 34 for the flocculated alumina. A comparison of these two images shows that the dispersed sample has a more uniform distribution

of the alumina particles than the flocculated sample which has a more agglomeration (i.e. there are regions of closely clumped particles interspaced with pores which are relatively larger in size than the dispersed case). Computer programs are employed to analyze the pixels of the scanned grayscale images like the examples shown in Figure 33 and Figure 34 to determine the stereological parameters and the population distributed properties of the tessellation cells.

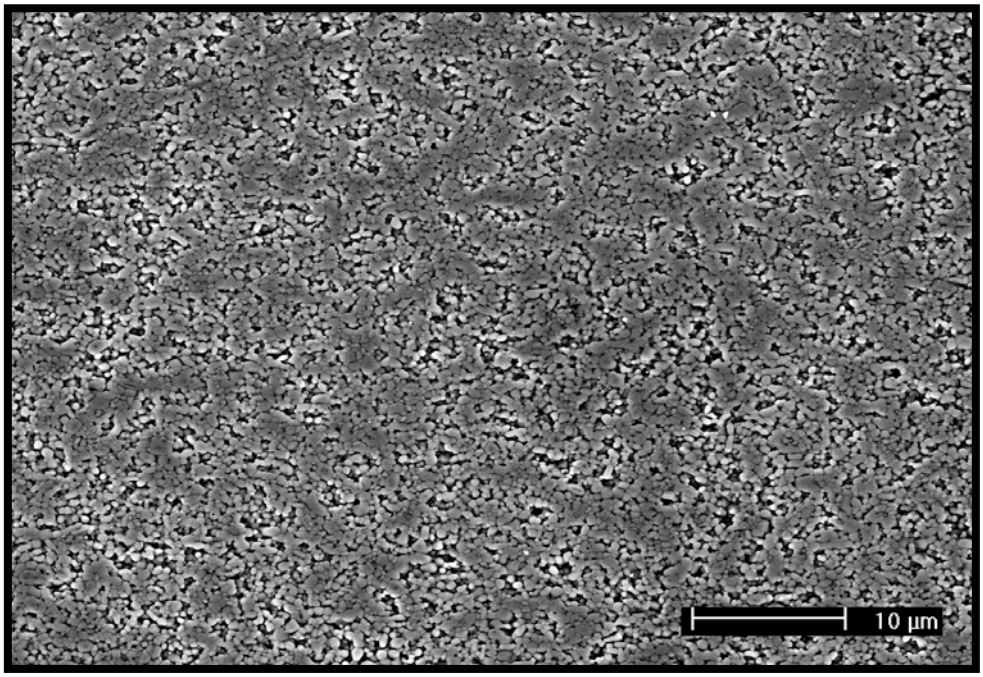

Figure 33. SEM Micrograph of dispersed alumina sintered for 0.6 hours at 1350 °C with V_V^S =0.87. (Courtesy of the MSE Dept., University of Pittsburgh, McAfee[35], p. 79)

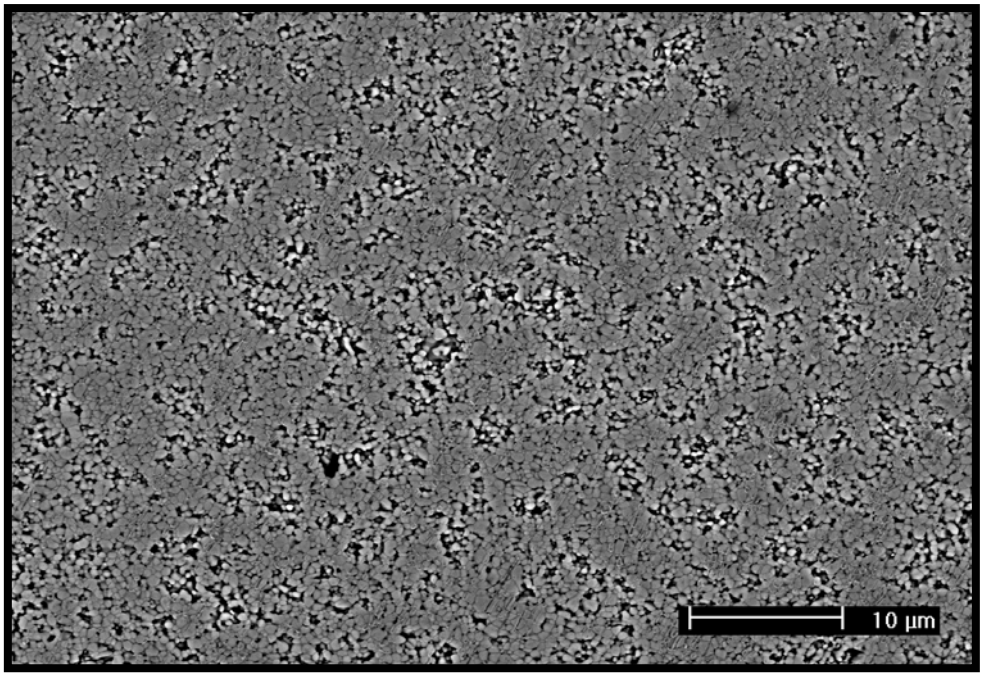

Figure 34. SEM Micrograph of flocculated alumina sintered for 1.1 hours at 1350 °C with V_V^S = 0.85. (Courtesy of the MSE Dept., University of Pittsburgh, McAfee[35], p. 79)

4.1 PLOT OF $\overline{S}^{SS}$ vs. V_V^S CURVES – EXPERIMENTS

The first method used to evaluate the experimental samples was the determination of the stereological parameters — the solid-solid surface area per unit volume, S_V^{SS}, the solid-void surface area per unit volume, S_V^{SV}, and the solid volume fraction, V_V^S. As noted earlier, the main experimental data used for comparison to the simulation results are the studies by Krishnan [17] and McAfee [29, 35, 37] for alumina powders. There are also other studies published in the literature on the behavior of sintered materials. Unfortunately, many of the studies do not report sufficient

information on the stereological parameters (i.e. the values for S_V^{SS} and S_V^{SV} as a function of V_V^S) to allow the calculation of the fractional solid-solid surface area. The primary difficulty is that most studies present their measurements of the sample surfaces in terms of the grain size or pore size as a function of V_V^S. As noted by Nettleship, *et al* [45], it is not possible to distill the measured stereological quantities (S_V^{SS} and S_V^{SV}) solely from the reported data. Since the fractional solid-solid surface area, $\overline{S}^{SS}$, cannot be determined without this information, this precludes a comparison of the experimental data to the simulation results. However, there are a few studies which do report measured values of S_V^{SS} and S_V^{SV}: a study by Shaw and Brook[42] on the grain coarsening of alumina powder, a study by Aigeltinger and DeHoff[43] on the sintering of spherical copper powders, and a study by Aigeltinger and Exner[44] examining copper structures. The experimental data reported in these studies are used to determine the fractional solid-solid surface area as a function of the solid volume fraction and added to the data from Krishnan [17] and McAfee.[29, 35, 37] The results from these studies are plotted in Figure 35.

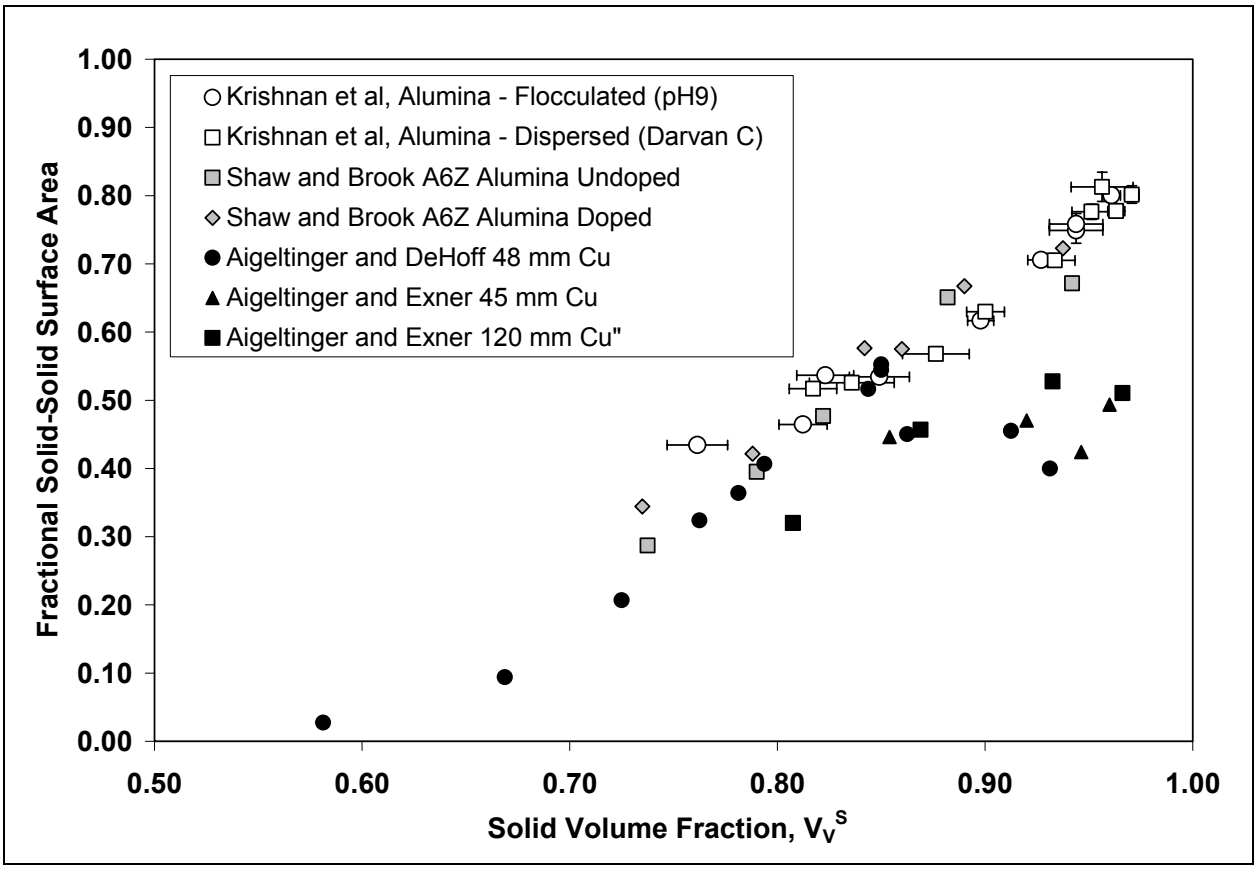

Figure 35. Plot of $\overline{S}^{SS}$ vs. V_V^S for experimental data.

Some general observations can be made from the experimental data presented in Figure 35. First, the general trend for the experimental data is an increase in the fractional solid-solid surface area, $\overline{S}^{SS}$, as the solid volume fraction, V_V^S, increases. This results from the relative increase in the solid-solid surface area and the relative decrease in solid-void surface area due to contact flattening and the reduction in particle center distance which typically occurs as densification progresses during the sintering process. Second, the slopes of the $\overline{S}^{SS}$ vs. V_V^S curves are not necessarily constant. The results for the alumina samples reported by Krishnan *et al* [17] show an increase in the slope of the curve while the slopes of the curves decreased for the

other studies at higher densities (V_V^S>0.88). The change in slope at higher densities is more prominent for the copper data reported by Aigeltinger and DeHoff[43] and Aigeltinger and Exner[44] than for the alumina data reported by Shaw and Brook[42]. The change in the slope of the $\overline{S}^{SS}$ vs. V_V^S curves may provide insight to the behavior of the microstructure. The key to interpreting the behavior of the microstructure from this data is based on the change in S_V^{SS} and S_V^{SV}. A decrease in the solid-solid surface area, S_V^{SS}, would imply the presence of grain growth while a decrease in the solid-void surface area, S_V^{SV}, would imply pore coarsening.

4.2 TESSELLATION RESULTS – EXPERIMENTS

The second method used to evaluate the experimental samples was the employment of tessellation to generate data characterizing the population distribution. McAfee[35] applied tessellation to the dispersed and flocculated alumina samples. The grayscale scanned images of the sample surface, similar to the examples shown in Figure 33 and Figure 34, are processed to generate a black and white image of solid particles (white) and pores (black). Boundary tessellation is then applied to the black and white image to generate cells based on the pores as the feature of interest. Figure 36 shows an example of the outlines of the tessellation cells superimposed on the original grayscale image used to generate the cells.

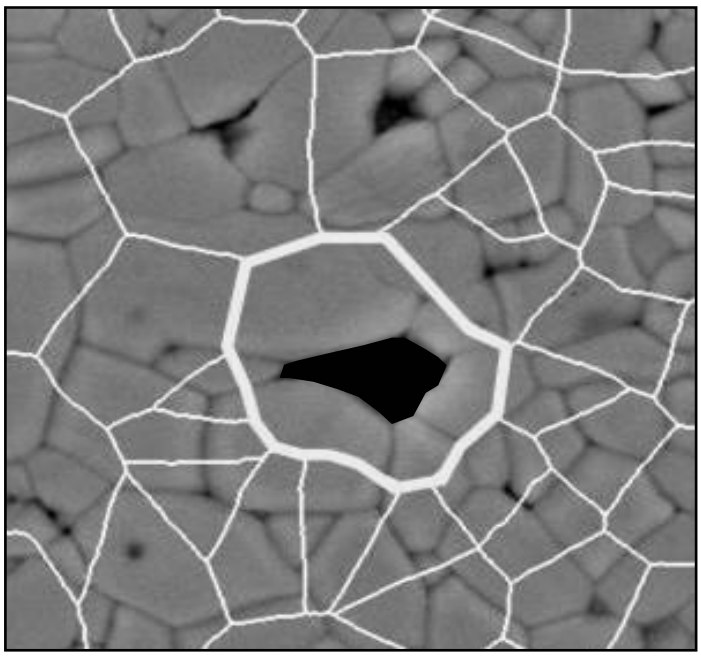

Figure 36. A scanned image of the pore structure with outlines of the tessellation cells superimposed. (Courtesy of the MSE Dept., University of Pittsburgh, McAfee [37])

Figure 37 shows a processed image with the tessellation cells (the colored regions) superimposed over the black and white image showing the pores (black). It is important to note that the pores near the edges of the image are not included in the statistics since it is not possible to calculate the outline of the boundaries needed to completely enclose the pores at the edges inside a tessellation cell.

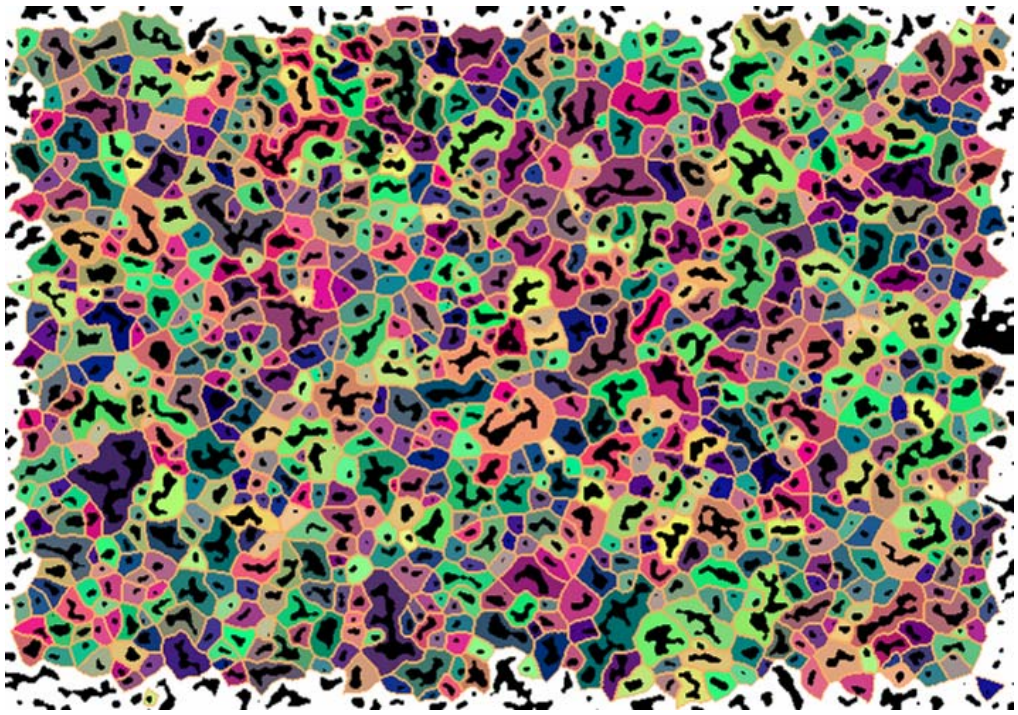

Figure 37. Tessellated image of the black and white SEM micrographs.
(Courtesy of the MSE Dept., University of Pittsburgh, McAfee[35], p. 101)

After tessellation of the image, the cell area (CA) and the solid area fraction (SAF) are calculated for each cell generated from the scanned image. The distribution of the cell properties are then graphed using either the 2-D or 3-D SAF vs. CA Map. McAfee [35] applied tessellation to scanned images of samples of the dispersed and the flocculated cases for alumina powder. The results for the dispersed alumina case are shown in Figure 38 for different solid volume fractions using 3-D SAF vs. CA Maps. The results for the flocculated alumina case are shown in Figure 39 for different solid volume fractions using 3-D SAF vs. CA Maps. The data for the flocculated alumina case presented in Figure 39 are also shown using the 2-D SAF vs. CA Maps in Figure 40 with the peaks enclosed by the red lines.

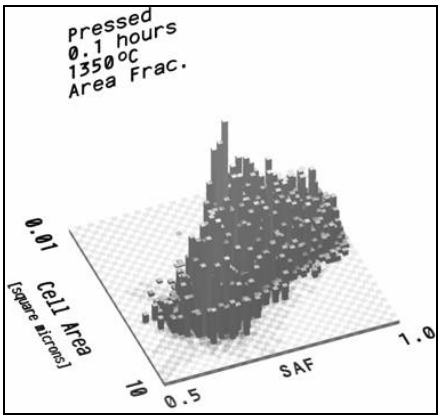

(a) $V_V^S = 0.82$

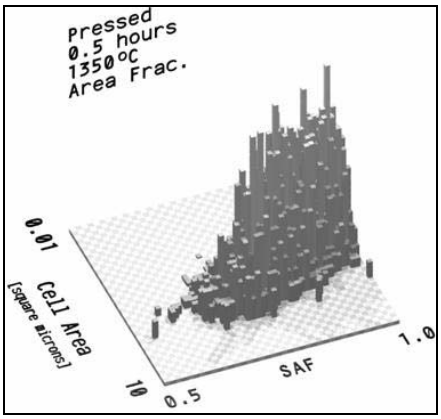

(b) $V_V^S = 0.82$

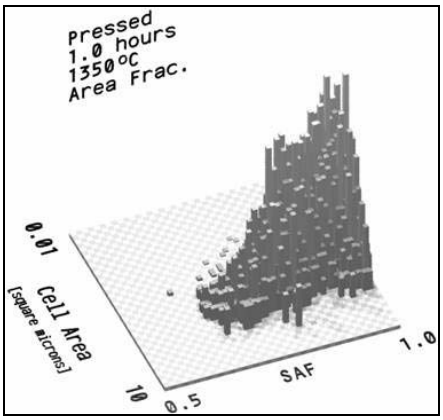

(c) $V_V^S = 0.87$

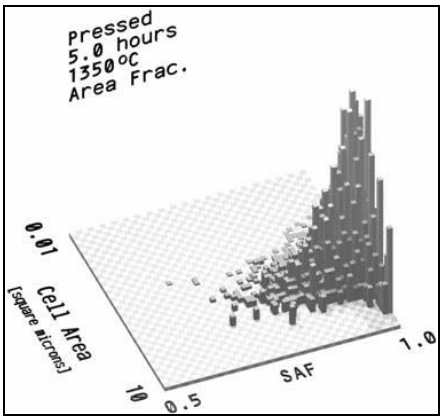

(d) $V_V^S = 0.93$

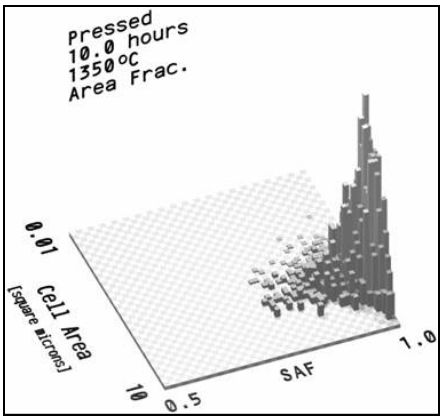

(e) $V_V^S = 0.95$

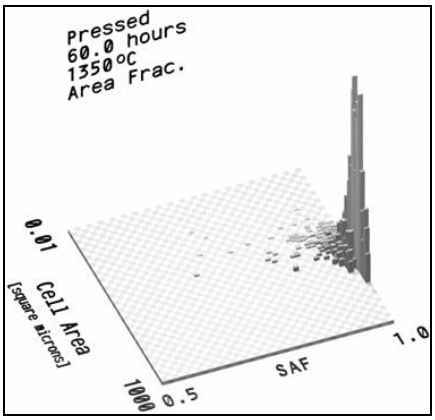

(f) $V_V^S = 0.96$

Figure 38. 3-D SAF vs. CA Maps for dispersed alumina samples.
(Courtesy of the MSE Dept., University of Pittsburgh, McAfee[35], p. 114)

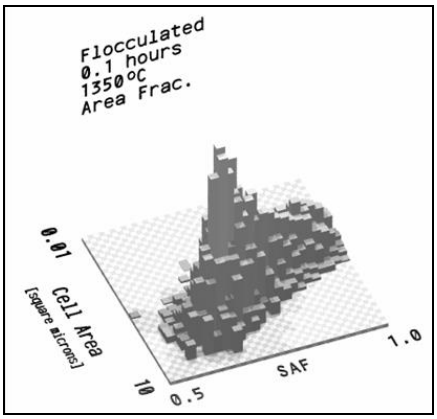

(a) $V_V^S = 0.75$

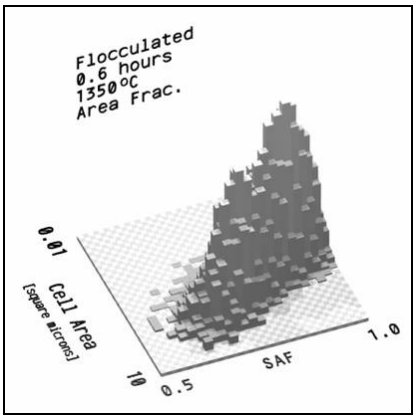

(b) $V_V^S = 0.825$

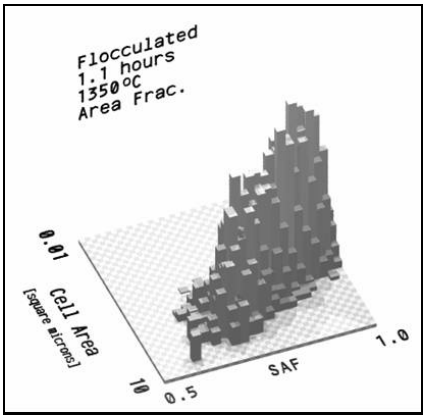

(c) $V_V^S = 0.85$

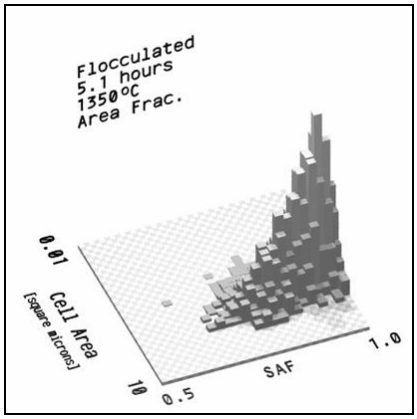

(d) $V_V^S = 0.90$

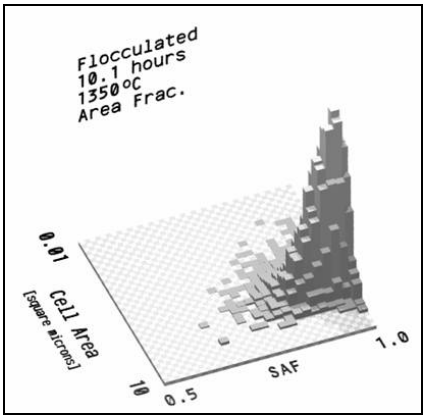

(e) $V_V^S = 0.95$

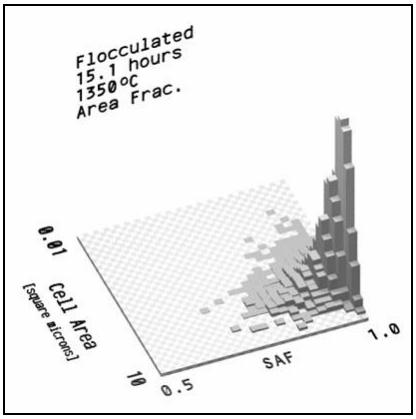

(f) $V_V^S = 0.95$

Figure 39. 3-D SAF vs. CA Maps for flocculated samples.
(Courtesy of the MSE Dept., University of Pittsburgh, McAfee[35], p. 114)

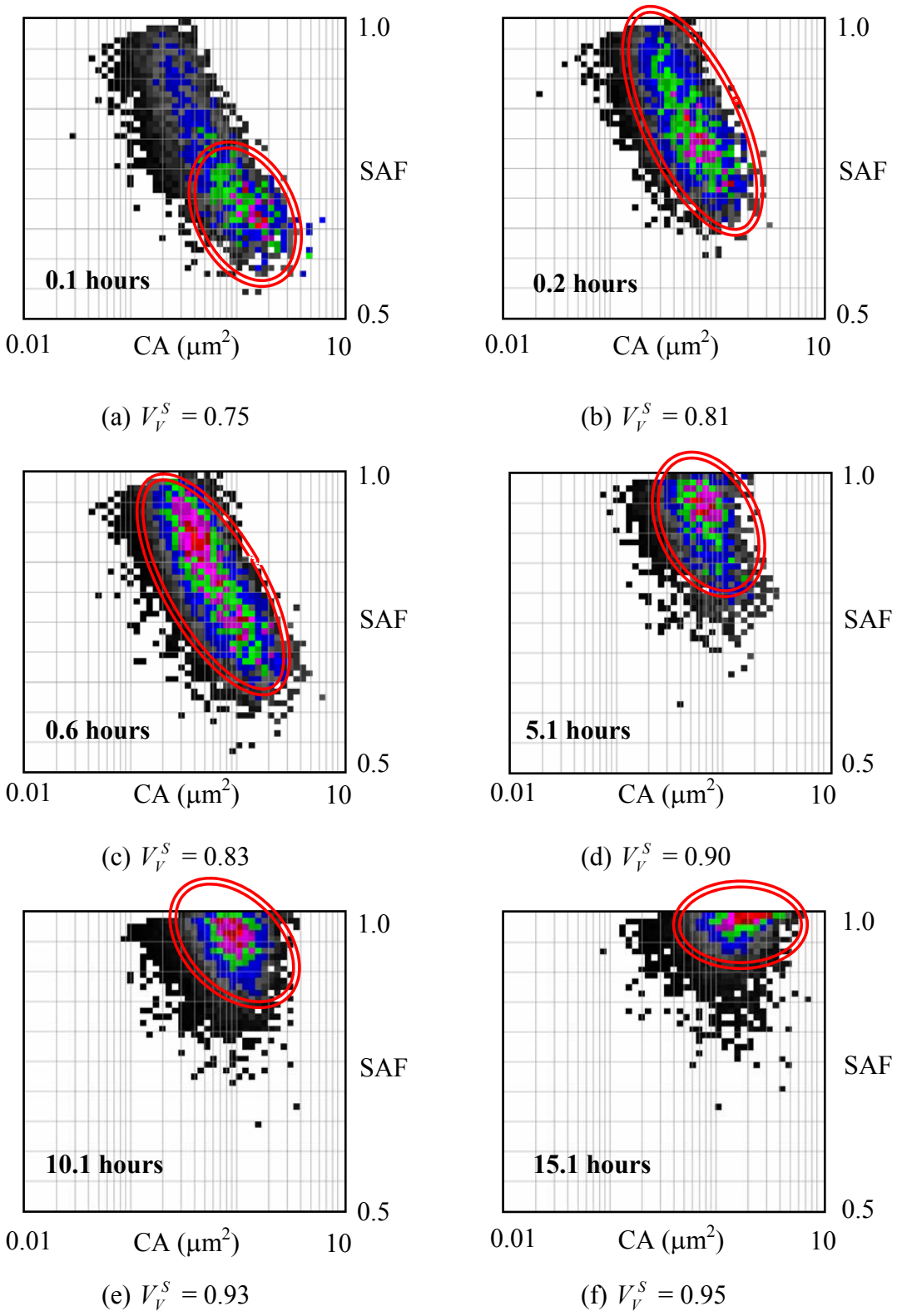

(a) $V_V^S = 0.75$ (b) $V_V^S = 0.81$

(c) $V_V^S = 0.83$ (d) $V_V^S = 0.90$

(e) $V_V^S = 0.93$ (f) $V_V^S = 0.95$

Figure 40. 2-D SAF vs. CA Maps for flocculated alumina samples.

(Courtesy of the MSE Dept., University of Pittsburgh, McAfee[35], p. 113)

By identifying the peaks for different solid volume fractions, the changes in the microstructure can be analyzed by examining the movement of the peaks as densification progresses. The movements of the peaks for the dispersed and flocculated alumina cases are shown in Figure 41. While the peak paths differ for these two cases, there are a few general observations which can be made concerning the evolution of the microstructure. First, the initial peak motion for $0.75 < V_V^S < 0.90$ is in the general direction of arrow (e) from Figure 31 (i.e. up and to the left on the 2-D SAF-CA Map). A comparison of the peak shift with the isopore lines shows a reduction in pore size by an order of magnitude for the peak (i.e. most of the tessellation cells). This behavior indicates pore shrinkage and breakup of the pore network in the microstructure – material behavior which commonly occurs during the intermediate stage of sintering. Second, at the higher densities ($V_V^S > 0.90$), the peak moves primarily in the general direction of arrow (b) from Figure 31 (i.e. to the right on 2-D SAF-CA Map). This indicates a general reduction in pore size with the elimination of the smaller pores. The removal of the smaller pores results in fewer tessellation cells, but the cells are larger in area with high SAF. This material behavior commonly occurs during the final stage sintering.

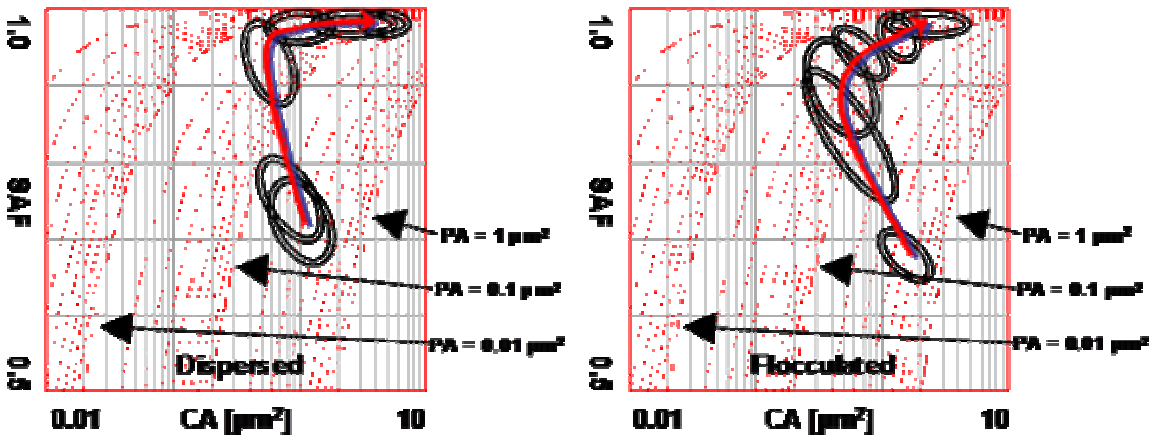

Figure 41. Peak paths for dispersed (left) and flocculated (right) alumina samples. (Courtesy of the MSE Dept., University of Pittsburgh, McAfee[35], p. 147)

5.0 SIMULATION RESULTS – ISOTROPIC, HOMOGENEOUS SINTERING

Simulations were run to examine the influence of several factors on the evolution of the microstructure: the particle size distribution, the number of particles within the RVE, the average initial overlap for the particles in the packing algorithm, and agglomerated packing arrangements. Densification in the simulation was modeled using isotropic, homogenous sintering as described in Section 3.5.1. In additional to the simulation of the initial packing arrangement, simulations were run for four different agglomerated particle arrangements which were created by varying the number of particles removed from the initially generated particle packing arrangement as described in Section 3.4.

5.1 PLOT OF $\overline{S}^{SS}$ vs. V_V^S CURVES – ISOTROPIC, HOMOGENEOUS SINTERING

For each simulated particle arrangement, the solid-solid surface area, S_V^{SS}, the solid-void surface area, S_V^{SV}, and the solid volume fraction, V_V^S were determined. The fractional solid-solid surface area $\overline{S}^{SS}$ was calculated and plotted as a function of the solid volume fraction V_V^S in Figure 42. The results for the experiments conducted on alumina samples from Section 4.1 are also plotted

for comparison. The different agglomerated particle arrangements are identified by the total number of spheres remaining in the overall containing box.

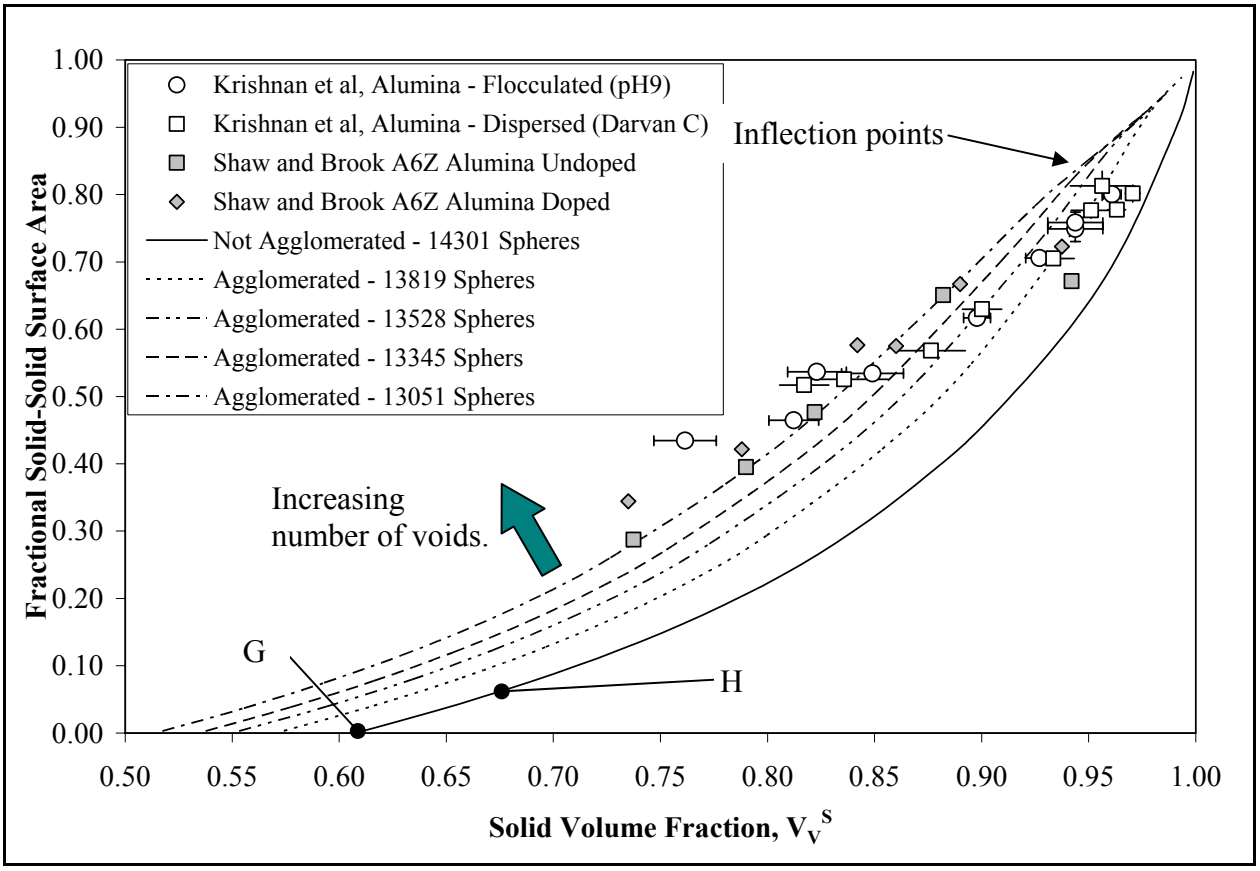

Figure 42. Comparison of $\overline{S}^{SS}$ vs. V_V^S for different number of voids.

5.1.1 Effect of particle distribution

Simulations were conducted for three different particle size distributions: a mono-sized distribution, a distribution duplicating the particle sizes in the alumina experiments reported by Nettleship, *et al* [29] with a ratio of the standard deviation to the mean for the particle sizes of

0.24, and a distribution of particle sizes with a standard deviation larger than the alumina experiment corresponding to a ratio of the standard deviation over the mean for the particle sizes of 0.32. The comparison showed that both the mono-sized particle distribution and the experimental particle size distribution had the same green density (V_V^S = 0.61). The wider particle distribution had a slightly greater green density (V_V^S = 0.62). Also, for all three distributions, the path of the fractional solid-solid surface area, $\overline{S}^{SS}$, versus the solid volume fraction, V_V^S, curves were similar to the "Not agglomerated" curve shown in Figure 42 from green density to full densification. Nolan and Kavanuagh [15] noted that certain values of the ratio of the minimum particle size over the maximum particle size influenced the efficiency of the particle packing. This could explain the similarity between the mono-sized and the experimental distributions, since the range of particle sizes for the experimental distribution may not be sufficiently large to permit the smaller particles to fill the gaps between the larger particles. The wider distribution had a greater range of particle sizes which allowed more of the smaller particles to fill some of the voids between the larger particles, hence the slightly greater green density. However, given the small change in the green density, varying the standard deviation of the particle sizes over the range considered did not significantly alter the evolution of $\overline{S}^{SS}$ with V_V^S.

5.1.2 Effect of number of spheres

Simulations were run to determine the effect of varying the number of spheres in the RVE. For simulations with less than ~100 spheres in the RVE, the path of the $\overline{S}^{SS}$ versus V_V^S curve changed as the number of spheres was varied. For simulations with more than 100 spheres, the

addition of more spheres to the simulation RVE did not alter the path of the $\overline{S}^{SS}$ versus V_V^S curve. Consequently, a minimum of 100 spheres are needed to model the evolution of the parameters used to characterize the microstructure. However, since the agglomerations are simulated by eliminating randomly selected particles, additional particles are needed inside the RVE to provide sufficient regions of voids interspaced among the solid particles. Hence, a larger number of spheres were required in the simulation to create agglomerated packing arrangements (10,000+ spheres).

5.1.3 Effect of varying amount of permitted overlap

Two simulations were run to determine the influence of varying the amount of initial overlap between particles produced by the packing algorithm prior to densification. The first simulation had a packing arrangement with an average overlap of 0.5%. The second simulation had a packing arrangement with an average overlap of 5.7%. The increase in the amount of permissible overlap not only increased the initial solid volume fraction (from 0.61 to 0.66), but also increased the initial fractional solid-solid surface area (from approximately 0 to 0.05). The combination of these two events did not alter the path of the $\overline{S}^{SS}$ versus V_V^S curve. Instead, the starting point of the simulation shifted along the $\overline{S}^{SS}$ versus V_V^S curve from point G to point H as shown in Figure 42. Hence, increasing the average overlap essentially starts the simulation at a point further in the densification process, but does not affect the subsequent evolution of $\overline{S}^{SS}$ in the model.

5.1.4 Effect of agglomerations in the particle arrangement

Simulations were run with different numbers of additional voids randomly spaced in the particle packing arrangement to model the agglomeration of particles which may be present in the packing arrangements of real materials. The fractional solid-solid surface area $\overline{S}^{SS}$ as a function of the solid volume fraction V_V^S is plotted in Figure 42 for different agglomerated particle arrangements. A comparison of the results shows that the additional voids introduced to the particle packing to simulate the agglomerations reduces the solid volume fraction for the green compact. This shifts the $\overline{S}^{SS}$ versus V_V^S curve for the agglomerated particle arrangements to a trajectory different from the particle arrangement without agglomerations. Also, an inflection point (see upper right of curves in Figure 42) appears as the simulation approaches full densification for the agglomerated curves. The inflection behavior may be due to the smaller voids being eliminated first, with the larger voids associated with the removed spheres filling or breaking up later in the sintering process. If so, this would alter the rate of change of the surface areas versus the solid volume fraction thus creating the inflection in the curve. The curves for the agglomerated arrangements all have the same trajectory as they approach full densification.

5.1.5 Comparison to experiments

Shaw and Brook [42] conducted high temperature experiments (1500°C) on other alumina samples. As shown in Figure 42, their experimental results follow a simulated agglomerated particle arrangement $\overline{S}^{SS}$ versus V_V^S curve closely for the density range $0.60 < V_V^S < 0.88$.

However, at higher densities (V_V^S>0.88), the experimental results diverge from the simulation curve by cutting across several different simulation curves. This divergence may also occur due to grain growth at the higher densities but that resulted in coarsening (not self-similar coarsening) of the microstructure in the alumina samples at the higher densities.

Since the particle size distribution used in the simulation duplicates the particle size distribution measured from the experimental samples [17, 29] and the simulation makes the common assumption of uniform contact flattening, one might expect that the simulated $\overline{S}^{SS}$ versus V_V^S curves would match those for the experimental data from the alumina samples reported by Krishnan, *et al.*[17] and those of Brook and Shaw.[42] Suitable experimental results are rare because the determination of $\overline{S}^{SS}$ requires the measurement of S_V^{SS} and S_V^{SV} on the same samples. $\overline{S}^{SS}$ cannot be calculated directly from a measurement of S_V^{SV} by gas absorption methods. However, as shown in Figure 42, the experimental data trends for sintering at 1350 °C from Krishnan, *et al.* have flatter trajectories which cross the $\overline{S}^{SS}$ versus V_V^S curves for the simulations with agglomerated particle arrangements. At the lower sintering temperature, one might speculate that there is a greater contribution of pore coarsening by surface diffusion which lower S_V^{SV} and increase $\overline{S}^{SS}$ at any particular density. This would also decrease the slope of the curve. These effects cannot be accommodated in the present simulation.

5.2 RVE CROSS SECTIONS – ISOTROPIC, HOMOGENEOUS SINTERING

Sample cross sections taken from the same plane (mid-height of the RVE) are presented for the simulations without any agglomerations (see Figure 43) and with agglomerations (see Figure 44) in the particle arrangement for comparable solid volume fractions. A comparison of these cross sections can be used to illustrate several features of the simulated microstructural evolution. For comparable solid volume fractions, the size of the voids and their frequency differ for the various particle arrangements. For the simulation with no agglomerations, an examination of the cross section in Figure 43(d) shows a fairly uniform distribution of the voids. This implies spatial homogeneity in the microstructure. However, for the simulation with agglomerations, an examination of the cross section in Figure 44(d) indicates the presence of local regions of high and low density which will vary based on the number of agglomerations present in the RVE. These differences in the microstructure may provide an explanation for the presence of the inflection point in the $\overline{S}^{SS}$ versus V_V^S curves for the simulations with agglomerations. For the same solid volume fraction, the agglomeration simulation has fewer voids, but the voids are larger in size as compared to the simulation with no agglomerations. This is because more necking is required in the areas between the large voids to get the same density, thereby eliminating many of the small pore sections that are still present in the simulation without large voids.

The cross sections taken from the RVE also demonstrate the breakup of long, thin voids as a natural consequence of densification by contact flattening. This is illustrated by examining the region labeled K in Figure 44 for different solid volume fractions. Region K begins as one large void as shown in Figure 44(a). It initially reduces in size in the early stages of sintering as shown in Figure 44(b). As sintering progresses even further, the breakup of the void begins to take place as segments of the void are pinched off as shown in Figure 44(c). Finally, densification proceeds to a point where the initially large void is broken into several separate, smaller voids as shown in Figure 44(d).

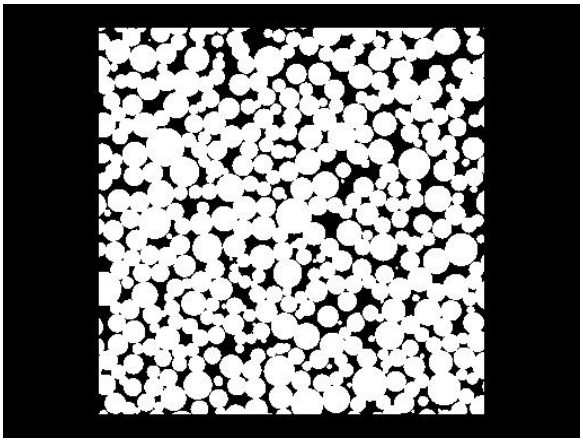

(a) $V_V^S = 0.75$

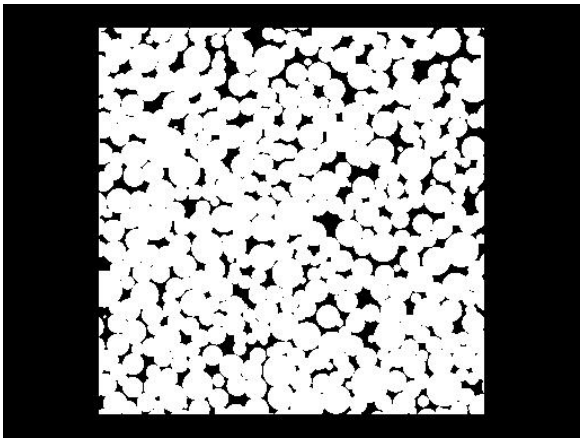

(b) $V_V^S = 0.85$

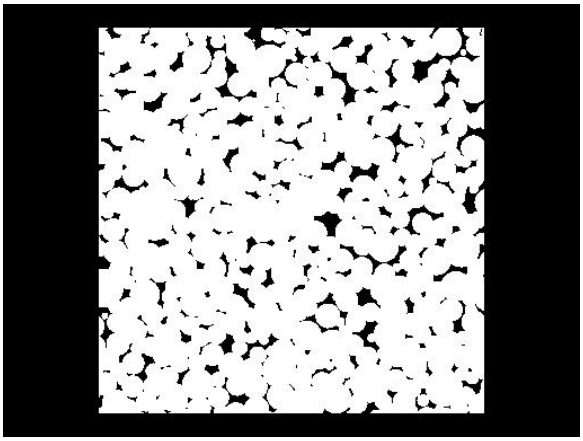

(c) $V_V^S = 0.90$

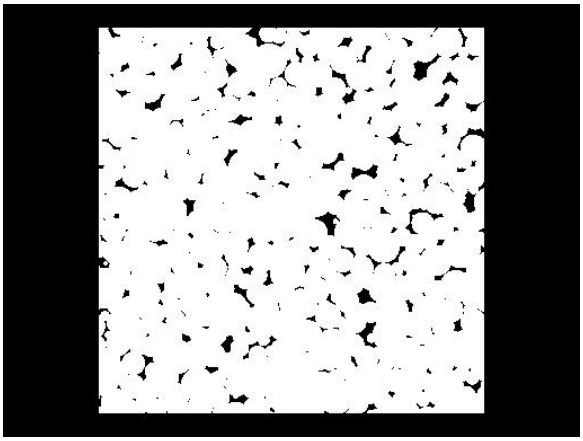

(d) $V_V^S = 0.95$

Figure 43. Sample cross sections from RVE for simulation without agglomerations (14301 spheres).

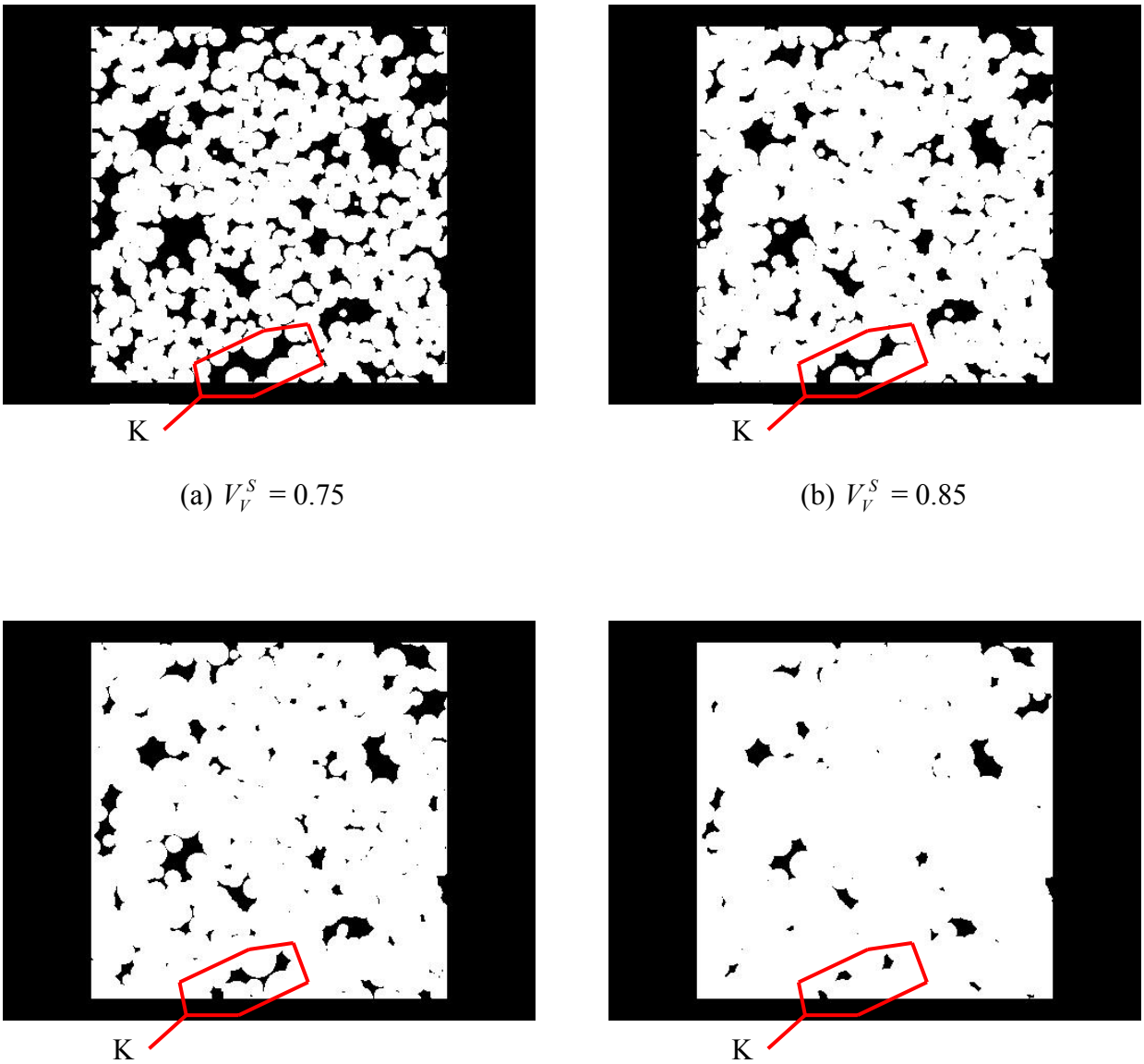

(a) $V_V^S = 0.75$ (b) $V_V^S = 0.85$

(c) $V_V^S = 0.90$ (d) $V_V^S = 0.95$

Figure 44. Sample cross sections from RVE for simulation with agglomerations (13051 spheres).

5.3 TESSELLATION RESULTS – ISOTROPIC, HOMOGENEOUS SINTERING

Tessellation was applied to multiple cross sections taken from the RVE for the different simulations. The tessellated images in Figures 45 and 46 correspond to the sample cross sections presented in Figures 43 and 44 respectively. From the tessellated images, the cell properties (SAF and CA) are determined for different solid volume fractions. Figure 47 shows the 3-D SAF vs. CA Maps and Figure 48 shows the 2-D SAF vs. CA Maps for the simulation without agglomerations. Figure 49 shows the 3-D SAF vs. CA Maps and Figure 50 shows the 2-D SAF vs. CA Maps for the simulation with agglomerations (13501 spheres). The peaks of the distribution are highlighted on the 2-D SAF vs. CA Maps in Figures 48 and 50. The peak for the different solid volume fractions are superimposed on a 2-D SAF vs. CA Map (see Figure 51) for each simulation in order to trace the movement of the peak as densification progresses.

In the experiments, the dispersed sample had a more even distribution of the material while the flocculated sample had a greater degree of agglomeration present. The first important observation from the comparison of the simulation and experimental results is that the same general behavior pattern is observed in both the simulations and the experiments. The first motion of the peak is up and to the left. This peak motion indicates an order of magnitude decrease in pore size and the breakup of the pores characteristic of the intermediate stage of sintering ($V_V^S \sim 0.75$ to $V_V^S \sim 0.85$). As mentioned in the previous section, the breakup of the pore network in the simulation can be shown using the cross sections taken from the RVE – see region K in Figure 44. At higher densities ($V_V^S > 0.90$), the peak motion shifts to the right. This

indicates a general shrinkage of the pores characteristic of the final stage of sintering. The smaller pores are eliminated first which would result in larger tessellated cells.

Another observable trait is the initial distribution of solid area fraction (SAF) values for the tessellated cells. If the 3-D SAF vs. CA maps are examined, there is a higher frequency of cells with low SAF for the simulation without agglomerations, see Figure 48(a), and the flocculated experiment results, see Figure 40(a), than for the simulation without agglomerations, see Figure 50(a), and the dispersed experiment results, Figure 38(a).

For the simulation without agglomerations and the flocculated experiment results, the interconnected pore network has larger pore spaces in the agglomerated and flocculated cases resulting in tessellation cells with lower SAF values. As densification progresses, there is a decrease in the number of cells with low SAF as the interconnected pore network breaks down. As the material approaches full densification during the final stage of sintering, break down of the pore network is complete as isolated pores form. Thus, thought the initial distribution differs, the tessellation cells begin to shift to similar behavior when the pores get smaller as densification occurs.

(a) $V_V^S = 0.75$

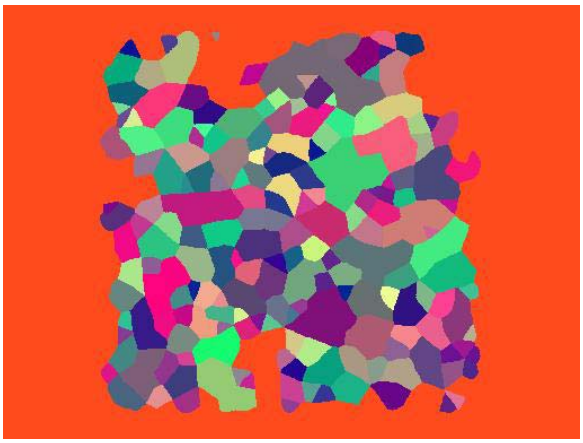

(b) $V_V^S = 0.85$

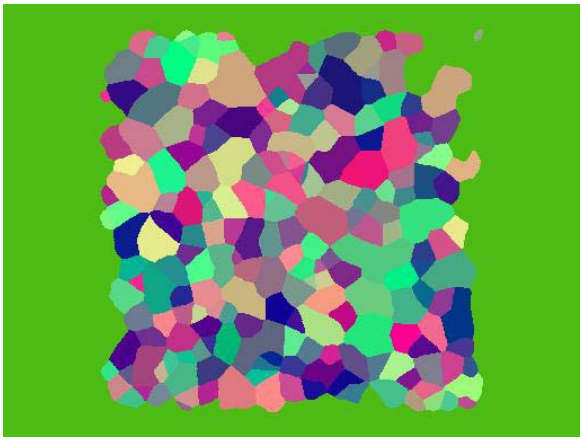

(c) $V_V^S = 0.90$

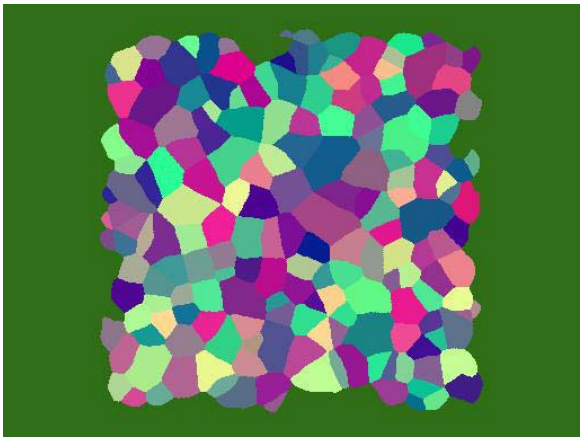

(d) $V_V^S = 0.95$

Figure 45. Tessellated images for cross sections from Figure 43 for simulation without agglomerations.

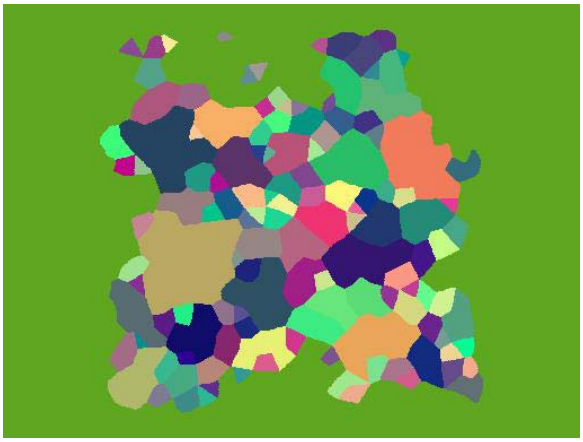

(a) $V_V^S = 0.75$

(b) $V_V^S = 0.85$

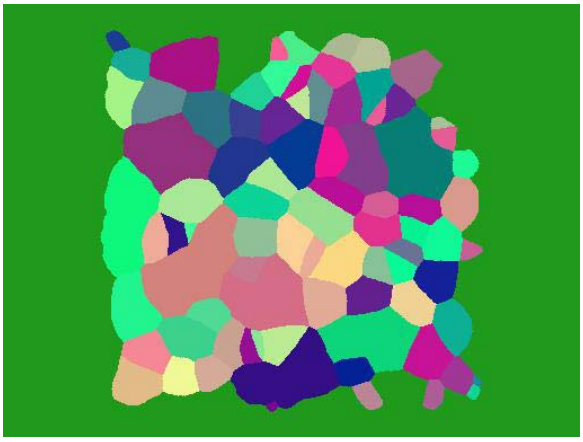

(c) $V_V^S = 0.90$

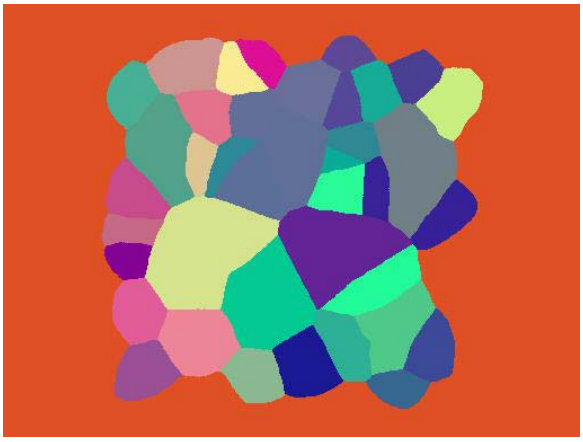

(d) $V_V^S = 0.95$

Figure 46. Tessellated images of cross sections from Figure 44 for simulation with agglomerations.

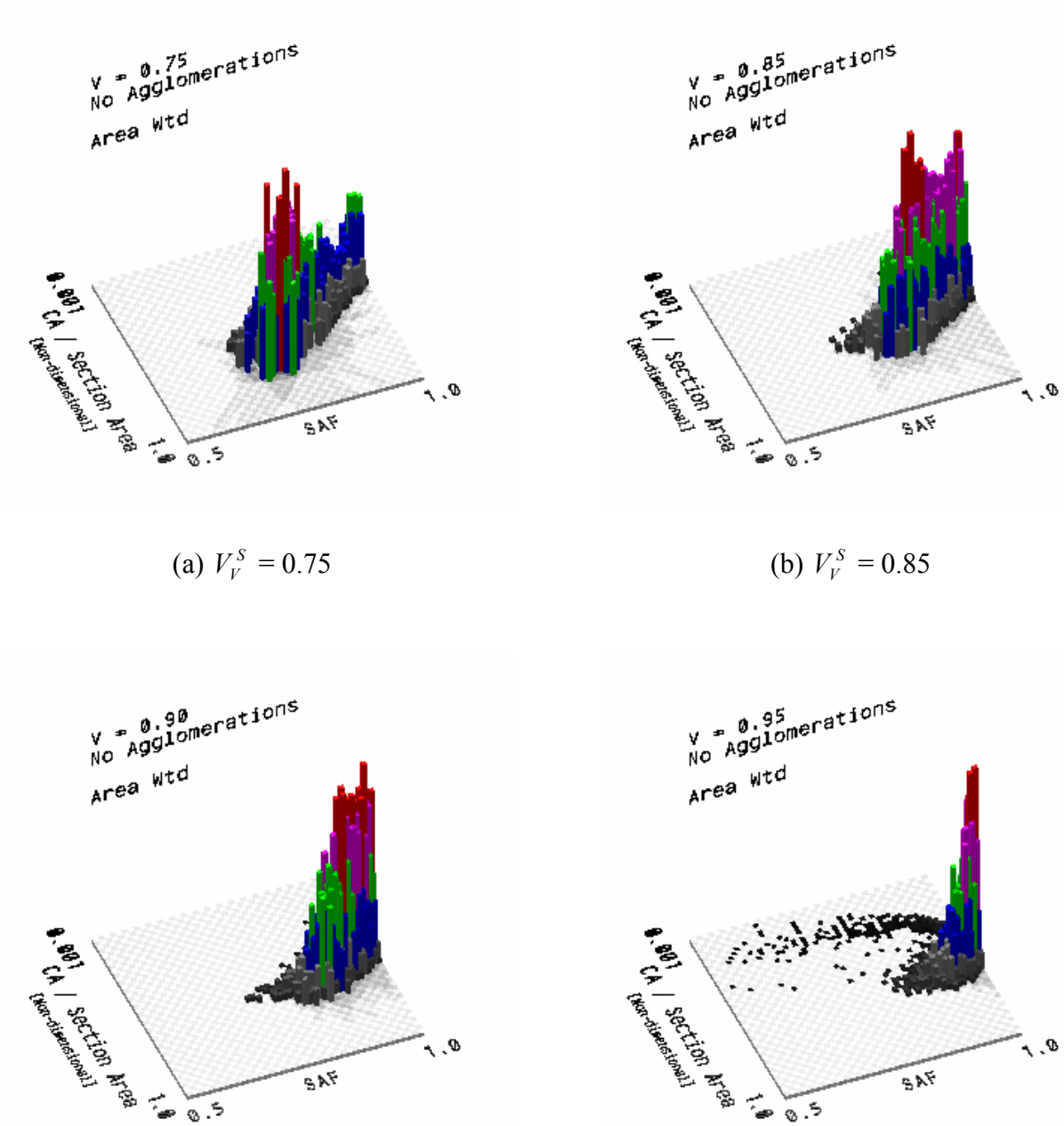

(a) $V_V^S = 0.75$

(b) $V_V^S = 0.85$

(c) $V_V^S = 0.90$

(d) $V_V^S = 0.95$

Figure 47. 3-D SAF vs. CA / Section Area Maps for simulation without agglomeration.

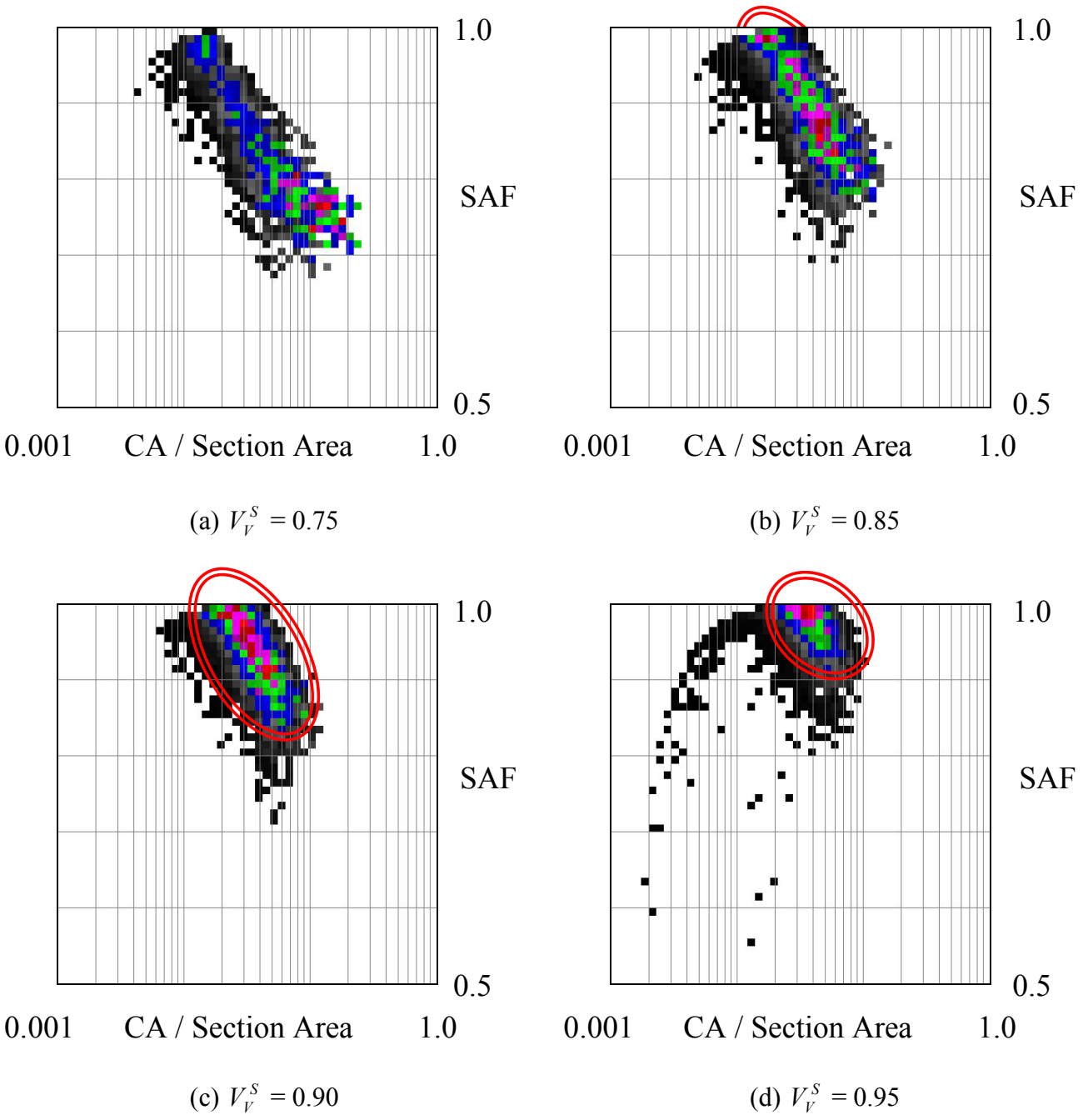

Figure 48. 2-D SAF vs. CA / Section Area Maps for simulation with no agglomerations.

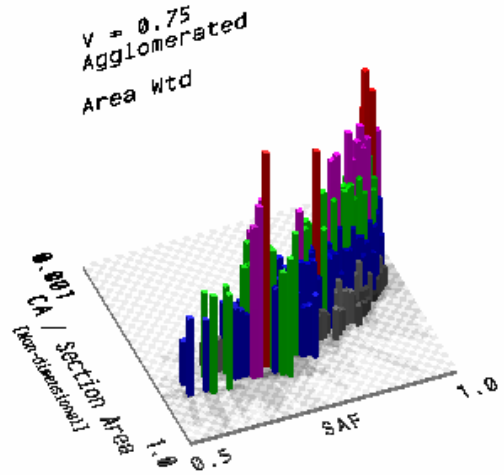

(a) $V_V^S = 0.75$

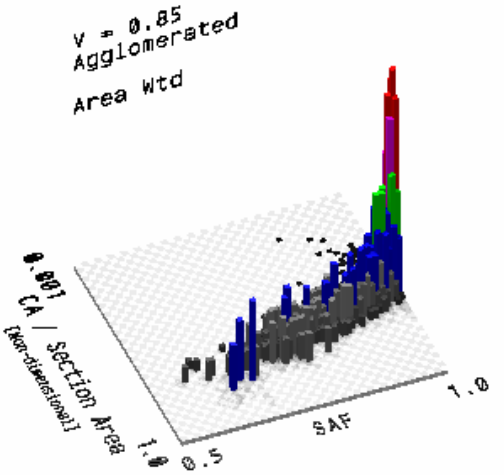

(b) $V_V^S = 0.85$

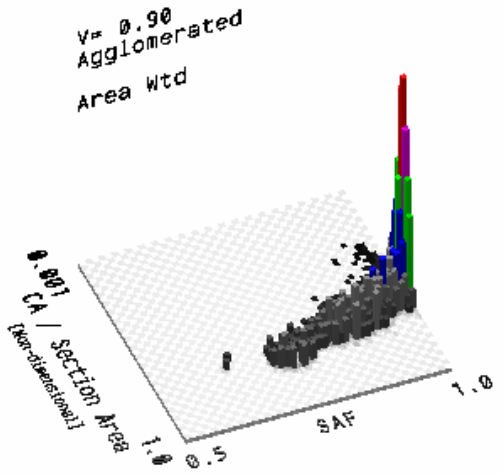

(c) $V_V^S = 0.90$

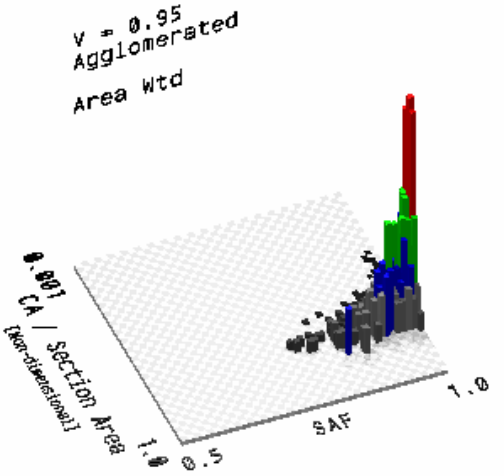

(d) $V_V^S = 0.95$

Figure 49. 3-D SAF vs. CA Maps for simulation with agglomerations.

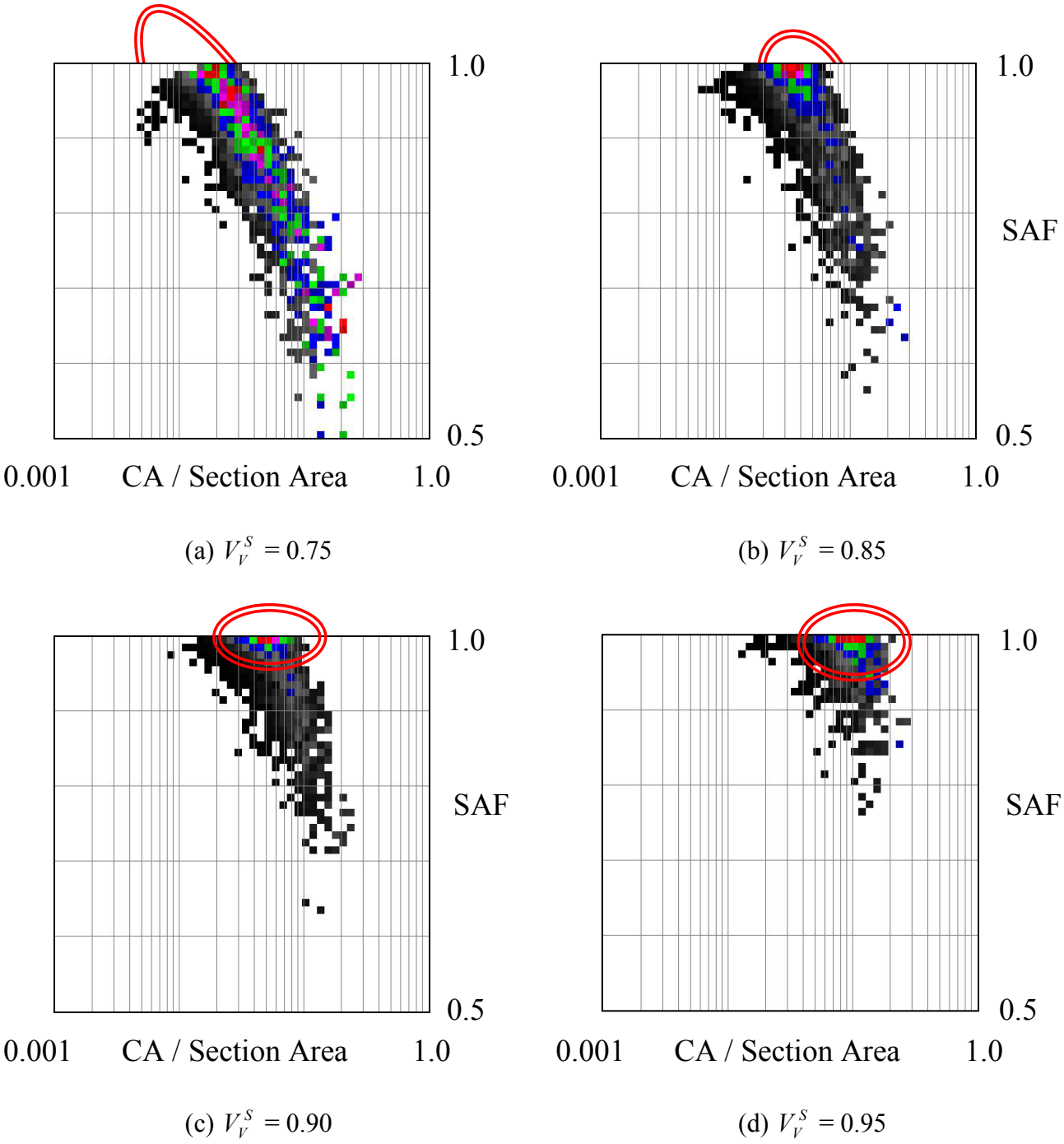

(a) $V_V^S = 0.75$ (b) $V_V^S = 0.85$

(c) $V_V^S = 0.90$ (d) $V_V^S = 0.95$

Figure 50. 2-D SAF vs. CA Maps for simulation with agglomerations (13051 spheres in RVE).

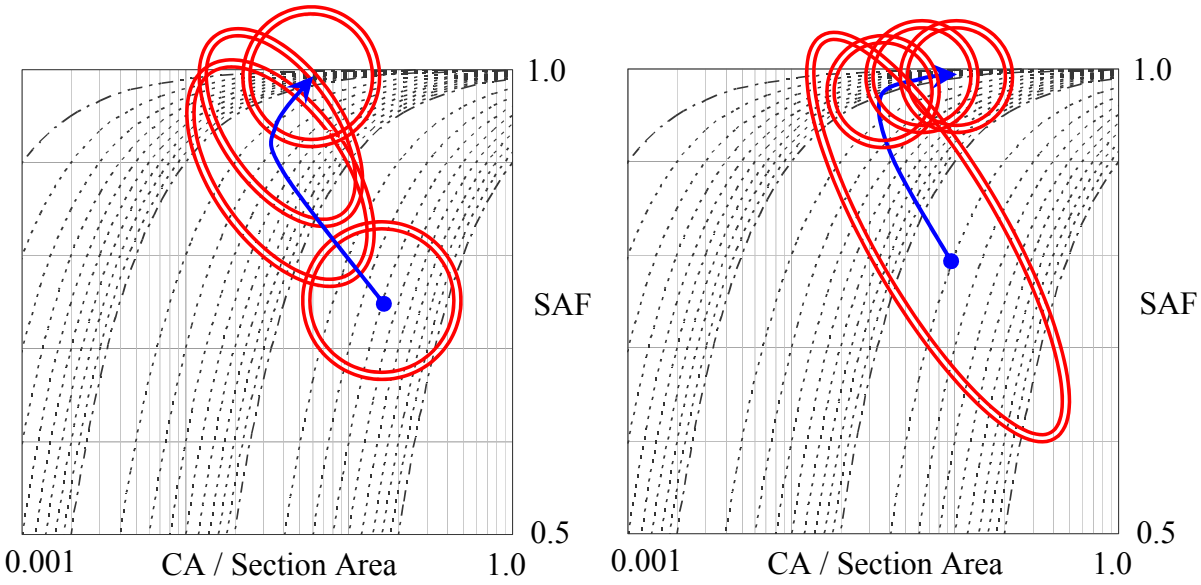

(a) Simulation without agglomerations. **(b) Simulation with agglomerations (13051 spheres).**

Figure 51. 2-D SAF vs. CA Maps indicating movement of the peaks for the simulations.

6.0 SIMULATION RESULTS – LOCAL PARTICLE REARRANGEMENT (LPR)

A series of simulations were run to determine the effect of using Local Particle Rearrangement (LPR), as described in Section 3.5.2, to simulate sintering. Two sets of three simulations were run. The first set of simulations applied three different sintering models to a particle arrangement with no agglomeration. The second set of simulations applied three different sintering models to a particle arrangement with agglomeration. For each set, the three sintering models applied to the particle arrangement were: isotropic, homogenous sintering; sintering through Local Particle Rearrangement (LPR) using the values of μ^t=0.01 and μ^n=0.1 for the viscosities; and sintering through Local Particle Rearrangement (LPR) using the values of μ^t=0.1 and μ^n=0.1 for the viscosities. The viscosity values for the two cases of sintering using LPR were arbitrarily chosen to explore the effect of the tangential viscosity since it models the ability of the particles to slide past each other in the simulation.

The maximum number of particles in the particle arrangement placed in the containing box was limited to 806 spheres. This corresponds to approximately 466 spheres residing inside the RVE for the green compact. This restriction is due to the maximum allowable size of the software application. This limits the amount of memory which can be allocated for the simulation. Coupled with the additional memory space required to store the variables and the matrix used solve the equations to establish force and moment equilibrium for the simulated

sintering using Local Particle Rearrangement (LPR), this significantly reduces the number of particles which can be placed in the simulation.

6.1 PLOT OF $\overline{S}^{SS}$ VS. V_V^S CURVES – LPR

The results for the first and second sets of simulations are plotted in Figure 52 along with the experimental data from Section 4.0. Using this plot, a few general observations can be made from a comparison of the $\overline{S}^{SS}$ vs. V_V^S curves for the two sets of simulations.

For the first set of simulations examining the particle arrangement with no agglomerations, the $\overline{S}^{SS}$ vs. V_V^S curves for the simulation using isotropic, homogeneous sintering and the two simulations using LPR essentially follow the same path. This behavior can be explained by the arrangement of the particles in the green (initial) compact. Without the presence of the larger voids used to simulate agglomerations in the particle arrangement, the motion of the particles in the LPR simulations is restricted due to the close packing of the particles. Consequently, densification essentially occurs only through contact flattening as modeled by the isotropic, homogeneous sintering for all three simulations - hence the similarity among the $\overline{S}^{SS}$ vs. V_V^S curves.

For the second set of simulations examining the particle arrangement with agglomeration, the two sintering simulations using LPR essentially have the same the $\overline{S}^{SS}$ vs. V_V^S curves.

However, these $\overline{S}^{SS}$ vs. V_V^S curves follow a path which has lower values of $\overline{S}^{SS}$ than the $\overline{S}^{SS}$ vs. V_V^S curve for the simulation with isotropic, homogeneous sintering. For isotropic, homogenous sintering, the densification of the particle arrangement occurs through contact flattening. For this sintering model, an increase in density generally corresponds to an increase in the solid-solid surface area (S^{SS}) which results in an increase in $\overline{S}^{SS}$. However, for sintering via local particle rearrangement, densification can occur, not only by contact flattening, but also by individual particles moving to fill the empty voids spaces in the agglomerated arrangement. When the later occurs, there is an increase in the density, but there may not be a corresponding increase in solid-solid surface area. The result is a different path for the $\overline{S}^{SS}$ vs. V_V^S curves of the simulations using LPR. Since simulations have the same initial particle arrangement and will eventually approach full density, all three curves start at the same position and will eventually converge at higher densities.

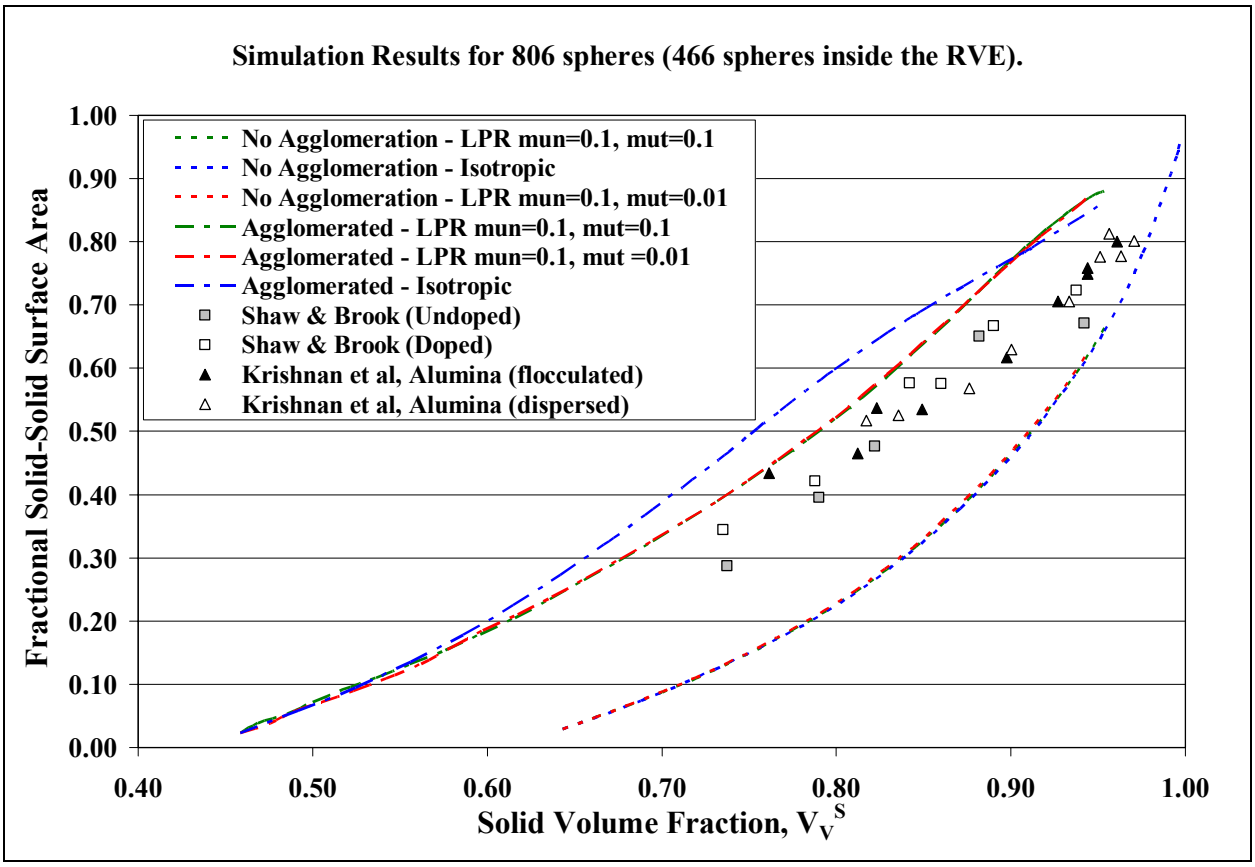

Figure 52. Comparison of $\overline{S}^{SS}$ vs. V_V^S curves for the simulations examining the effect of LPR.

6.2 RVE CROSS SECTIONS – LPR

Sample cross sections taken from the same plane (mid-height of the RVE) are presented for each simulation at different solid volume fractions, V_V^S. For the first set of simulations, the cross sections for the simulations with no agglomeration in the particle arrangement are shown in Figure 53 for the case of isotropic, homogeneous sintering, in Figure 54 for the case of sintering using LPR with μ^t=0.01 and μ^n=0.1, and in Figure 55 for the case of sintering using LPR with

μ^t=0.1 and μ^n=0.1 for comparable solid volume fractions. A comparison of the cross sections at $V_V^S \cong 0.95$ indicates a different evolution of the microstructure for each simulation. For the simulation using isotropic, homogeneous sintering shown in Figure 53(d), there are relatively fewer small pores when compared to the sections of the two simulations using LPR in Figure 54(d) and Figure 55(d). This indicates that using sintering via LPR may create a greater range of pores sizes in the simulation. Furthermore, the simulation using LPR with the higher value for the tangential viscosity [see Figure 55(d)] has a greater number of small pores than the other LPR simulation [see Figure 54(d)]. This suggests that the ability of the particles to slide by each other, modeled in the simulation by the tangential viscosity, may influence the rate at which the small pores are eliminated in the LPR simulations.

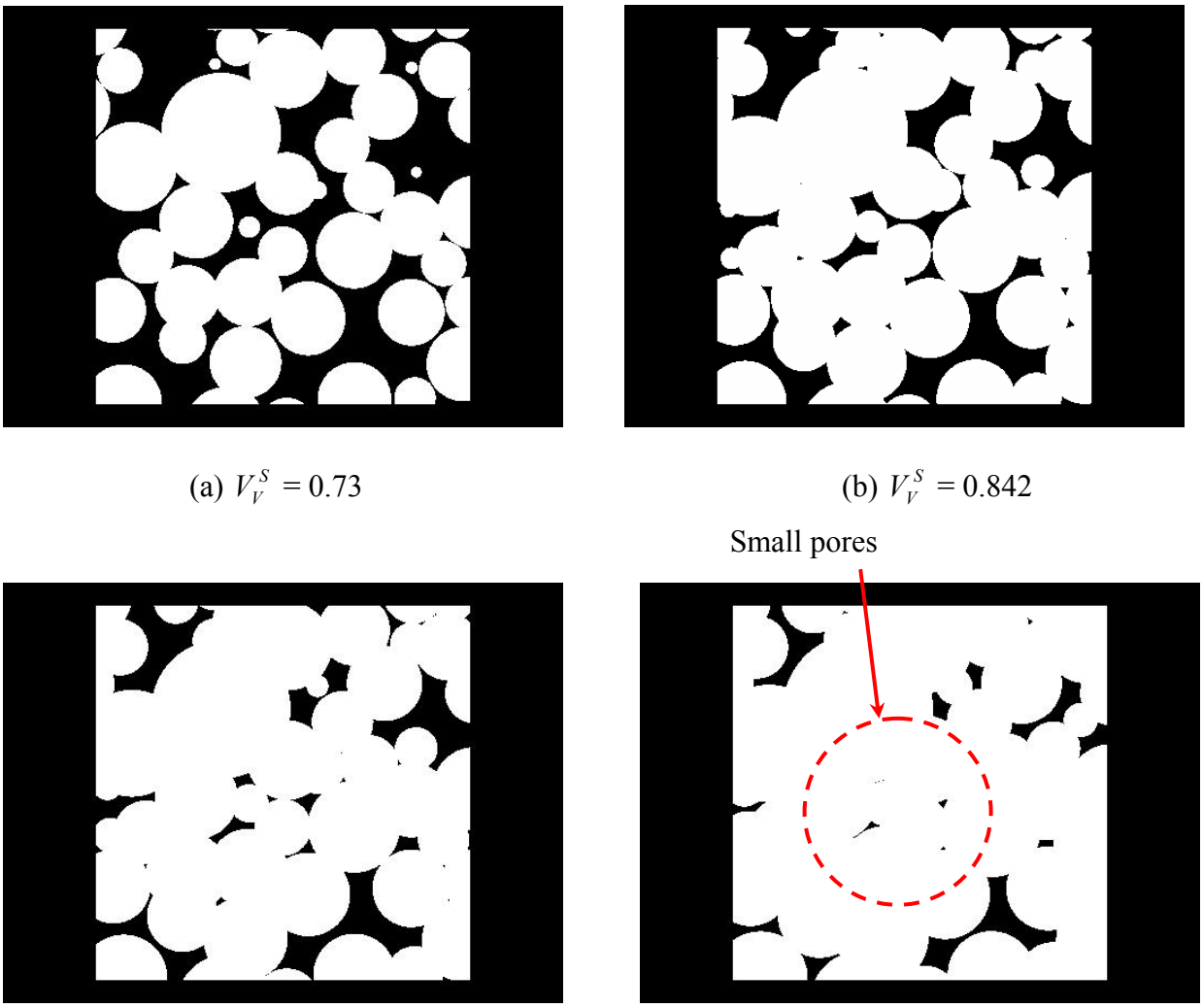

(a) $V_V^S = 0.73$

(b) $V_V^S = 0.842$

(c) $V_V^S = 0.897$

(d) $V_V^S = 0.954$

Figure 53. Cross sections for isotropic, homogeneous sintering; no agglomerations.

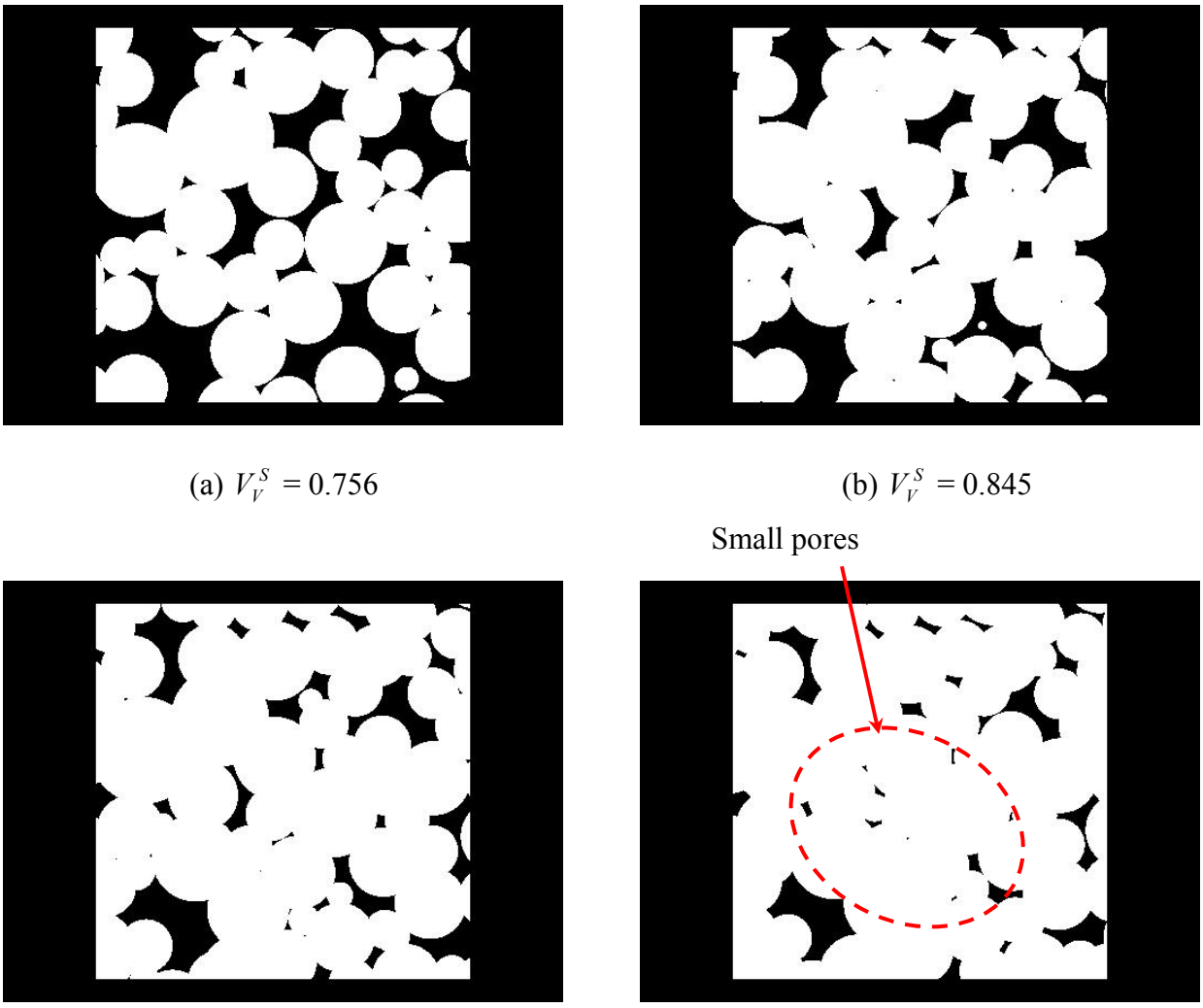

(a) $V_V^S = 0.756$

(b) $V_V^S = 0.845$

(c) $V_V^S = 0.902$

(d) $V_V^S = 0.945$

Figure 54. Cross sections for sintering via LPR (μ^t=0.01, μ^n=0.1); no agglomerations.

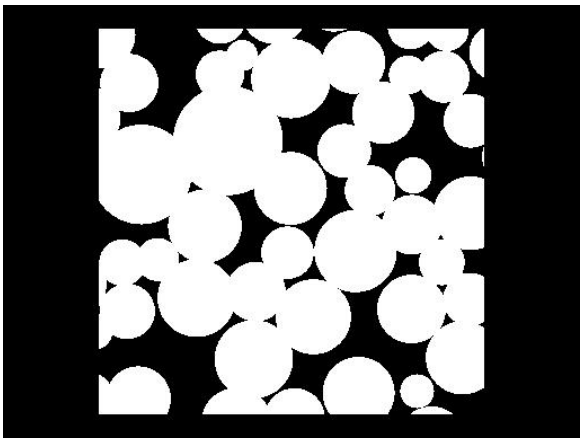

(a) $V_V^S = 0.76$

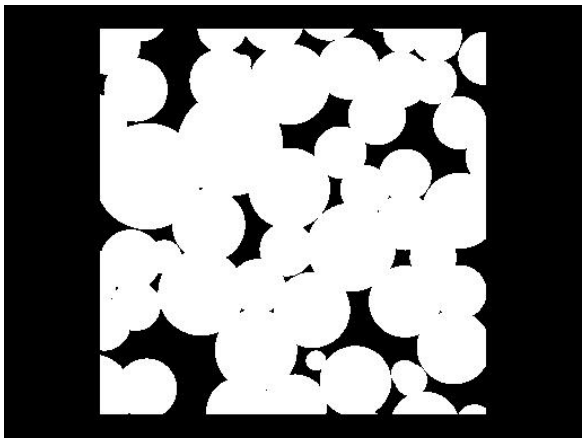

(b) $V_V^S = 0.846$

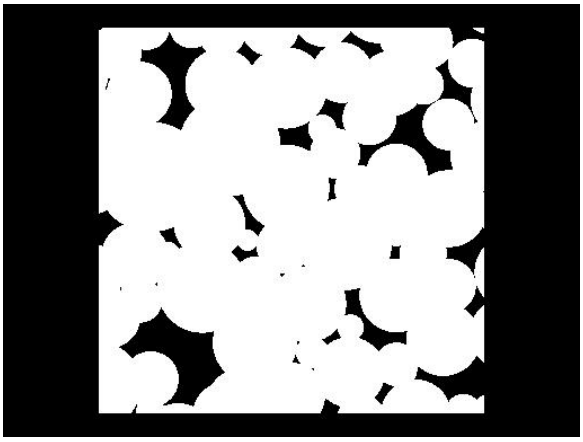

(c) $V_V^S = 0.90$

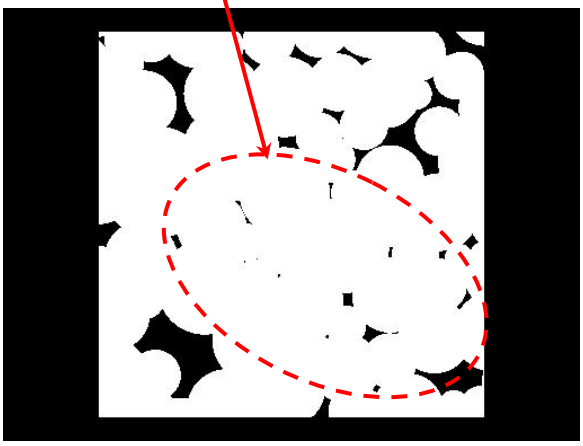

(d) $V_V^S = 0.947$

Figure 55. Cross sections for sintering via LPR (μ^t=0.1, μ^n=0.1); no agglomeration.

For the second set of simulations, the cross sections for the simulations with agglomeration in the particle arrangement are shown in Figure 56 for the case of isotropic, homogeneous sintering, in Figure 57 for the case of sintering using LPR with μ^t=0.01 and μ^n=0.1, and in Figure 58 for the case of sintering using LPR with μ^t=0.1 and μ^n=0.1 for comparable solid volume fractions. For comparable solid volume fractions, the particle arrangements with agglomeration have, in general, fewer small pores than the particle arrangement with no agglomerations. The reason for this is the same as noted one noted in Section 5.2 (i.e. that more necking is required in the areas between the large voids to get the same density, thereby eliminating many of the small pores which are typically present in the simulation with no agglomeration).

Unfortunately, an examination of the cross sections indicates a problem with the number of particles in the simulation. At high densities, there are very few pores remaining in the simulation as shown in Figure 56(d) [only two pores], Figure 57(d) [only four pores] and Figure 58(d) [only three pores]. Some of the pores are open to the edge as seen in Figure 56(d). This reduces the number of tessellation cells and affects the data. Consequently, a larger number of particles are required inside the RVE before a proper analysis of the effect of sintering using LPR on agglomerated particle arrangements can be made.

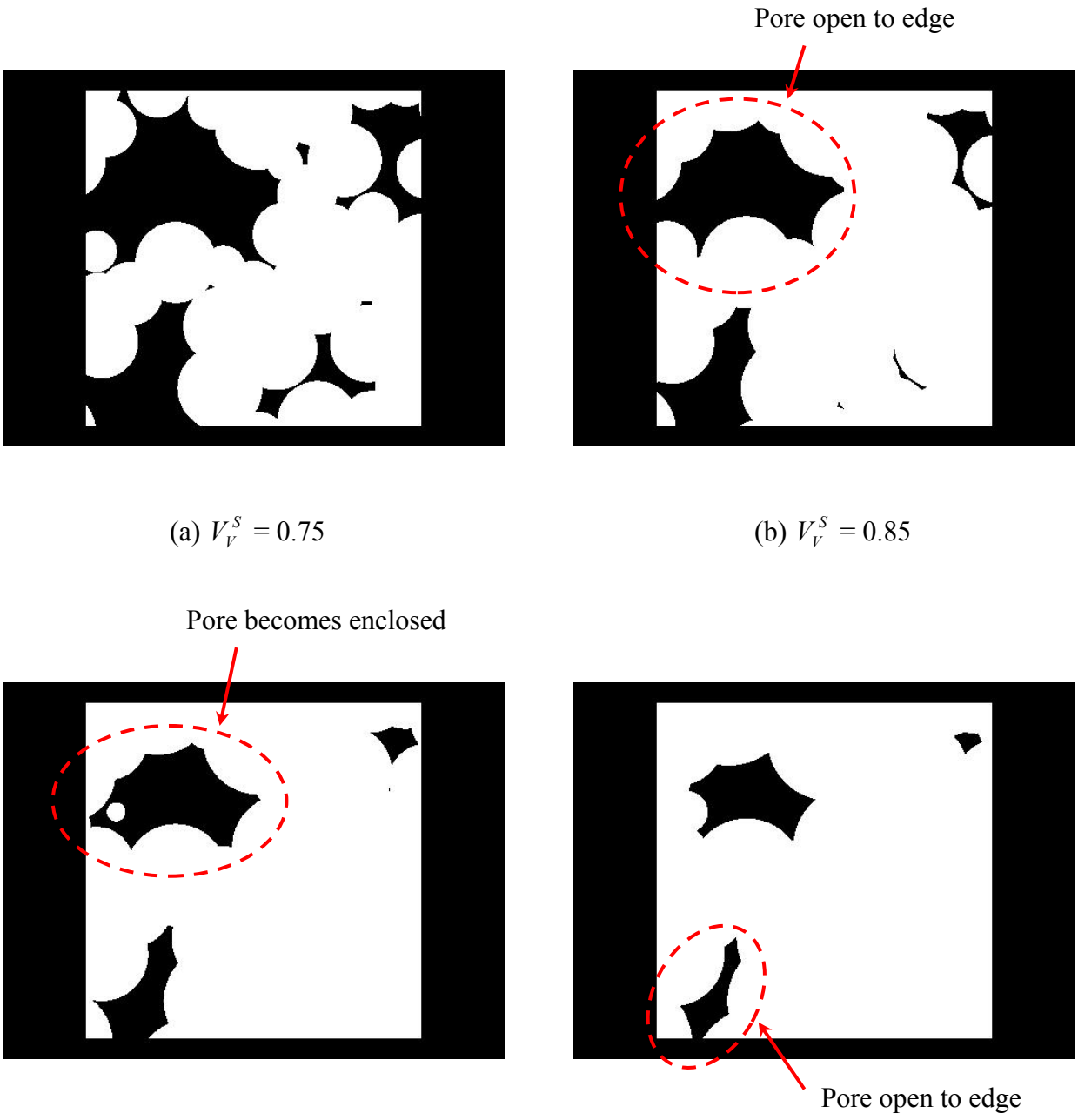

Figure 56. Cross sections for isotropic, homogeneous sintering; agglomeration.

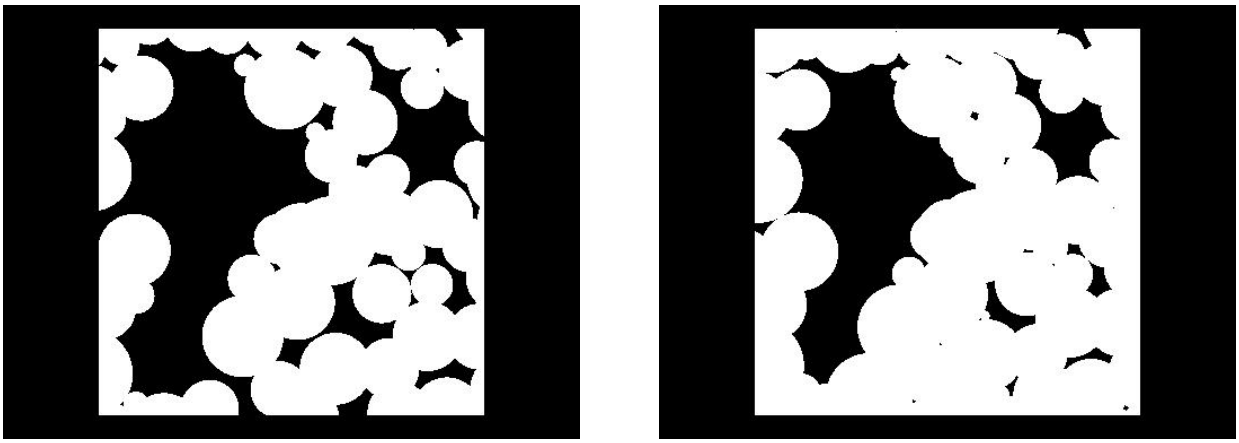

(a) $V_V^S = 0.75$ (b) $V_V^S = 0.844$

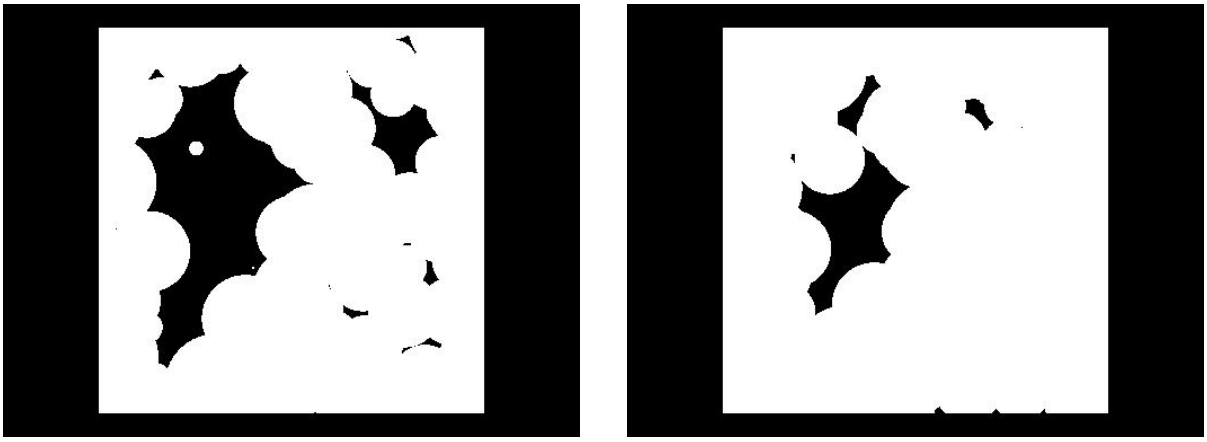

(c) $V_V^S = 0.90$ (d) $V_V^S = 0.951$

Figure 57. Cross sections for sintering via LPR (μ^t=0.01, μ^n=0.1); agglomerations.

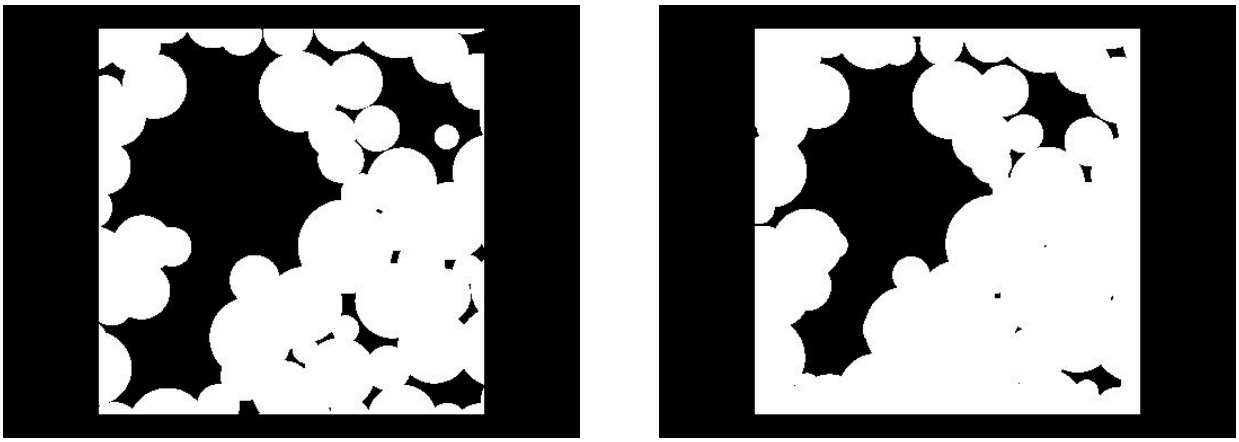

(a) $V_V^S = 0.75$ (b) $V_V^S = 0.844$

(c) $V_V^S = 0.90$ (d) $V_V^S = 0.951$

Figure 58. Cross sections for sintering via LPR (μ^t=0.1, μ^n=0.1); agglomeration.

6.3 TESSELLATION RESULTS – LPR

Tessellation was applied to multiple cross sections taken from the RVE for the different simulations. The 2-D SAF vs. CA Maps for the first set of simulations of the particle arrangement with no agglomerations are shown in Figure 59 for the case of isotropic, homogenous sintering, in Figure 60 for the case of sintering using LPR with μ^t=0.01 and μ^n=0.1 , and Figure 61 for sintering using LPR with μ^t=0.01 and μ^n=0.1 with the peaks are highlighted. The peaks for the different solid volume fractions are superimposed on the 2-D SAF vs. CA Maps in Figure 62 for each simulation in order to trace the movement of the peak as densification progresses.

If the peaks are compared for V_V^S = 0.75, the distribution of the tessellation cell properties is wider for the two simulations using LPR [see Figure 62(b) and Figure 62(c)] than for the simulation using isotropic, homogeneous sintering [see Figure 62(a)]. The peaks for the LPR simulations extend across several isopore lines and indicate a variation in pore size of two orders of magnitude. Note that since the simulation is non-dimensional, the pore area (PA) is normalized on the 2-D SAF vs. CA Maps by dividing by the section area (SA). This provides quantitative support for the observation made from the examination of the cross sections that the simulations using LPR have more small pores, in general, than the simulation for isotropic, homogenous sintering.

An examination of the peak paths shows movement of the peaks upward on the 2-D SAF vs. CA Maps with a slight movement to the left as densification occurs. The upward motion of the peak indicates a general decrease in pore size. The movement to the left indicates the

presence of some pore breakup. At higher solid volume fractions (i.e. $0.90 < V_V^S < 0.95$), the peak paths show a slight shift to the right indicating the elimination of the smaller pores. While they are not the same, the general behavior of the peak paths is similar to the pattern observed in the experimental data for microstructural evolution.

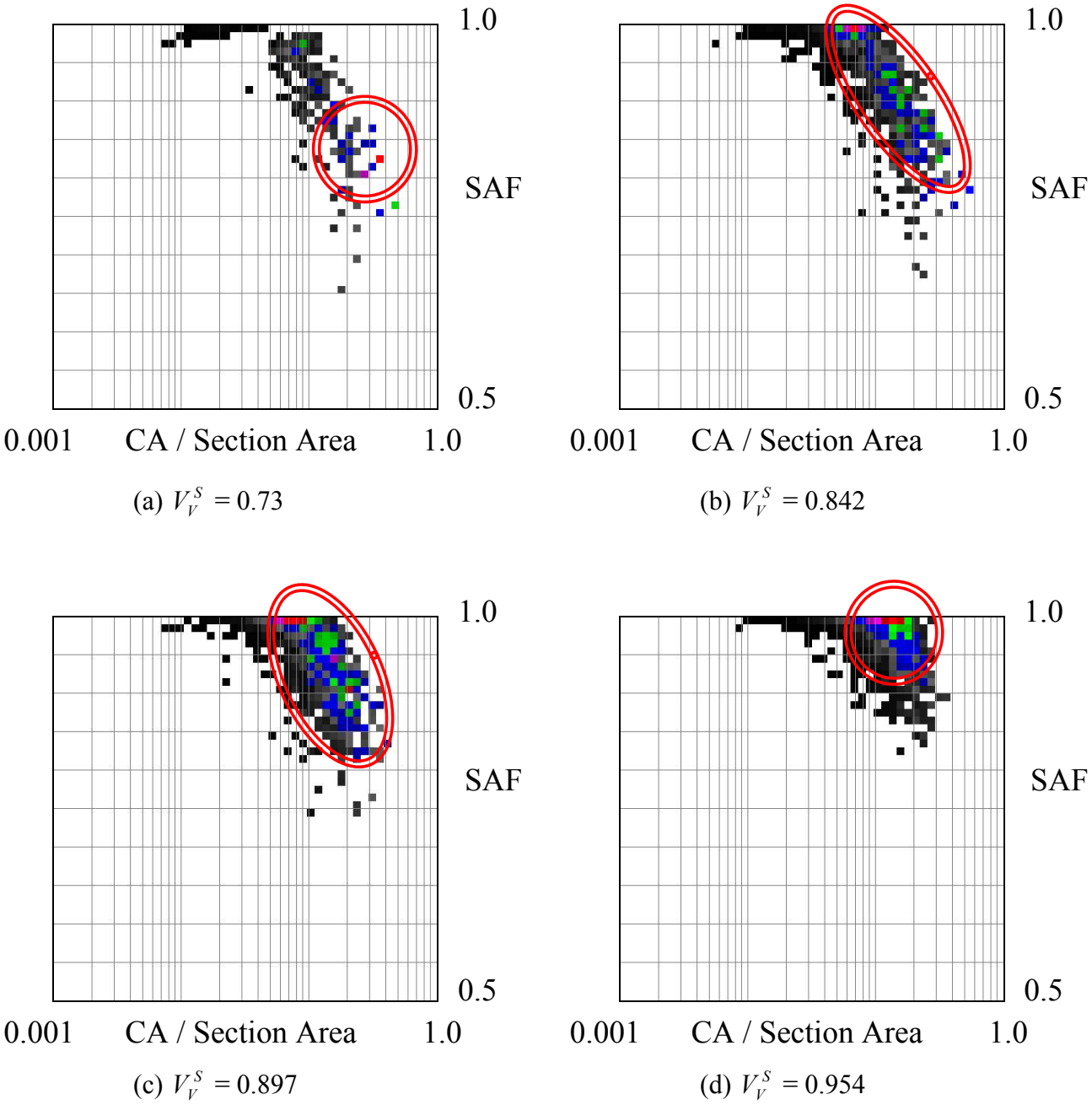

Figure 59. 2-D SAF vs. CA Maps for isotropic, homogeneous sintering; no agglomerations.

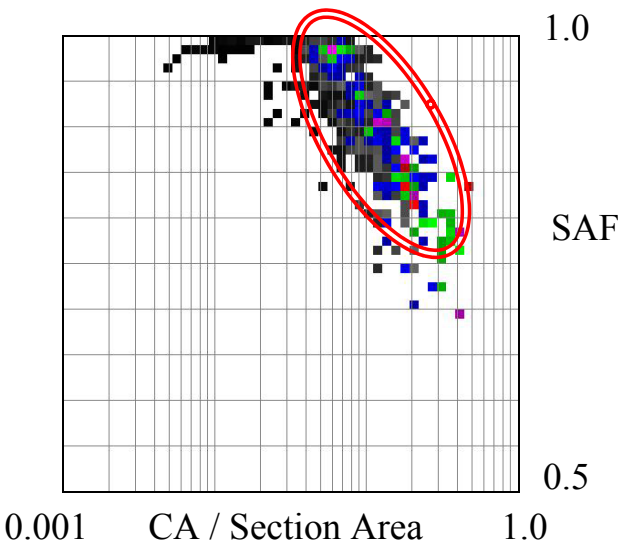

(a) $V_V^S = 0.756$

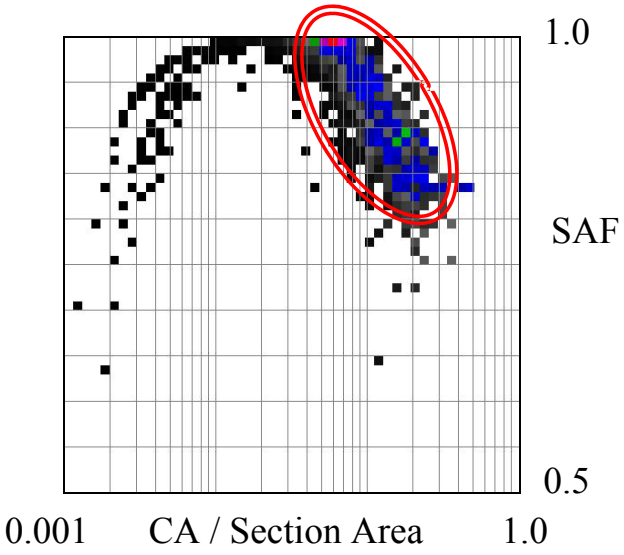

(b) $V_V^S = 0.845$

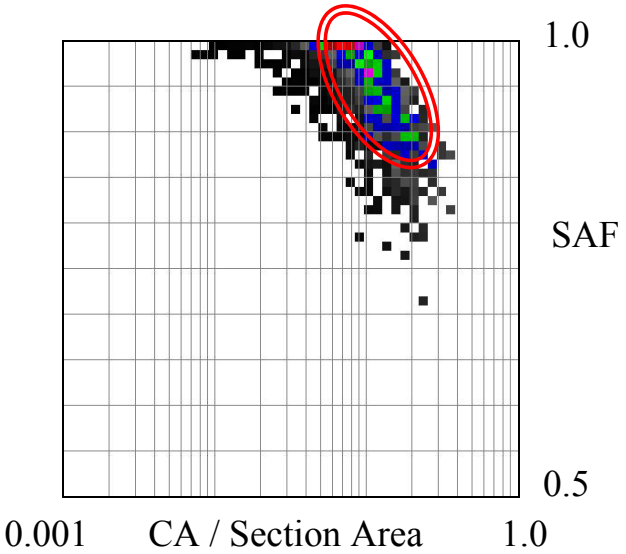

(c) $V_V^S = 0.902$

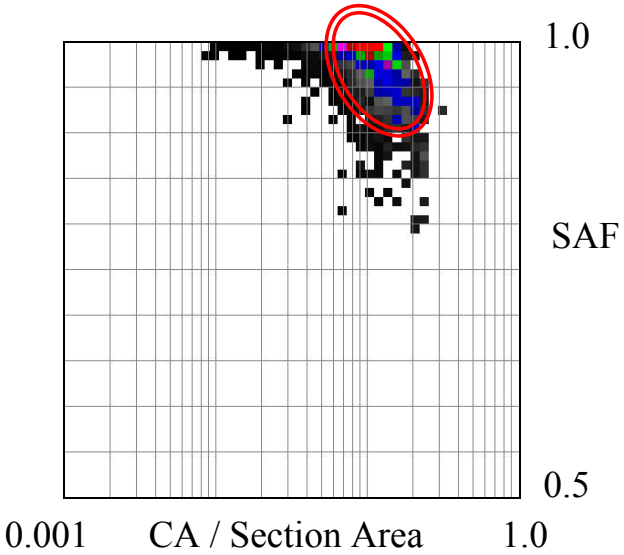

(d) $V_V^S = 0.945$

Figure 60. 2-D SAF vs. CA Maps for sintering via LPR (μ^t=0.01, μ^n=0.1); no agglomeration.

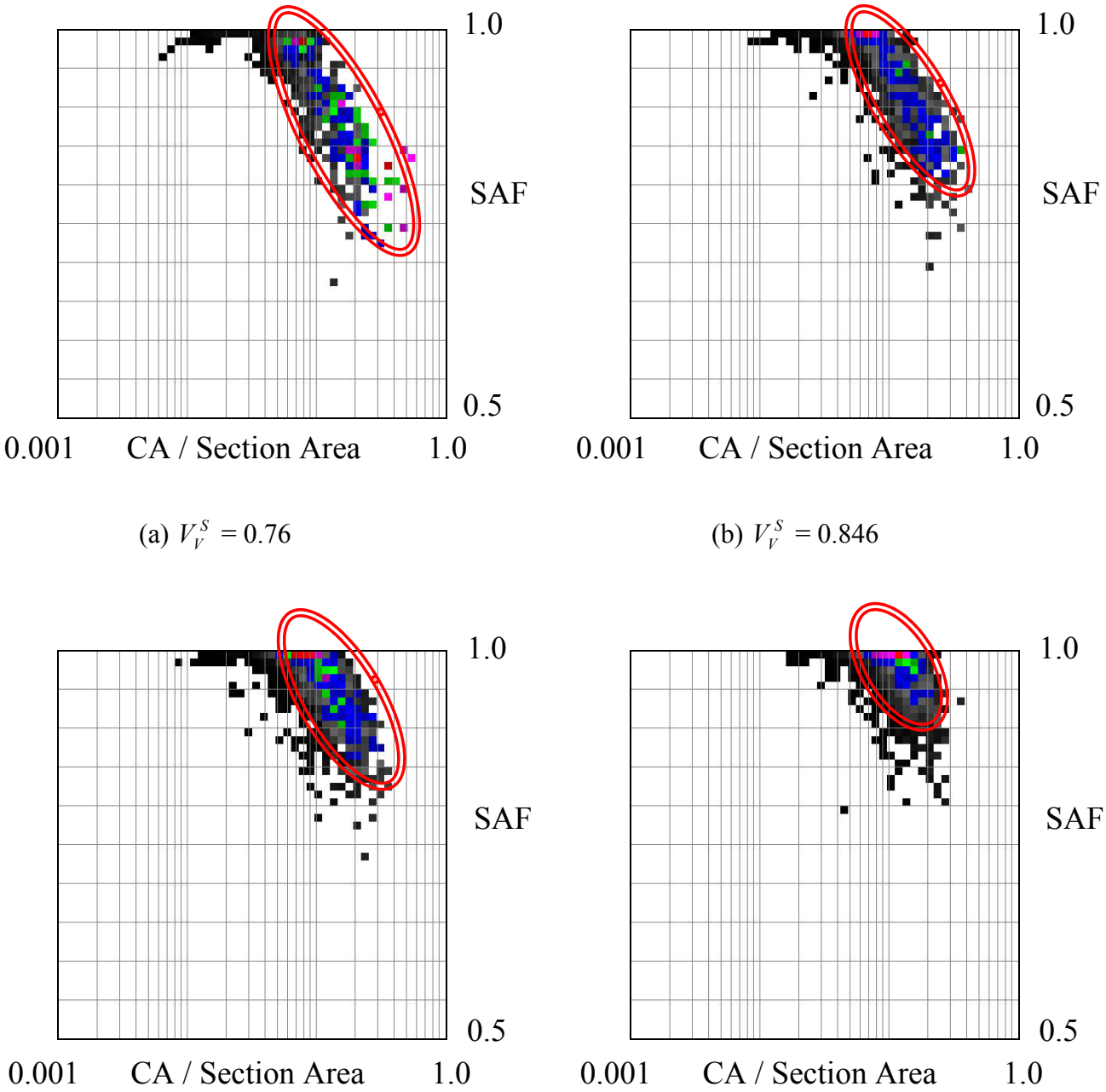

(a) $V_V^S = 0.76$

(b) $V_V^S = 0.846$

(c) $V_V^S = 0.90$

(d) $V_V^S = 0.947$

Figure 61. 2-D SAF vs. CA Maps for sintering via LPR (μ^t=0.1, μ^n=0.1); no agglomerations.

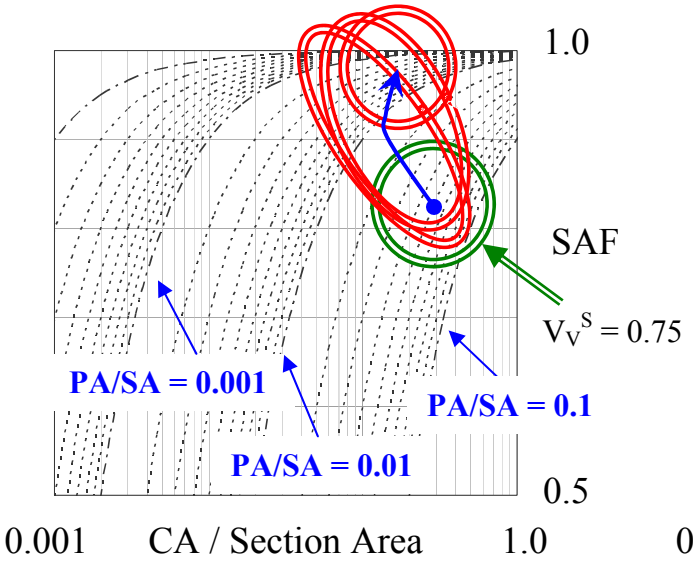

(a) Isotropic, homogenous sintering.

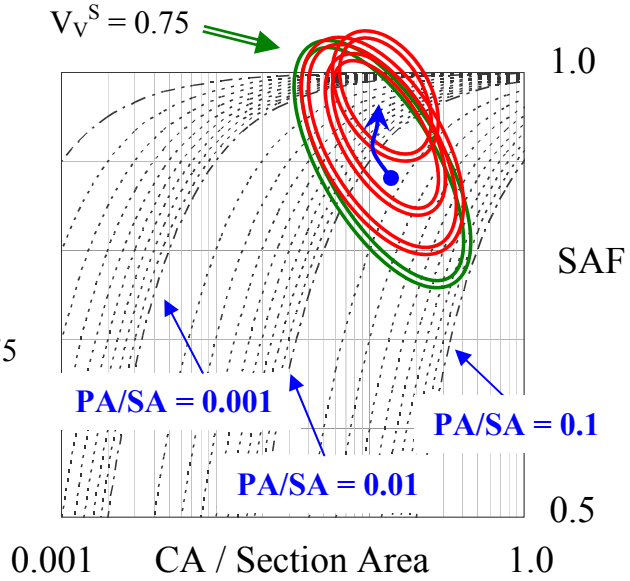

(b) Sintering via LPR (μ^t=0.01, μ^n=0.1).

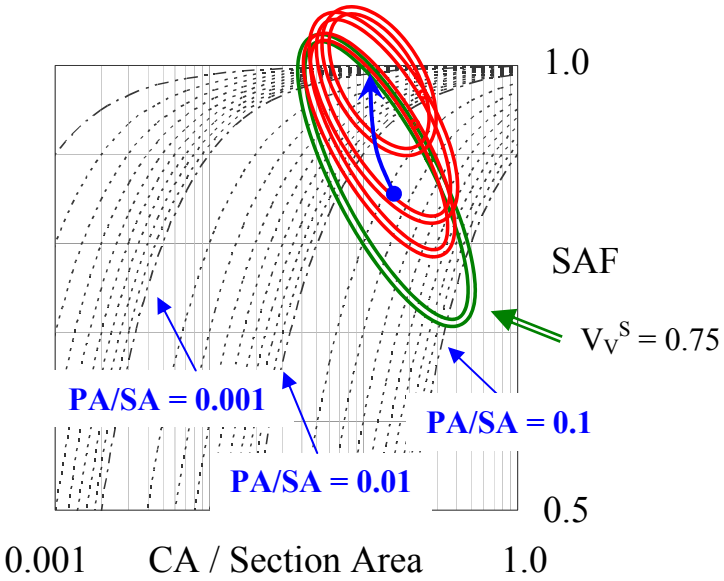

(c) Sintering via LPR (μ^t=0.1, μ^n=0.1).

Figure 62. Comparison of peak motion for densification of particle arrangements with no agglomerations.

The 2-D SAF vs. CA Maps for the second set of simulations of the particle arrangement with agglomeration are shown in Figure 63 for the case of isotropic, homogenous sintering, in Figure 64 for the case of sintering using LPR with μ^t=0.01 and μ^n=0.1, and Figure 65 for sintering using LPR with μ^t=0.01 and μ^n=0.1 with the peaks are highlighted. The peaks for the different solid volume fractions are superimposed on the 2-D SAF vs. CA Maps in Figure 66 for each simulation in order to trace the movement of the peak as densification progresses.

An examination of the peak paths in Figure 66 shows that the peaks at the lower solid volume fractions (V_V^S = 0.75) have a relatively narrow distribution with cells of high SAF when compared to the results for the particle arrangements with no agglomerations shown in Figure 62. As densification progresses, the motion of the peaks is primarily to the right. However, the distribution of tessellation cell properties expands at higher solid volume fractions (V_V^S = 0.95) for two of the simulations. A possible explanation for this atypical behavior of the peak motion is evident from the cross sections. Initially, some of the large pores are open to the edge of the simulation as shown in Figure 56(b). Because the pore is not enclosed, no tessellation cell is generated and the pore is not included in the data. Then, as densification progresses in the simulation, some of these pores eventually close off at the edges of the cross sections as shown in Figure 56(c). This creates large tessellation cells with low solid area fraction (SAF) which were not present at the lower solid volume fractions. Because the pore is now enclosed, a tessellation cell can be formed and its cell properties included in the data. The appearance of these cells in the statistical data results in the shift to a wider peak distribution at the higher solid volume fractions (V_V^S = 0.95) as shown in Figure 66(a) and Figure 66(c). To avoid this problem, more particles are needed in the simulation to enclose the larger voids present in the

agglomeration particle arrangements in order to enclose enough pores to generate sufficient statistical data using tessellation. At present, the amount of memory space required to solve the force and moment equilibrium equations and the limitations of the software application size restrict the maximum number of particles in the containing volume to approximately 800.

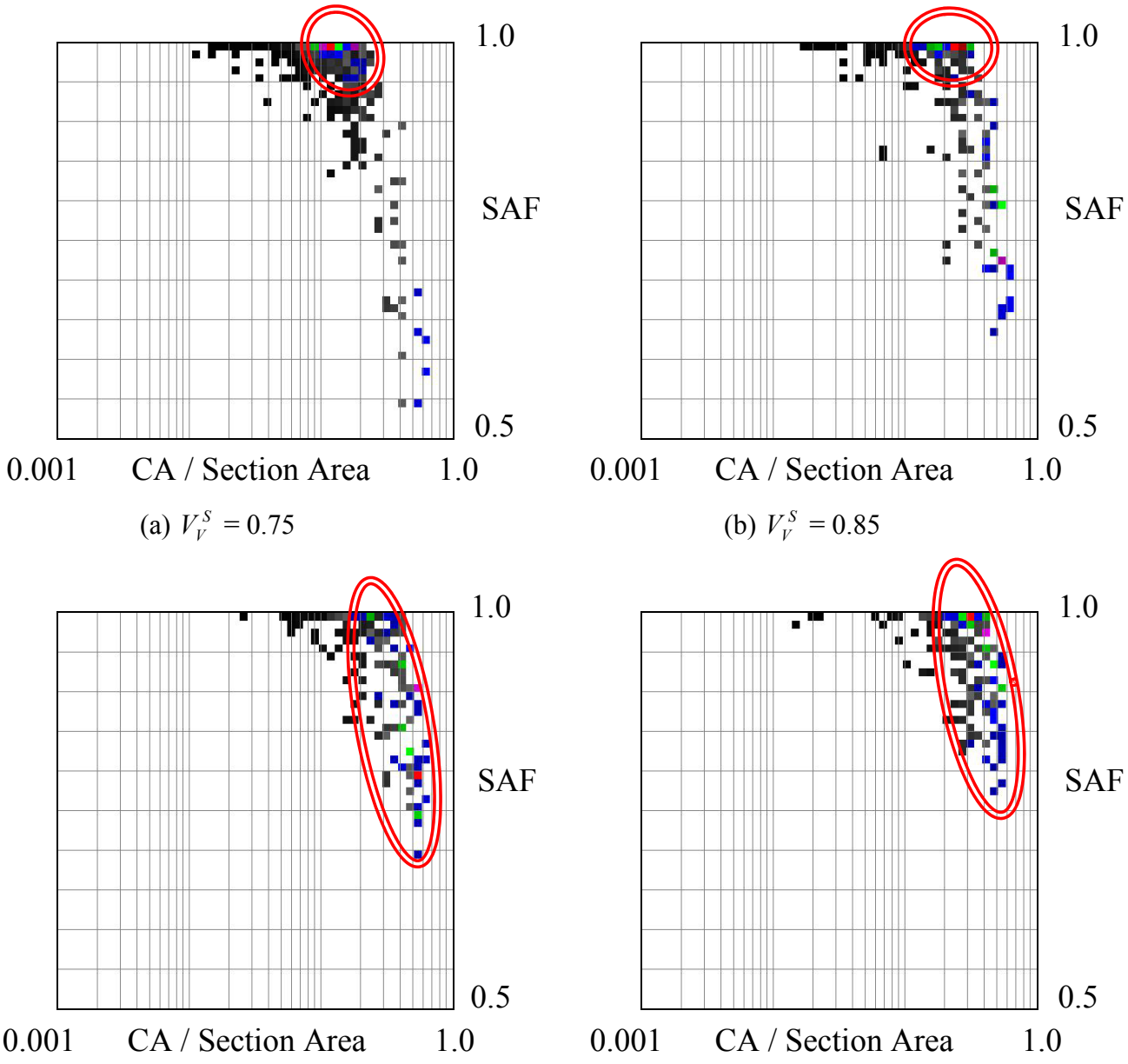

Figure 63. 2-D SAF vs. CA Maps for isotropic, homogeneous sintering; agglomeration.

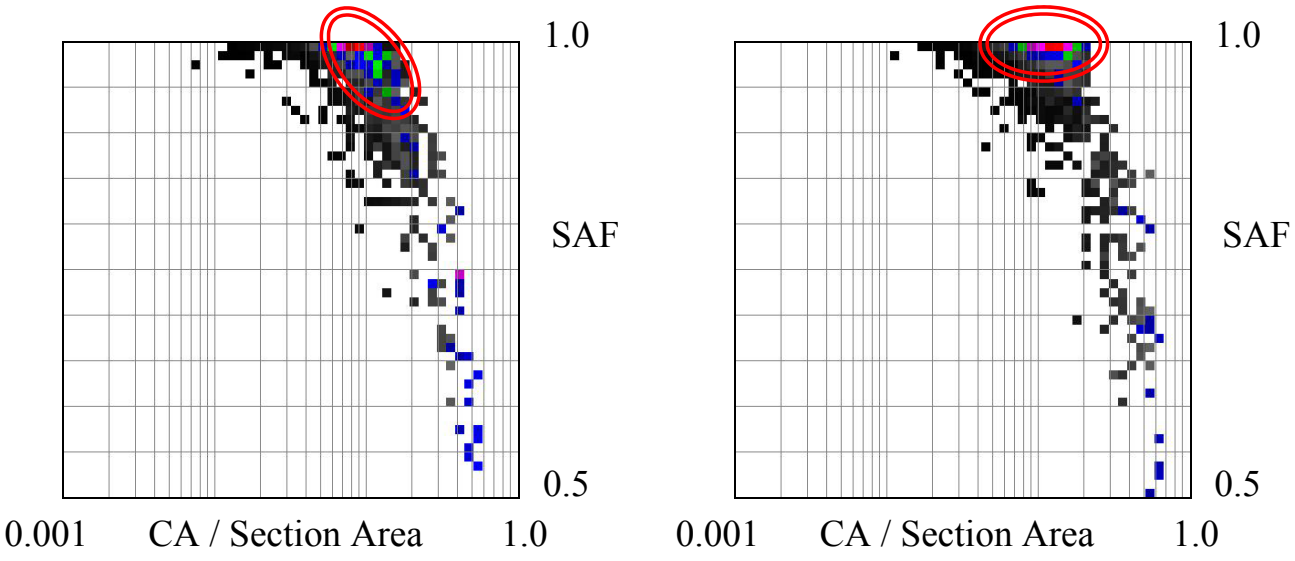

(a) $V_V^S = 0.75$ (b) $V_V^S = 0.843$

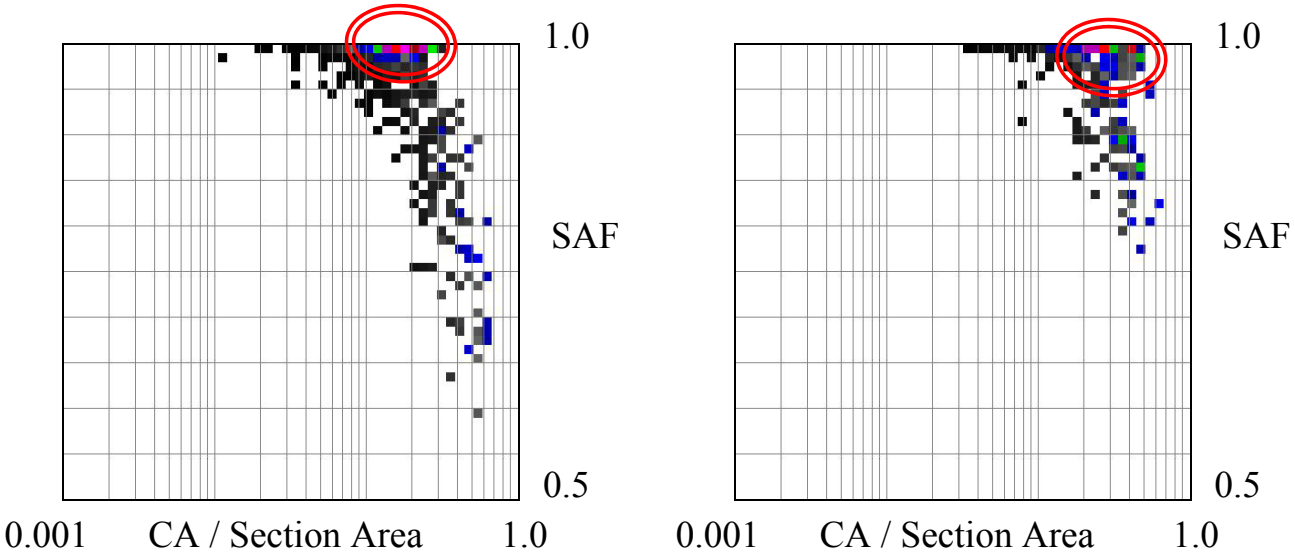

(c) $V_V^S = 0.90$ (d) $V_V^S = 0.951$

Figure 64. 2-D SAF vs. CA Maps for sintering via LPR (μ^t=0.01, μ^n=0.1); agglomeration.

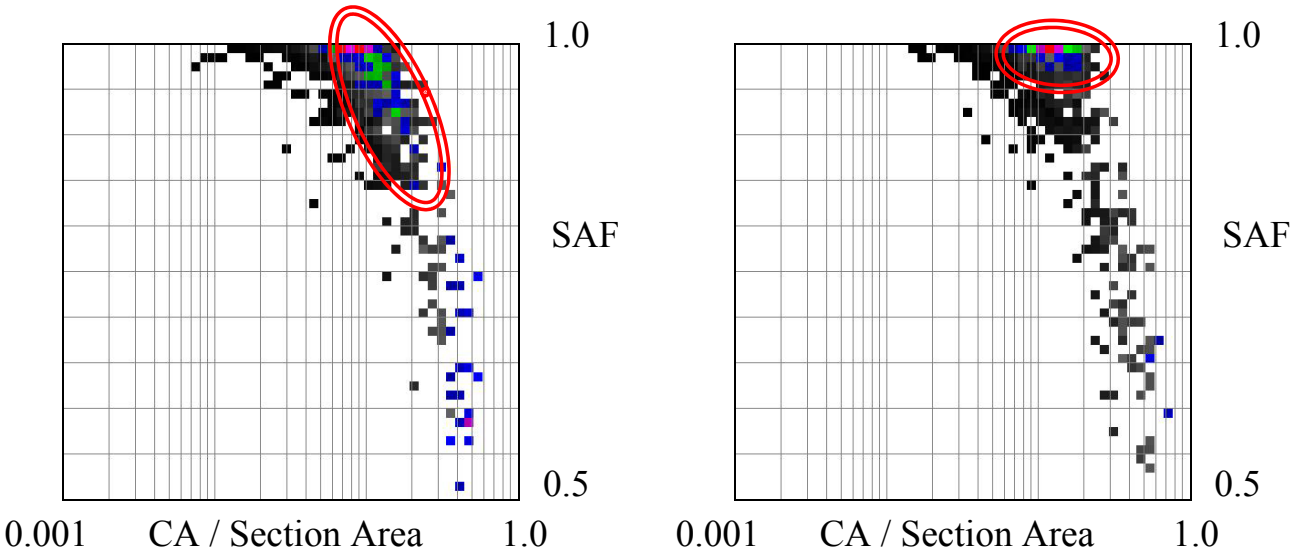

(a) $V_V^S = 0.75$ (b) $V_V^S = 0.844$

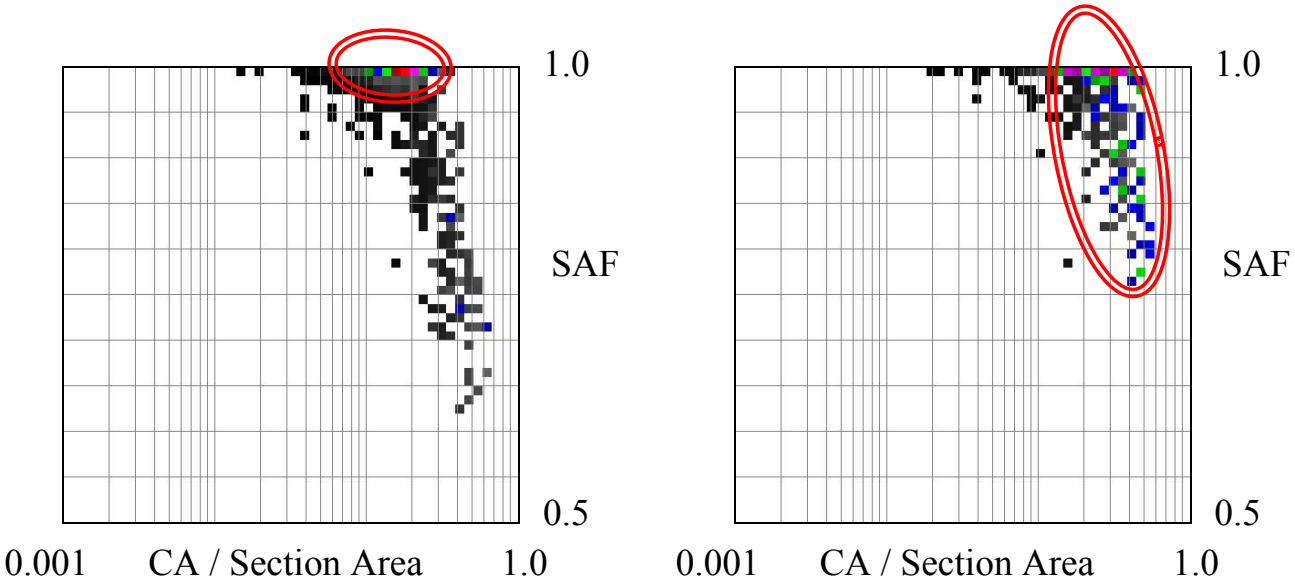

(c) $V_V^S = 0.90$ (d) $V_V^S = 0.951$

Figure 65. 2-D SAF vs. CA Maps for sintering via LPR (μ^t=0.1, μ^n=0.1); agglomeration.

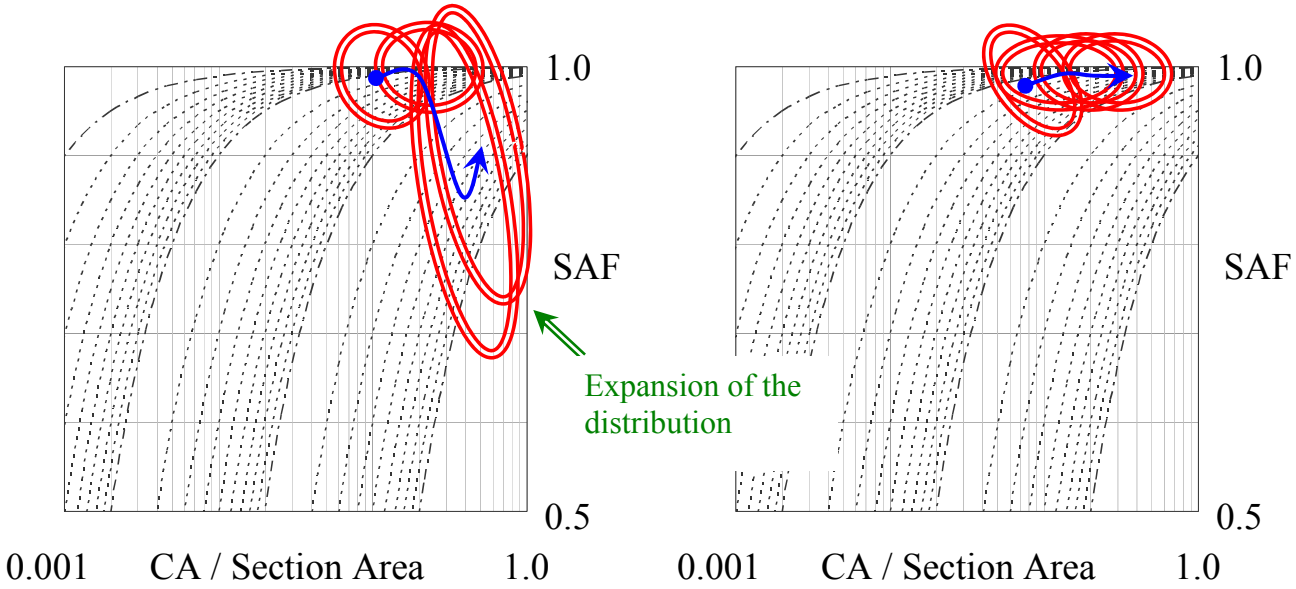

(a) Isotropic, homogenous sintering.

(b) Sintering via LPR (μ^t=0.01, μ^n=0.1).

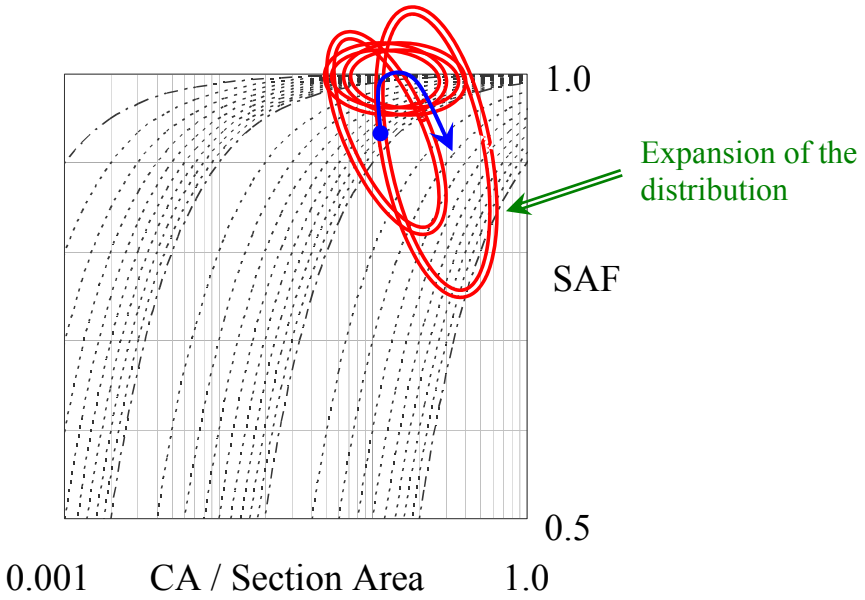

(c) Sintering via LPR (μ^t=0.1, μ^n=0.1).

Figure 66. Comparison of peak motion for densification of particle arrangements with agglomerations.

7.0 SUMMARY AND CONCLUSIONS

To summarize, a 3-D model has been developed with the goal of simulating the behavior of real sintered material which incorporated the following main features:

1. The use of an algorithm to control the random motion of the particles to improve the efficiency of the packing of the particles into a containing volume.
2. The adaptation of Monte Carlo integration techniques to calculate, for the simulation, the stereological parameters which are commonly used to characterize sintered materials in experiments.
3. The introduction of a technique to simulate agglomerated particle arrangements.
4. The application of tessellation to 2-D cross sections taken from the Representative Volume Element (RVE) generated by the simulation.
5. The derivation of force and moment equilibrium equations to allow for Local Particle Rearrangement in the RVE.

The model was compared to experimental data obtained from measurements on sintered alumina samples using two techniques: the stereological parameters for the RVE determined by the simulation, and additional measurable quantities obtained from applying tessellation to cross sections taken from the RVE to further describe the characteristics of the microstructure. Based

on the analysis of the simulation results and a comparison to experimental data, the following observations were made:

1. The simulation reproduced behavioral trends in the microstructure similar to those observed in the measurement of the experimental samples using the $\overline{S}^{SS}$ vs. V_V^S curves and tracing the peak movements on the 2-D SAF vs. CA Maps, thereby demonstrating the feasibility of employing the 3-D simulations to replicate the microstructural behavior observed in real sintered materials.
2. The results from Section 5.0 indicate that the generation of agglomerated particle packing arrangements may be useful in simulating the microstructural evolution of sintering since the presence of the large voids used to simulate agglomeration had a significant effect on the simulation results.
3. The simulation results for isotropic, homogenous sintering indicate that approximately 10,000 particles are needed to properly model agglomeration in the particle arrangement.
4. Based on the $\overline{S}^{SS}$ vs. V_V^S curves, there was no difference between the isotropic, homogenous simulation and the LPR simulations for the particle arrangement with no agglomerations. However, there was a noticeable difference between the isotropic, homogenous simulation and the LPR simulations for the particle arrangement with agglomeration.
5. The comparison of the cross sections for the LPR simulations using different viscosity values suggests that the ability of the particles to slide past each other, modeled in the simulation by the tangential viscosity, may influence the rate at which small pores are formed and/or eliminated in the RVE.

6. The LPR simulations for particle arrangements with agglomeration were inconclusive since there were insufficient particles (only 800 particles) in RVE to close off the pores from the edges.

The analysis of the features shows the advantages of simulations as a tool for examining the evolution microstructural. While additional development of the model is needed, once the simulation has been fully validated through comparison to experimental results, the behavior of different local packing arrangements can be analyzed both in terms of their control of the densification rate and the generation of defects by sintering.

8.0 FUTURE WORK

As outlined in the previous section, the model presented in this study has introduced several improvements to the techniques used in models to simulate the microstructural behavior of real sintered materials. However, there are three primary areas where additional research is needed to further improve the model:

1. Increase the number of particles in the Representative Volume Element (RVE) for sintering using Local Particle Rearrangement (LPR).

   As demonstrated by the simulation results, it is possible to replicate agglomerations in the particle arrangement. Unfortunately, a larger number of particles are required in the RVE n order to isolate the pores so the statistical data can be determined. While this is possible for the case of isotropic, homogenous sintering (see results from Section 5.0), it is not possible for the case of sintering using Local Particle Rearrangement (LPR) due to the amount of memory space required to store the variables needed to compile and solve the matrix to establish force and moment equilibrium for each step of the simulated sintering process which limits the number of particles for the simulation with local particle rearrangement to approximately 800 particles. The coefficient matrix used to determine the velocities and rotations to establish equilibrium is sparsely populated (i.e. mostly zero terms). Thus, it is possible to increase the number of particles in the LPR simulations by implementing sparse

matrix techniques to reduce the overall memory space required to store and solve the matrix. Once this is achieved, a better analysis of the LPR simulations can be made. The simulation results for the isotropic, homogenous sintering of the agglomerated particle arrangement (Section 5.0) indicate that approximately 10,000 particles are needed in the RVE to adequately model agglomerated particle arrangements.

2. How to determine the correct values for the normal and tangential viscosities.

   The values for the normal and tangential viscosities used in the simulation were arbitrarily chosen to explore how they may influence the simulation results. Before a direct comparison to experimental results can truly be made, appropriate values for the viscosities have to be determined for the real material being simulated.

3. Exploring better ways to simulate agglomeration in the particle arrangement.

   Ideally, the pore distribution in the RVE for the simulation should match the properties distribution of the tessellation cells measured from experimental samples. In the present simulation, agglomeration was simulated in the particle arrangement by the random removal of particles from the initial packed RVE. This technique may not be sufficient to achieve a good statistical match. Therefore, additional research needs to be conducted to determine the most efficient manner in which to match the simulation and experimental distribution.

APPENDIX

DERIVATION OF THE EQUATIONS OF MOTION GOVERNING LOCAL PARTICLE REARRANGEMENT (LPR).

Equations governing the movement of the particles inside the RVE are used to determine the linear and angular velocities of the particle centers required to establish force and moment equilibrium for all the particles in the simulation. The derivation of the equations is based on the model of a pair of overlapping particle as shown in Figure 67:

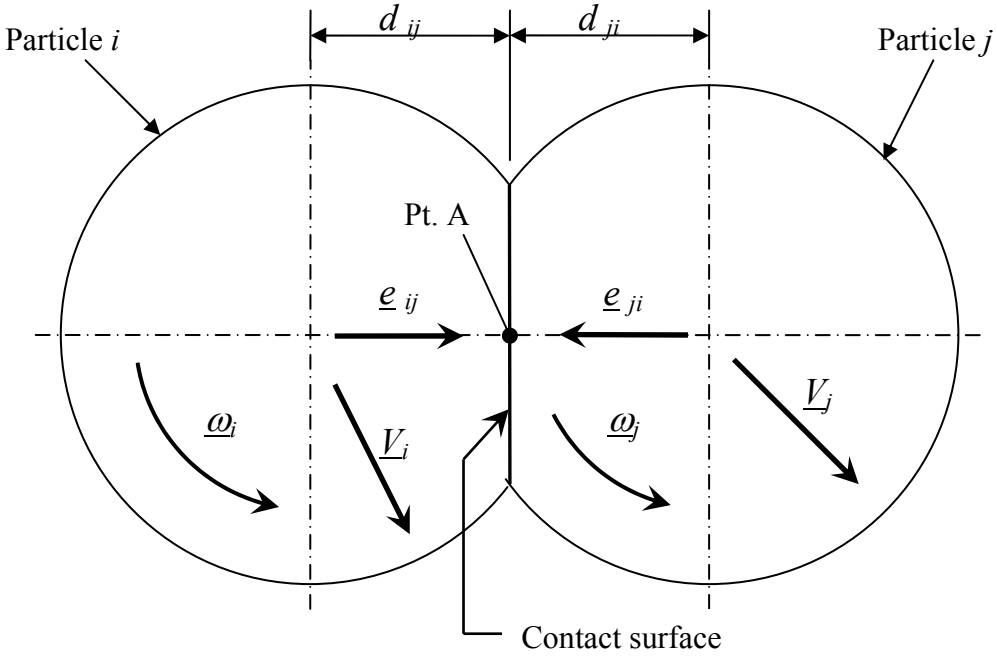

Figure 67. Geometry of particle motion of two particles in contact.

The definitions of the variables labeled in Figure 67 are:

i, j = Indices identifying individual particles. Variable i identifies the current particle and variable j identifies the overlapping particle.

d_{ij} = Distance from center of particle i to the contact surface.

d_{ji} = Distance from center of particle j to the contact surface.

$\underline{e}_{ij}$ = Unit vector identifying direction from center of particle i to contact surface.

$\underline{e}_{ji}$ = Unit vector identifying direction from center of particle j to contact surface.

$\underline{\omega}_i, \underline{\omega}_j$ = Angular velocities of particles i and j respectively.

$\underline{V}_i, \underline{V}_j$ = Linear velocities of particles i and j respectively.

For the purposes of this derivation, vector quantities are underlined; the unit vectors for coordinates are identified by $\underline{i}, \underline{j}$ and $\underline{k}$; and the scalar components of a vector are denoted using a superscript.

A.1 DEFINITION OF NORMAL AND TANGENTIAL VELOCITIES

The difference in velocity of particle *j* with respects to the velocity of particle *i* at the center of the circular contact surface (labeled as Pt. A in Figure 67) is given by:

$$\Delta\underline{V}_{ji} = \underline{V}_j + \underline{\omega}_j \times d_{ji}\underline{e}_{ji} - \left(\underline{V}_i + \underline{\omega}_i \times d_{ij}\underline{e}_{ij}\right)$$

$$\Delta\underline{V}_{ji} = \underline{V}_j - \underline{V}_i + \underline{\omega}_j \times d_{ji}\underline{e}_{ji} - \underline{\omega}_i \times d_{ij}\underline{e}_{ij}$$

$$\Delta\underline{V}_{ji} = \underline{V}_j - \underline{V}_i - \underline{\omega}_j \times d_{ji}\underline{e}_{ij} - \underline{\omega}_i \times d_{ij}\underline{e}_{ij} \qquad \text{(Note: } \underline{e}_{ij} = -\underline{e}_{ji}\text{)} \qquad \text{[A1]}$$

Expansion of the cross products in equation [A1] yields the following expressions,

$$\underline{\omega}_j \times d_{ji}\underline{e}_{ij} = d_{ji}\left[\left(\omega_j^Y e_{ij}^Z - \omega_j^Z e_{ij}^Y\right)\underline{i} - \left(\omega_j^X e_{ij}^Z - \omega_j^Z e_{ij}^X\right)\underline{j} + \left(\omega_j^X e_{ij}^Y - \omega_j^Y e_{ij}^X\right)\underline{k}\right] \qquad \text{[A2]}$$

$$\underline{\omega}_i \times d_{ij}\underline{e}_{ij} = d_{ij}\left[\left(\omega_i^Y e_{ij}^Z - \omega_i^Z e_{ij}^Y\right)\underline{i} - \left(\omega_i^X e_{ij}^Z - \omega_i^Z e_{ij}^X\right)\underline{j} + \left(\omega_i^X e_{ij}^Y - \omega_i^Y e_{ij}^X\right)\underline{k}\right]$$

Substitution of equations [A2] into equation [A1] and adding the scalar components for the velocities results in the follow expression,

$$\begin{aligned}\Delta\underline{V}_{ji} &= \left(V_j^X - V_i^X\right)\underline{i} + \left(V_j^Y - V_i^Y\right)\underline{j} + \left(V_j^Z - V_i^Z\right)\underline{k} \\ &- d_{ji}\left[\left(\omega_j^Y e_{ij}^Z - \omega_j^Z e_{ij}^Y\right)\underline{i} - \left(\omega_j^X e_{ij}^Z - \omega_j^Z e_{ij}^X\right)\underline{j} + \left(\omega_j^X e_{ij}^Y - \omega_j^Y e_{ij}^X\right)\underline{k}\right] \\ &- d_{ij}\left[\left(\omega_i^Y e_{ij}^Z - \omega_i^Z e_{ij}^Y\right)\underline{i} - \left(\omega_i^X e_{ij}^Z - \omega_i^Z e_{ij}^X\right)\underline{j} + \left(\omega_i^X e_{ij}^Y - \omega_i^Y e_{ij}^X\right)\underline{k}\right] \qquad \text{[A3]}\end{aligned}$$

The coefficients of unit vectors for the Cartesian coordinate system can be combined to give,

$$\begin{aligned}\Delta V_{ji} &= \left[V_j^X - V_i^X - d_{ji}\left(\omega_j^Y e_{ij}^Z - \omega_j^Z e_{ij}^Y\right) - d_{ij}\left(\omega_i^Y e_{ij}^Z - \omega_i^Z e_{ij}^Y\right)\right]\underline{i} \\ &+ \left[V_j^Y - V_i^Y + d_{ji}\left(\omega_j^X e_{ij}^Z - \omega_j^Z e_{ij}^X\right) + d_{ij}\left(\omega_i^X e_{ij}^Z - \omega_i^Z e_{ij}^X\right)\right]\underline{j} \\ &+ \left[V_j^Z - V_i^Z - d_{ji}\left(\omega_j^X e_{ij}^Y - \omega_j^Y e_{ij}^X\right) - d_{ij}\left(\omega_i^X e_{ij}^Y - \omega_i^Y e_{ij}^X\right)\right]\underline{k} \qquad \text{[A4]}\end{aligned}$$

Since $\underline{e}_{ij}$ is a unit vector, the relative velocity normal to the contact surface contact ($\Delta\underline{V}_{ji}^n$) is given by the projection of $\Delta\underline{V}_{ji}$ onto $\underline{e}_{ij}$,

$$\Delta\underline{V}_{ji}^n = \left(\Delta\underline{V}_{ji} \cdot \underline{e}_{ij}\right)\underline{e}_{ij} = \left[\left(\underline{V}_j - \underline{V}_i - \underline{\omega}_j \times d_{ji}\underline{e}_{ij} - \underline{\omega}_i \times d_{ij}\underline{e}_{ij}\right) \cdot \underline{e}_{ij}\right]\underline{e}_{ij} \qquad \text{[A5]}$$

where superscripts ^{n} and ^{t} refer to the vectors normal and tangential to the contact surface respectively. In general, $\left(\underline{a} \times \underline{b}\right) \cdot \underline{b} = \underline{0}$ due to orthogonality. Therefore, the terms $\left(\underline{\omega}_j \times d_{ji}\underline{e}_{ij}\right) \cdot \underline{e}_{ij}$ and $\left(\underline{\omega}_i \times d_{ij}\underline{e}_{ij}\right) \cdot \underline{e}_{ij}$ in equation [A5] are equal to zero. This reduces equation [A5] to,

$$\Delta \underline{V}_{ji}^{n} = \left[\left(\underline{V}_j - \underline{V}_i\right)\cdot \underline{e}_{ij}\right]\underline{e}_{ij}$$

$$= \left[\left(V_j^X e_{ij}^X + V_j^Y e_{ij}^Y + V_j^Z e_{ij}^Z\right) - \left(V_i^X e_{ij}^X + V_i^Y e_{ij}^Y + V_i^Z e_{ij}^Z\right)\right]\underline{e}_{ij}$$

$$= \left[\left(V_j^X - V_i^X\right)e_{ij}^X + \left(V_j^Y - V_i^Y\right)e_{ij}^Y + \left(V_j^Z - V_i^Z\right)e_{ij}^Z\right]\underline{e}_{ij} \qquad \text{[A6]}$$

The relative velocity tangential to the contact surface($\Delta \underline{V}_{ji}^{t}$) is given by:

$$\Delta \underline{V}_{ji}^{t} = \Delta \underline{V}_{ji} - \Delta \underline{V}_{ji}^{n} = \underline{V}_j - \underline{V}_i - \left(d_{ji}\underline{\omega}_j + d_{ij}\underline{\omega}_i\right)\times \underline{e}_{ij} - \left[\left(\underline{V}_j - \underline{V}_i\right)\cdot \underline{e}_{ij}\right]\underline{e}_{ij} \qquad \text{[A7]}$$

A.2 EQUATIONS FOR FORCE EQUILIBRIUM

The free body diagram (FBD) of the interaction between two overlapping particles i and j as shown in Figure 68 is used to determine the relationship between the forces and the velocities acting on the particles.

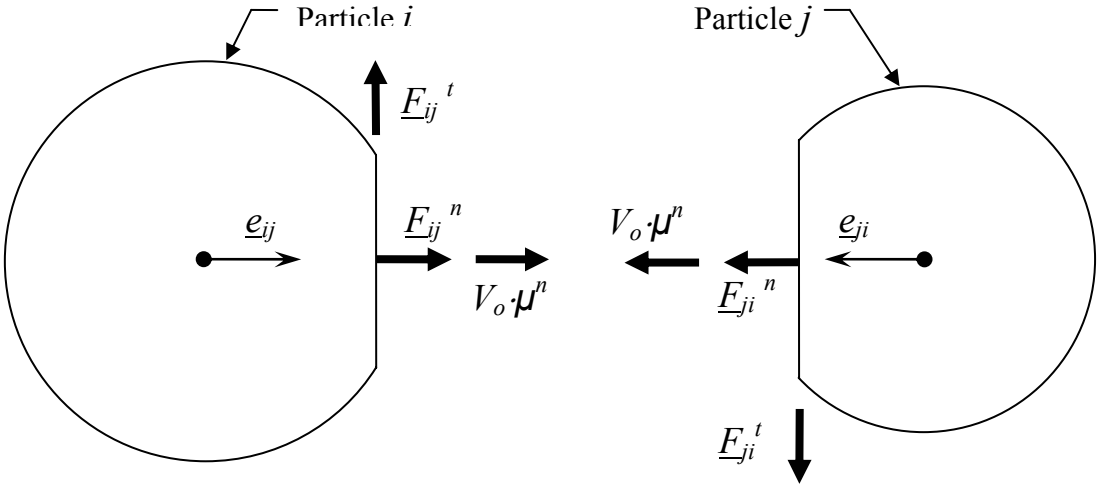

Figure 68. Forces resulting from the interaction of two particles in contact.

The definitions of the variables labeled in Figure 68 are:

$\underline{F}_{ij}^{n}$ = Normal contact force exerted on particle *i* by particle *j*.

$\underline{F}_{ji}^{n}$ = Normal contact force exerted on particle *j* by particle *i*.

$\underline{F}_{ij}^{t}$ = Tangential contact force exerted on particle *i* by particle *j*.

$\underline{F}_{ji}^{t}$ = Tangential contact force exerted on particle *j* by particle *i*.

$\underline{e}_{ij}$ = Unit vector identifying direction from center of particle *i* to contact surface.

$\underline{e}_{ij}$ = Unit vector identifying direction from center of particle *j* to contact surface.

V_0 = Velocity term to model tendency of particles to move towards each other in sintering. Note that $V_0 = f\left(R_i, R_j, CDIST_{ij}\right)$.

μ^t = Tangential viscosity term to model material properties of the simulated body.

μ^n = Normal viscosity term to model material properties of the simulated body.

From Figure 68, a summation of the forces normal and tangential to the surface of contact acting on particle *i* results in the following equations:

$$\underline{F}_{ji}^{n} = \mu^{n}\left(\Delta\underline{V}_{ji}^{n} - V_0\,\underline{e}_{ij}\right) \qquad \text{[A8]}$$

$$\underline{F}_{ji}^{t} = \mu^{t}\left(\Delta\underline{V}_{ji}^{t}\right) \qquad \text{[A9]}$$

$$\underline{F}_{ji}^{n} + \underline{F}_{ji}^{t} = \mu^{n}\left(\Delta\underline{V}_{ji}^{n} - V_0\,\underline{e}_{ij}\right) + \mu^{t}\Delta\underline{V}_{ji}^{t} \qquad \text{[A10]}$$

Substituting equation [A7] ($\Delta\underline{V}_{ji}^{t} = \Delta\underline{V}_{ji} - \Delta\underline{V}_{ji}^{n}$) gives,

$$\underline{F}_{ji}^{n} + \underline{F}_{ji}^{t} = \mu^{n}\left(\Delta\underline{V}_{ji}^{n} - V_0\,\underline{e}_{ij}\right) + \mu^{t}\left(\Delta\underline{V}_{ji} - \Delta\underline{V}_{ji}^{n}\right)$$

Rearranging variables,

$$\underline{F}_{ji}^{n} + \underline{F}_{ji}^{t} = \left(\mu^{n} - \mu^{t}\right)\left(\Delta\underline{V}_{ji}^{n}\right) - \mu^{n}V_0\,\underline{e}_{ij} + \mu^{t}\left(\Delta\underline{V}_{ji}\right) \qquad \text{[A11]}$$

Recall that $\underline{e}_{ij} = e_{ij}^{X}\,\underline{i} + e_{ij}^{Y}\,\underline{j} + e_{ij}^{Z}\,\underline{k}$. Substituting this and the expressions for $\Delta\underline{V}_{ji}^{n}$ and $\Delta\underline{V}_{ji}$ (i.e. equations [A6] and [A4]) into equation [A11] gives,

$$\begin{aligned}\underline{F}_{ji}^{n} + \underline{F}_{ji}^{t} = {} & \left(\mu^{n} - \mu^{t}\right)\left(\left[V_j^{X} - V_i^{X}\right]e_{ij}^{X} + \left[V_j^{Y} - V_i^{Y}\right]e_{ij}^{Y} + \left[V_j^{Z} - V_i^{Z}\right]e_{ij}^{Z}\right)\left(e_{ij}^{X}\,\underline{i} + e_{ij}^{Y}\,\underline{j} + e_{ij}^{Z}\,\underline{k}\right) \\ & - \mu^{n}V_0\left(e_{ij}^{X}\,\underline{i} + e_{ij}^{Y}\,\underline{j} + e_{ij}^{Z}\,\underline{k}\right) \\ & \mu^{t}\left\{\left[V_j^{X} - V_i^{X} - d_{ji}\left(\omega_j^{Y}e_{ij}^{Z} - \omega_j^{Z}e_{ij}^{Y}\right) - d_{ij}\left(\omega_i^{Y}e_{ij}^{Z} - \omega_i^{Z}e_{ij}^{Y}\right)\right]\underline{i}\right.\end{aligned}$$

$$+\left[V_j^Y - V_i^Y + d_{ji}\left(\omega_j^X e_{ij}^Z - \omega_j^Z e_{ij}^X\right) + d_{ij}\left(\omega_i^X e_{ij}^Z - \omega_i^Z e_{ij}^X\right)\right]\underline{j}$$

$$+\left[V_j^Z - V_i^Z - d_{ji}\left(\omega_j^X e_{ij}^Y - \omega_j^Y e_{ij}^X\right) - d_{ij}\left(\omega_i^X e_{ij}^Y - \omega_i^Y e_{ij}^X\right)\right]\}\underline{k} \qquad \text{[A12]}$$

Rearranging equation [A12] to combine the coefficients of **i**, **j**, and **k** gives:

$$\begin{aligned}
\underline{F}_{ji}^n + \underline{F}_{ji}^t = {} & \left\{\left(\mu^n - \mu^t\right)\left[\left(V_j^X - V_i^X\right)e_{ij}^X + \left(V_j^Y - V_i^Y\right)e_{ij}^Y + \left(V_j^Z - V_i^Z\right)e_{ij}^Z\right]e_{ij}^X - \mu^n V_0 e_{ij}^X\right. \\
& + \mu^t\left[V_j^X - V_i^X - d_{ji}\left(\omega_j^Y e_{ij}^Z - \omega_j^Z e_{ij}^Y\right) - d_{ij}\left(\omega_i^Y e_{ij}^Z - \omega_i^Z e_{ij}^Y\right)\right]\}\underline{i} \\
& + \left\{\left(\mu^n - \mu^t\right)\left[\left(V_j^X - V_i^X\right)e_{ij}^X + \left(V_j^Y - V_i^Y\right)e_{ij}^Y + \left(V_j^Z - V_i^Z\right)e_{ij}^Z\right]e_{ij}^Y - \mu^n V_0 e_{ij}^Y\right. \\
& + \mu^t\left[V_j^Y - V_i^Y + d_{ji}\left(\omega_j^X e_{ij}^Z - \omega_j^Z e_{ij}^X\right) + d_{ij}\left(\omega_i^X e_{ij}^Z - \omega_i^Z e_{ij}^X\right)\right]\}\underline{j} \\
& + \left\{\left(\mu^n - \mu^t\right)\left[\left(V_j^X - V_i^X\right)e_{ij}^X + \left(V_j^Y - V_i^Y\right)e_{ij}^Y + \left(V_j^Z - V_i^Z\right)e_{ij}^Z\right]e_{ij}^Z - \mu^n V_0 e_{ij}^Z\right. \\
& + \mu^t\left[V_j^Y - V_i^Y - d_{ji}\left(\omega_j^X e_{ij}^Y - \omega_j^Y e_{ij}^X\right) - d_{ij}\left(\omega_i^X e_{ij}^Y - \omega_i^Y e_{ij}^X\right)\right]\}\underline{k} \qquad \text{[A13]}
\end{aligned}$$

To split up equation [A13] into matrix form, set each $\underline{i}$, $\underline{j}$, and $\underline{k}$ component equal to zero and determine the scalar coefficients of the unknown linear ($V_j^X, V_j^Y, V_j^Z, V_i^X, V_i^Y, V_i^Z$) and angular ($\omega_j^X, \omega_j^Y, \omega_j^Z, \omega_i^X, \omega_i^Y, \omega_i^Z$) velocities for particle *i* and particle *j*:

- Component in the **$\underline{i}$**-direction set equal to zero and expanding the terms:

$$\left(\mu^n - \mu^t\right)\left(V_j^X e_{ij}^X e_{ij}^X - V_i^X e_{ij}^X e_{ij}^X + V_j^Y e_{ij}^Y e_{ij}^X - V_i^Y e_{ij}^Y e_{ij}^X + V_j^Z e_{ij}^Z e_{ij}^X - V_i^Z e_{ij}^Z e_{ij}^X\right) - \mu^n V_0 e_{ij}^X$$
$$+ \mu^t\left(V_j^X - V_i^X - d_{ji}\omega_j^Y e_{ij}^Z + d_{ji}\omega_j^Z e_{ij}^Y - d_{ij}\omega_i^Y e_{ij}^Z + d_{ij}\omega_i^Z e_{ij}^Y\right) = 0$$

- Separating into coefficients of unknown variables gives:

$$\left[\left(\mu^n - \mu^t\right)\left(e_{ij}^X e_{ij}^X\right) + \mu^t\right]V_j^X + \left[\left(\mu^n - \mu^t\right)\left(e_{ij}^Y e_{ij}^X\right)\right]V_j^Y + \left[\left(\mu^n - \mu^t\right)\left(e_{ij}^Z e_{ij}^X\right)\right]V_j^Z \qquad \text{[A14]}$$
$$+ \left[\left(\mu^t - \mu^n\right)\left(e_{ij}^X e_{ij}^X\right) - \mu^t\right]V_i^X + \left[\left(\mu^t - \mu^n\right)\left(e_{ij}^Y e_{ij}^X\right)\right]V_i^Y + \left[\left(\mu^t - \mu^n\right)\left(e_{ij}^Z e_{ij}^X\right)\right]V_i^Z$$
$$+ [0]\omega_j^X + \left[-\mu^t d_{ji} e_{ij}^Z\right]\omega_j^Y + \left[\mu^t d_{ji} e_{ij}^Y\right]\omega_j^Z + [0]\omega_i^X + \left[-\mu^t d_{ij} e_{ij}^Z\right]\omega_i^Y + \left[\mu^t d_{ij} e_{ij}^Y\right]\omega_i^Z = +\mu^n V_0 e_{np}^X$$

- Component in the $\underline{j}$-direction (set equal to zero):

$$\left(\mu^n - \mu^t\right)\left(V_j^X e_{ij}^X e_{ij}^Y - V_i^X e_{ij}^X e_{ij}^Y + V_j^Y e_{ij}^Y e_{ij}^Y - V_i^Y e_{ij}^Y e_{ij}^Y + V_j^Z e_{ij}^Z e_{ij}^Y - V_i^Z e_{ij}^Z e_{ij}^Y\right) - \mu^n V_0 e_{ij}^Y$$
$$+ \mu^t\left(V_j^Y - V_i^Y + d_{ji}\omega_j^X e_{ij}^Z - d_{ji}\omega_j^Z e_{ij}^X + d_{ij}\omega_i^X e_{ij}^Z - d_{ij}\omega_i^Z e_{ij}^X\right) = 0$$

- Separating into coefficients of unknown variables gives:

$$\left[\left(\mu^n-\mu^t\right)\left(e_{ij}^X e_{ij}^Y\right)\right]V_j^X+\left[\left(\mu^n-\mu^t\right)\left(e_{ij}^Y e_{ij}^Y\right)+\mu^t\right]V_j^Y+\left[\left(\mu^n-\mu^t\right)\left(e_{ij}^Z e_{ij}^Y\right)\right]V_j^Z \qquad \text{[A15]}$$

$$+\left[\left(\mu^t-\mu^n\right)\left(e_{ij}^X e_{ij}^Y\right)\right]V_i^X+\left[\left(\mu^t-\mu^n\right)\left(e_{ij}^Y e_{ij}^Y\right)-\mu^t\right]V_i^Y+\left[\left(\mu^t-\mu^n\right)\left(e_{ij}^Z e_{ij}^Y\right)\right]V_i^Z$$

$$+\left[\mu^t d_{ji} e_{ij}^Z\right]\omega_j^X+[0]\omega_j^Y+\left[-\mu^t d_{ji} e_{ij}^x\right]\omega_j^Z+\left[\mu^t d_{ij} e_{ij}^Z\right]\omega_i^X+[0]\omega_i^Y+\left[-\mu^t d_{ij} e_{ij}^X\right]\omega_i^Z=+\mu^n V_0 e_{np}^Y$$

- Component in the <u>*k*</u>-direction (set equal to zero):

$$\left(\mu^n-\mu^t\right)\left(V_j^X e_{ij}^X e_{ij}^Z-V_i^X e_{ij}^X e_{ij}^Z+V_j^Y e_{ij}^Y e_{ij}^Z-V_i^Y e_{ij}^Y e_{ij}^Z+V_j^Z e_{ij}^Z e_{ij}^Z-V_i^Z e_{ij}^Z e_{ij}^Z\right)-\mu^n V_0 e_{ij}^Z$$

$$+\mu^t\left(V_j^Z-V_i^Z-d_{ji}\omega_j^X e_{ij}^Y+d_{ji}\omega_j^Y e_{ij}^X-d_{ij}\omega_i^X e_{ij}^Y+d_{ij}\omega_i^Y e_{ij}^X\right)=0$$

- Separating into coefficients of unknown variables:

$$\left[\left(\mu^n-\mu^t\right)\left(e_{ij}^X e_{ij}^Z\right)\right]V_j^X+\left[\left(\mu^n-\mu^t\right)\left(e_{ij}^Y e_{ij}^Z\right)\right]V_j^Y+\left[\left(\mu^n-\mu^t\right)\left(e_{ij}^Z e_{ij}^Z\right)+\mu^t\right]V_j^Z \qquad \text{[A16]}$$

$$+\left[\left(\mu^t-\mu^n\right)\left(e_{ij}^X e_{ij}^Z\right)\right]V_i^X+\left[\left(\mu^t-\mu^n\right)\left(e_{ij}^Y e_{ij}^Z\right)\right]V_i^Y+\left[\left(\mu^t-\mu^n\right)\left(e_{ij}^Z e_{ij}^Z\right)-\mu^t\right]V_i^Z$$

$$+\left[-\mu^t d_{ji} e_{ij}^Y\right]\omega_j^X+\left[\mu^t d_{ji} e_{ij}^X\right]\omega_j^Y+[0]\omega_j^Z+\left[-\mu^t d_{ij} e_{ij}^Y\right]\omega_i^X+\left[\mu^t d_{ij} e_{ij}^X\right]\omega_i^Y+[0]\omega_i^Z=+\mu^n V_0 e_{np}^Z$$

The coefficients of the unknown variables from equations [A14], [A15] and [A16] determine the terms in matrices A_{11}, A_{12}, A_{13}, and A_{14} in Section A.4.

A.3 EQUATIONS FOR MOMENT EQUILIBRIUM

The free body diagram (FBD) of the interaction between two overlapping particles i and j as shown in Figure 68 is used to determine the relationship between the moments and the velocities acting on the particles. The following equation must be satisfied for moment equilibrium at the contact surface of the overlapping particles,

$$d_{ij}\,\underline{e}_{ij} \times \underline{F}^{t}_{ij} = \underline{0}\ .$$

$$-d_{ij}\,\underline{e}_{ij} \times \underline{F}^{t}_{ji} = \underline{0} \text{ since } \underline{F}^{t}_{ij} = -\underline{F}^{t}_{ji}$$

Substituting $\underline{F}^{t}_{ji} = \left[\mu^{t}\,\Delta\underline{V}^{t}_{ji}\right]$ gives,

$$-d_{ij}\,\underline{e}_{ij} \times \left[\mu^{t}\,\Delta\underline{V}^{t}_{ji}\right] = \underline{0}$$

Substituting $\Delta\underline{V}^{t}_{ji} = \Delta\underline{V}_{ji} - \Delta\underline{V}^{n}_{ji}$ and simplifying gives,

$$-d_{ij}\,\underline{e}_{ij} \times \left(\mu^{t}\right)\left(\Delta\underline{V}_{ji} - \Delta\underline{V}^{n}_{ji}\right) = \underline{0}$$

$$-d_{ij}\,\mu^{t}\,\underline{e}_{ij} \times \left(\Delta\underline{V}_{ji} - \Delta\underline{V}^{n}_{ji}\right) = \underline{0}$$

$$-d_{ij}\,\mu^{t}\,\underline{e}_{ij} \times \left(\Delta\underline{V}_{ji}\right) + d_{ij}\,\mu^{t}\,\underline{e}_{ij} \times \Delta\underline{V}^{n}_{ji} = \underline{0} \qquad \text{[A17]}$$

Recall, the expression for $\Delta \underline{V}_{ji}^{n}$ specified by equation [A6],

$$\Delta \underline{V}_{ji}^{n} = \left[\left(V_j^X - V_i^X\right)e_{ij}^X + \left(V_j^Y - V_i^Y\right)e_{ij}^Y + \left(V_j^Z - V_i^Z\right)e_{ij}^Z\right]\underline{e}_{ij}$$

Note that $\underline{e}_{ij} \times \underline{e}_{ij} = \underline{0}$. Consequently, the second term in equation [A17] (i.e. $d_{ij}\mu^t \underline{e}_{ij} \times \Delta \underline{V}_{ji}^{n}$) is zero. Thus, the moment equilibrium equation [A17] reduces to:

$$-d_{ij}\mu^t \underline{e}_{ij} \times \Delta \underline{V}_{ji} = \underline{0} \qquad \text{[A18]}$$

Recall,

$$\underline{e}_{ij} = e_{ij}^X \underline{i} + e_{ij}^Y \underline{j} + e_{ij}^Z \underline{k}$$

and,

$$\begin{aligned}\Delta \underline{V}_{ji} = &\left[V_j^X - V_i^X - d_{ji}\left(\omega_j^Y e_{ij}^Z - \omega_j^Z e_{ij}^Y\right) - d_{ij}\left(\omega_i^Y e_{ij}^Z - \omega_i^Z e_{ij}^Y\right)\right]\underline{i} \\ &+ \left[V_j^Y - V_i^Y + d_{ji}\left(\omega_j^X e_{ij}^Z - \omega_j^Z e_{ij}^X\right) + d_{ij}\left(\omega_i^X e_{ij}^Z - \omega_i^Z e_{ij}^X\right)\right]\underline{j} \\ &+ \left[V_j^Z - V_i^Z - d_{ji}\left(\omega_j^X e_{ij}^Y - \omega_j^Y e_{ij}^X\right) - d_{ij}\left(\omega_i^X e_{ij}^Y - \omega_i^Y e_{ij}^X\right)\right]\underline{k}\end{aligned}$$

Substituting these expressions into equation [A18] give,

$$\begin{aligned}-d_{ij}\mu^t\left(e_{ij}^X \underline{i} + e_{ij}^Y \underline{j} + e_{ij}^Z \underline{k}\right) \times &\left\{\left[V_j^X - V_i^X - d_{ji}\left(\omega_j^Y e_{ij}^Z - \omega_j^Z e_{ij}^Y\right) - d_{ij}\left(\omega_i^Y e_{ij}^Z - \omega_i^Z e_{ij}^Y\right)\right]\underline{i}\right. \\ &+ \left[V_j^Y - V_i^Y + d_{ji}\left(\omega_j^X e_{ij}^Z - \omega_j^Z e_{ij}^X\right) + d_{ij}\left(\omega_i^X e_{ij}^Z - \omega_i^Z e_{ij}^X\right)\right]\underline{j} \\ &\left.+ \left[V_j^Z - V_i^Z - d_{ji}\left(\omega_j^X e_{ij}^Y - \omega_j^Y e_{ij}^X\right) - d_{ij}\left(\omega_i^X e_{ij}^Y - \omega_i^Y e_{ij}^X\right)\right]\underline{k}\right\} = \underline{0}\end{aligned}$$

Taking cross product and separating the coefficients based on the unknown variables results in the following equations that must be satisfied for moment equilibrium:

- Component in the $\underline{i}$ direction:

$$-d_{ij}\mu^t\left\{e_{ij}^Y\left[V_j^Z - V_i^Z - d_{ji}\left(\omega_j^X e_{ij}^Y - \omega_j^Y e_{ij}^X\right) - d_{ij}\left(\omega_i^X e_{ij}^Y - \omega_i^Y e_{ij}^X\right)\right]\right.$$
$$\left.-e_{ij}^Z\left[V_j^Y - V_i^Y + d_{ji}\left(\omega_j^X e_{ij}^Z - \omega_j^Z e_{ij}^X\right) + d_{ij}\left(\omega_i^X e_{ij}^Z - \omega_i^Z e_{ij}^X\right)\right]\right\}\underline{i}$$

- Separating into coefficients of unknown variables:

$$(0)V_j^X + \left(d_{ij}\mu^t e_{ij}^Z\right)V_j^Y + \left(-d_{ij}\mu^t e_{ij}^Y\right)V_j^Z + (0)V_i^X + \left(-d_{ij}\mu^t e_{ij}^Z\right)V_i^Y + \left(d_{ij}\mu^t e_{ij}^Y\right)V_n^Z$$
$$+\left(d_{ij}d_{ji}\mu^t\left[e_{ij}^Y e_{ij}^Y + e_{ij}^Z e_{ij}^Z\right]\right)\omega_j^X - \left(d_{ij}d_{ji}\mu^t e_{ij}^X e_{ij}^Y\right)\omega_j^Y - \left(d_{ij}d_{ji}\mu^t e_{ij}^X e_{ij}^Z\right)\omega_j^Z$$
$$+\left(d_{ij}d_{ij}\mu^t\left[e_{ij}^Y e_{ij}^Y + e_{ij}^Z e_{ij}^Z\right]\right)\omega_i^X - \left(d_{ij}d_{ij}\mu^t e_{ij}^X e_{ij}^Y\right)\omega_i^Y - \left(d_{ij}d_{ij}\mu^t e_{ij}^X e_{ij}^Z\right)\omega_i^Z \qquad \text{[A19]}$$

- Component in the $\underline{j}$ direction:

$$d_{ij}\mu^t\left\{e_{ij}^X\left[V_j^Z - V_i^Z - d_{ji}\left(\omega_j^X e_{ij}^Y - \omega_j^Y e_{ij}^X\right) - d_{ij}\left(\omega_i^X e_{ij}^Y - \omega_i^Y e_{ij}^X\right)\right]\right.$$
$$\left.-e_{ij}^Z\left[V_j^X - V_i^X - d_{ji}\left(\omega_j^Y e_{ij}^Z - \omega_j^Z e_{ij}^Y\right) - d_{ij}\left(\omega_i^Y e_{ij}^Z - \omega_i^Z e_{ij}^Y\right)\right]\right\}\underline{j}$$

- Separating into coefficients of unknown variables:

$$-\left(d_{ij}\mu^t e_{ij}^Z\right)V_j^X + (0)V_j^Y + \left(d_{ij}\mu^t e_{ij}^X\right)V_j^Z + \left(d_{ij}\mu^t e_{ij}^Y\right)V_i^X + (0)V_i^Y + \left(-d_{ij}\mu^t e_{ij}^X\right)V_i^Z$$
$$-\left(d_{ij}d_{ji}\mu^t e_{ij}^X e_{ij}^Y\right)\omega_j^X + \left(d_{ij}d_{ji}\mu^t\left[e_{ij}^X e_{ij}^X + e_{ij}^Z e_{ij}^Z\right]\right)\omega_j^Y - \left(d_{ij}d_{ji}\mu^t e_{ij}^Z e_{ij}^Y\right)\omega_j^Z$$
$$-\left(d_{ij}d_{ji}\mu^t e_{ij}^X e_{ij}^Y\right)\omega_i^X + \left(d_{ij}d_{ji}\mu^t\left[e_{ij}^X e_{ij}^X + e_{ij}^Z e_{ij}^Z\right]\right)\omega_i^Y - \left(d_{ij}d_{ji}\mu^t e_{ij}^Z e_{ij}^Y\right)\omega_i^Z = 0 \qquad \text{[A20]}$$

- Component in $\underline{k}$ direction:

$$-d_{ij}\mu^t\left\{e_{ij}^X\left[V_j^Y - V_i^Y + d_{ji}\left(\omega_j^X e_{ij}^Z - \omega_j^Z e_{ij}^X\right) + d_{ij}\left(\omega_i^X e_{ij}^Z - \omega_i^Z e_{ij}^X\right)\right]\right.$$
$$\left.-e_{ij}^Y\left[V_j^X - V_i^X - d_{ji}\left(\omega_j^Y e_{ij}^Z - \omega_j^Z e_{ij}^Y\right) - d_{ij}\left(\omega_i^Y e_{ij}^Z - \omega_i^Z e_{ij}^Y\right)\right]\right\}\underline{k}$$

- Separating into coefficients of unknown variables:

$$\left(d_{ij}\mu^t e_{ij}^Y\right)V_j^X + \left(-d_{ij}\mu^t e_{ij}^X\right)V_j^Y + (0)V_j^Z + \left(-d_{ij}\mu^t e_{ij}^Y\right)V_i^X + \left(d_{ij}\mu^t e_{ij}^X\right)V_i^Y + (0)V_i^Z$$
$$-\left(d_{ij}d_{ji}\mu^t e_{ij}^X e_{ij}^Z\right)\omega_j^X - \left(d_{ij}d_{ji}\mu^t e_{ij}^Y e_{ij}^Z\right)\omega_j^Y + \left(d_{ij}d_{ji}\mu^t\left[e_{ij}^X e_{ij}^X + e_{ij}^Y e_{ij}^Y\right]\right)\omega_j^Z$$
$$-\left(d_{ij}d_{ij}\mu^t e_{ij}^X e_{ij}^Z\right)\omega_i^X - \left(d_{ij}d_{ij}\mu^t e_{ij}^Y e_{ij}^Z\right)\omega_i^Y + \left(d_{ij}d_{ij}\mu^t\left[e_{ij}^X e_{ij}^X + e_{ij}^Y e_{ij}^Y\right]\right)\omega_i^Z = 0 \qquad \text{[A21]}$$

The coefficients of the unknown variables from equations [A19], [A20] and [A21] determine the terms in matrices A_{21}, A_{22}, A_{23}, and A_{24} in Section A.4.

A.4 CONTRIBUTIONS TO ASSEMBLAGE OF MATRIX

Thus, we can specify the contributions for the pair particles *i* and *j* in contact to the global assemblage of the matrix as the following:

$$\left[\begin{array}{c|c|c|c} A_{11} & A_{12} & A_{13} & A_{14} \\ \hline A_{21} & A_{22} & A_{23} & A_{24} \end{array}\right]_{6x12} \begin{bmatrix} V_i^X \\ V_i^Y \\ V_i^Z \\ V_j^X \\ V_j^Y \\ V_j^Z \\ \omega_i^X \\ \omega_i^Y \\ \omega_i^Z \\ \omega_j^X \\ \omega_j^Y \\ \omega_j^Z \end{bmatrix}_{12x1} = \begin{bmatrix} \mu^n V_O e_{ij}^X \\ \mu^n V_O e_{ij}^Y \\ \mu^n V_O e_{ij}^Z \\ 0 \\ 0 \\ 0 \end{bmatrix}_{6x1}$$

where the terms in matrices A_{11}, A_{12}, A_{13}, A_{14}, A_{21}, A_{22}, A_{23} and A_{24} are defined as follows:

$$[A_{11}]_{3x3} = \begin{bmatrix} (\mu^t - \mu^n) e_{ij}^X e_{ij}^X - \mu^t & (\mu^t - \mu^n) e_{ij}^X e_{ij}^Y & (\mu^t - \mu^n) e_{ij}^X e_{ij}^Z \\ (\mu^t - \mu^n) e_{ij}^X e_{ij}^Y & (\mu^t - \mu^n) e_{ij}^Y e_{ij}^Y - \mu^t & (\mu^t - \mu^n) e_{ij}^Y e_{ij}^Z \\ (\mu^t - \mu^n) e_{ij}^X e_{ij}^Z & (\mu^t - \mu^n) e_{ij}^Y e_{ij}^Z & (\mu^t - \mu^n) e_{ij}^Z e_{ij}^Z - \mu^t \end{bmatrix}$$

$$[A_{12}]_{3x3} = \begin{bmatrix} (\mu^n - \mu^t) e_{ij}^X e_{ij}^X + \mu^t & (\mu^n - \mu^t) e_{ij}^X e_{ij}^Y & (\mu^n - \mu^t) e_{ij}^X e_{ij}^Z \\ (\mu^n - \mu^t) e_{ij}^X e_{ij}^Y & (\mu^n - \mu^t) e_{ij}^Y e_{ij}^Y + \mu^t & (\mu^n - \mu^t) e_{ij}^Y e_{ij}^Z \\ (\mu^n - \mu^t) e_{ij}^X e_{ij}^Z & (\mu^n - \mu^t) e_{ij}^Y e_{ij}^Z & (\mu^n - \mu^t) e_{ij}^Z e_{ij}^Z + \mu^t \end{bmatrix}$$

$$[A_{13}]_{3x3} = \begin{bmatrix} 0 & -\mu^t d_{ij} e_{ij}^Z & \mu^t d_{ij} e_{ij}^Y \\ \mu^t d_{ij} e_{ij}^Z & 0 & -\mu^t d_{ij} e_{ij}^X \\ -\mu^t d_{ij} e_{ij}^Y & \mu^t d_{ij} e_{ij}^X & 0 \end{bmatrix}$$

$$[A_{14}]_{3x3} = \begin{bmatrix} 0 & -\mu^t d_{ji} e_{ij}^Z & \mu^t d_{ji} e_{ij}^Y \\ \mu^t d_{ji} e_{ij}^Z & 0 & -\mu^t d_{ji} e_{ij}^X \\ -\mu^t d_{ji} e_{ij}^Y & \mu^t d_{ji} e_{ij}^X & 0 \end{bmatrix}$$

$$[A_{21}]_{3x3} = \begin{bmatrix} 0 & -\mu^t d_{ij} e_{ij}^Z & \mu^t d_{ij} e_{ij}^Y \\ \mu^t d_{ij} e_{ij}^Z & 0 & -\mu^t d_{ij} e_{ij}^X \\ -\mu^t d_{ij} e_{ij}^Y & \mu^t d_{ij} e_{ij}^X & 0 \end{bmatrix}$$

$$[A_{22}]_{3x3} = \begin{bmatrix} 0 & \mu^t d_{ij} e_{ij}^Z & -\mu^t d_{ij} e_{ij}^Y \\ -\mu^t d_{ij} e_{ij}^Z & 0 & \mu^t d_{ij} e_{ij}^X \\ \mu^t d_{ij} e_{ij}^Y & -\mu^t d_{ij} e_{ij}^X & 0 \end{bmatrix}$$

$$[A_{23}]_{3x3} = \begin{bmatrix} \mu^t d_{ij} d_{ij} \left(e_{ij}^Y e_{ij}^Y + e_{ij}^Z e_{ij}^Z \right) & -\mu^t d_{ij} d_{ij} e_{ij}^X e_{ij}^Y & -\mu^t d_{ij} d_{ij} e_{ij}^X e_{ij}^Z \\ -\mu^t d_{ij} d_{ij} e_{ij}^X e_{ij}^Y & \mu^t d_{ij} d_{ij} \left(e_{ij}^X e_{ij}^X + e_{ij}^Z e_{ij}^Z \right) & -\mu^t d_{ij} d_{ij} e_{ij}^Y e_{ij}^Z \\ -\mu^t d_{ij} d_{ij} e_{ij}^X e_{ij}^Z & -\mu^t d_{ij} d_{ij} e_{ij}^Y e_{ij}^Z & \mu^t d_{ij} d_{ij} \left(e_{ij}^X e_{ij}^X + e_{ij}^Y e_{ij}^Y \right) \end{bmatrix}$$

$$[A_{24}]_{3x3} = \begin{bmatrix} \mu^t d_{ij} d_{ji} \left(e_{ij}^Y e_{ij}^Y + e_{ij}^Z e_{ij}^Z \right) & -\mu^t d_{ij} d_{ji} e_{ij}^X e_{ij}^Y & -\mu^t d_{ij} d_{ji} e_{ij}^X e_{ij}^Z \\ -\mu^t d_{ij} d_{ji} e_{ij}^X e_{ij}^Y & \mu^t d_{ij} d_{ji} \left(e_{ij}^X e_{ij}^X + e_{ij}^Z e_{ij}^Z \right) & -\mu^t d_{ij} d_{ji} e_{ij}^Y e_{ij}^Z \\ -\mu^t d_{ij} d_{ji} e_{ij}^X e_{ij}^Z & -\mu^t d_{ij} d_{ji} e_{ij}^Y e_{ij}^Z & \mu^t d_{ij} d_{ji} \left(e_{ij}^X e_{ij}^X + e_{ij}^Y e_{ij}^Y \right) \end{bmatrix}$$

BIBLIOGRAPHY

1. R.M. German. *Sintering Theory and Practice*. New York: John Wiley and Sons (1996).

2. H.E. Exner and E. Arzt. *Chapter 31: Sintering Processes* from *Physical Metallurgy*, R.W. Cahn and P. Haasen, Editors. Elsevier Science: Amsterdam, pp. 2628-2662 (1996).

3. W.D. Kingery, H.K. Bowden and D.R. Uhlmann, *Introduction to Ceramics*, 2nd edition, Wiley Series on the Science and Technology of Materials. John Wiley & Sons, New York, (1976).

4. E.A. Olevsky. Theory of Sintering; From Discrete to Continuum. Materials Science and Engineering, **R23** [2], pp. 41-100 (1998).

5. A.C.F. Cocks. Constitutive modeling of powder compaction and sintering. Progress in Materials Science, **46**, pp. 201-229 (2001).

6. W.D. Kingery and M. Berg. Study of the Initial Stages of Sintering Solids by Viscous Flow, Evaporation-Condensation, and Self-Diffusion. *Journal of Applied Physics*, **26**, pp. 1205-1212 (1955).

7. R.L. Coble. Sintering Crystalline Solids I. Intermediate and Final Stage Diffusion Models. *Journal of Applied Physics*, **32** [5], pp. 787-792 (1961).

8. M.F. Ashby. A First Report on Sintering. *Acta Metallurgica*, **22**, pp. 275-289 (1974).

9. M.F. Ashby. A Second Report on Sintering. *Acta Metallurgica*, **29**, pp. 259-281 (1981).

10. H.J. Reidel and B. Blug. A comprehensive model for solid state sintering and its application to silicon carbide. In: Multiscale Deformation and Fracture in Materials and Structures, the James R. Rice 60th Anniversary Volume, T.J. Chuang and J.W. Rudnicki, Eds., Kluwer Academic Publishers, Dordrecht Boston London, pp. 49-70 (2001).

11. A. Jagota and P.R. Dawson, Micromechanical modeling of powder compacts – I. Unit problems for sintering and traction induced deformation. *Acta Metallurgia*, **36** [9], pp. 2551-2561 (1988).

12. A. Jagota and P.R. Dawson, Micromechanical modeling of powder compacts – II. Truss formulation of discrete packings. *Acta Metallurgia*, **36** [9], pp. 2563-2573 (1988).

13. J. Zheng and P.E. Johnson. Evolution of the Topology during Simulated Sintering of Powder Compacts. *J. Am. Ceramic Soc*., **76** [11], pp. 2760-2768 (1993).

14. G.T. Nolan and P.E. Kavanaugh. The size distribution of interstices in random packings of spheres. *Powder Technology*, **78**, pp. 231-238 (1994).

15. G.T. Nolan and P.E. Kavanaugh. Computer simulation of random packings of spheres with log-normal distributions. *Powder Technology*, **76**, pp. 309-316 (1993).

16. G.T. Nolan and P.E. Kavanaugh. Computer simulation of random packings of hard spheres. *Powder Technology*, **72**, pp. 149-155 (1992).

17. K. Krishnan, R. McAfee, I. Nettleship, and W. Slaughter. A Representative Volume Element for the Densification of Powders. Accepted for publication in *J. Am. Ceramic Soc.* (2005).

18. N.D. Aparicio and A.C.F. Cocks. On the representation of random packings of spheres for sintering simulations. *Acta Mater*, **43** [10], pp. 3873-3884 (1995).

19. A. Pavlovitch, R. Julien and P. Meakin. Geometrical properties of a random packing of hard spheres. *Physica A*, **176**, pp. 206-219 (1991).

20. A. Yang, C.T. Miller and L.D. Turcoliver. Simulation of correlated and uncorrelated packing of random size spheres. *Physical Review E*, Vol. 53, pp.1516-1524 (1996).

21. R.M. McMeeking and L. T. Kuhn. A diffusional creep law for powder compacts. *Acta Metallurgia*, Vol. 40, No. 5, p. 961-969 (1992).

22. F. Parhami and R.M. McMeeking. A network model for initial stage sintering. *Mechanics of Materials*, Vol. 27, No. 5, pp. 111-124 (1998).

23. W.S. Slaughter, I. Nettleship, M.D. Lehigh and P. Po-on Tong. A quantitative analysis of the effect of the geometric assumptions in sintering models. *Acta Mater*, **45** [12], pp. 5077-5086 (1997).

24. I. Nettleship and W. Slaughter. Dimensionless Parameters for Microstructural Pathways in Sintering. *J. Am. Ceramic Soc.*, **81** [3], pp. 700-704 (1998).

25. J. Svoboda, H. Riedel and H. Zipse. Equilibrium pore surfaces, sintering stresses and constitutive equations for the intermediate and late stages of sintering – I. Computation of equilibrium surfaces. *Acta Mater*, Vol. 42, No.2, pp.435-443 (1994).

26. H. Riedel, H. Zipse, and J. Svoboda. Equilibrium pore surfaces, sintering stresses and constitutive equations for the intermediate and late stages of sintering – II. Diffusional densification and creep. *Acta Mater*, Vol. 42, No.2, pp.445-452 (1994).

27. H.G. Kim, O. Gillia, and D. Bouvard. A phenomenological constitutive model for the sintering of alumina powder. *J. Eur. Cer. Soc.*, **23**, pp.1675-1685 (2003).

28. A. Jagota and P.R. Dawson. An anisotrpic continuum model for the sintering and compaction of powder packings. *Mechanics of Materials*, **7**, pp.255-269 (1988).

29. I. Nettleship, R. McAfee, and W. Slaughter. Evolution of the Grain Size Distribution during the Sintering of Alumina at 1350 C. *J. Am. Ceramic Soc.*, **85** [8], pp. 1954-1960 (2002).

30. R.T. DeHoff and F. N. Rhines, *Quantitative Microscopy*. McGraw Hill (1968).

31. A. Baddeley. *Spatial Statistics and Digital Image Analysis, Ch. 10: Stereology*. pp. 181-216, National Academy Press (1991).

32. *Quantitative Image Analysis of Microstructures*, H.E. Exner and H. P. Hougardy (eds.), DGM Informationsgellschaft mbH, Germany (1988).

33. E.E. Underwood. *Quantitative Stereology*. Addison-Wesley, Reading, MA (1970).

34. R. McAfee and I. Nettleship. The simulation and selection of shapes for the unfolding of grain size distributions. *Acta Mater*, Vol. 51, pp. 4603-4610 (2003).

35. R. McAfee. A study of microstructural evolution during sintering using tessellation. *Doctoral Dissertation*, University of Pittsburgh (2004).

36. A. Okabe, B. Boots, K. Sugihara and S.N. Chiu. Spatial Tessellations: Concepts and Applications of Voronoi Diagrams. 2nd Edition, Wiley (2000).

37. R. McAfee, I. Nettleship, and W. Slaughter. A Mesoscale Description of Microstructure Evolution for the Sintering of Ceramics. Submitted to *Acta Mater* for publication (2005).

38. William H. Press, *et al*. *Numerical Recipes in C++: the Art of Scientific Computing*, 2nd Edition. Cambridge University Press, Cambridge UK (2002).

39. A. Leon-Garcia. *Probability and Random Processes for Electrical Engineering*, 2nd Edition, Addison Wesley, p.576 (1994).

40. D.L. Logan. *A first course in the finite element method*. pp. 35-37. PWS Publishers, Boston, MA. (1986).

41. John B. Fraleigh. *Calculus with Analytical Geometry*. 2nd Edition, Addison Wesley Publishing Company, p.869 (1985).

42. N.J. Shaw and R.J. Brook. Structure and Grain Coarsening During the Sintering of Alumina. *J. Am. Ceramic Soc*., **69** [2], pp. 107-110 (1986).

43. E.H. Aigeltinger and R.T. Dehoff. Quantitative Determination of Topographical and Metric Properties During Sintering of Copper. *Metal. Trans A*, **6A**, pp.1853-1862 (1975).

44. E.H. Aigeltinger and H.E. Exner. Stereological Characterization of the Interaction Between Interfaces and its Application to the Sintering Process. *Metal. Trans A*, **8A**, pp.421-1424 (1977).

45. C.A. Handmerker, R.M. Cannon, and R.L. Coble. Final Stage Sintering of MgO. pp. 619-643. In: "Structures and Properties of MgO and Al_2O_3," Advances in Ceramics 10, edited by W.D. Kingery, published by American Ceramics Society, Columbus OH (1984).

46. H.P. Harmer . Use of Solid-Solution Additives in Ceramics Processing. pp. 679-696. In: "Structures and Properties of MgO and Al_2O_3," Advances in Ceramics 10, edited by W.D. Kingery, published by American Ceramics Society, Columbus OH (1984).